Chen Wang

Na-K-Sb photocathodes-synthesis, characterization and application in photoinjector

Schriftenreihe der Arbeitsgruppe des Lehrstuhls für Oberflächen- und Werkstofftechnologie im Institut für Werkstofftechnik

Impressum
Prof. Dr. rer. nat. habil. Xin Jiang
Lehrstuhl für Oberflächen- und Werkstofftechnologie
Institut für Werkstofftechnik
Universität Siegen
57076 Siegen
ISSN: 2194-0096
Zugl.: Siegen, Univ., Diss., 2026

Na-K-Sb Photocathodes-Synthesis, Characterization and Application in Photoinjector

Von der Naturwissenschaftlich-Technischen Fakultät

der Universität Siegen

zur Erlangung des Grades eines Doktors

der Ingenieurwissenschaften

genehmigte

Dissertation

von:	M. Sc. Chen Wang
aus:	Liaoning, China
eingereicht am:	12. Januar 2026
Mündliche Prüfung am:	12. Juni 2026
Referent:	Prof. Dr. rer. nat. habil. Xin Jiang
Koreferent:	Prof. Dr. rer. nat. Dipl-Phys. Thorsten Kamps

Zusammenfassung

Moderne und zukünftige Beschleunigeranlagen – wie Energy Recovery Linacs (ERLs),[1,2] Freie-Elektronen-Laser (FELs)[3,4] und Instrumente für ultraschnelle Elektronenbeugung (UED)[5] – stellen zunehmend höhere Anforderungen an die Brillanz und Robustheit der Elektronenquellen. Um diesen Anforderungen zu begegnen, werden Photokathoden in verschiedenen Materialsystemen eingesetzt. Unter diesen sind Multi-Alkali-Antimonid-Photokathoden vielversprechende Kandidaten für hohe Brillanz aufgrund ihrer hohen Quanteneffizienz (QE) und ihrer niedrigen intrinsischen Emittanz im sichtbaren Spektralbereich.[6]

Na–K–Sb-Photokathoden weisen dabei vergleichbare QE-Werte wie Cs–K–Sb im sichtbaren Bereich auf und erreichen mehrere Prozent im grünen Spektralbereich,[7,8] bei gleichzeitig überlegener thermischer Robustheit – einer entscheidenden Eigenschaft für viele Anwendungen, zum Beispiel ERLs.[9] Trotz dieser Vorteile wurde die breite Anwendung von Na–K–Sb-Photokathoden durch eine geringe Reproduzierbarkeit und niedrige Erfolgsraten bei der Herstellung behindert, die auf drei grundlegende Herausforderungen zurückzuführen sind: (1) ein außergewöhnlich schmales stöchiometrisches Fenster für hohe QE, (2) der extrem niedrige Gleichgewichts-Dampfdruck von Natrium, der für die hoch-effiziente Na_2KSb-Phase erforderlich ist, und (3) eine unzureichende Kontrolle über Schlüsselparameter während der Abscheidung, insbesondere der Flussraten der Alkalimetalle.

In dieser Arbeit werden diese Herausforderungen systematisch angegangen, durch den Entwurf und die Inbetriebnahme einer neuen Präparationskammer sowie die Entwicklung einer optimierten Dreifachverdampfungsmethode, bei der die drei Elemente gleichzeitig auf dem Substrat verdampfen. Mittels detaillierter Charakterisierung der spektralen Empfindlichkeit und Röntgenphotoelektronenspektroskopie (XPS) wird erstmals das reproduzierbare Wachstum von Na_2KSb Photokathoden unter hochkontrollierten Bedingungen auf Substraten demonstri-

ert, die für Elektronenbeschleuniger geeignet sind. Ein Kontrollvariablen-Ansatz stellt klare Korrelationen zwischen Wachstumsparametern, Stöchiometrie und photoemissiven Eigenschaften her. Eine umfassende Analyse der QE-Homogenität, gestützt durch ein Wachstumsmodell, ermöglicht eine schnelle und präzise Einstellung der QE. Darüber hinaus wird eine umfangreiche XPS-Datenbank, basierend auf der Stöchiometrie, von über 35 Na–K–Sb-Photokathoden erstellt. Abschließend wird der erfolgreiche Betrieb eines supraleitenden Radiofrequenz (SRF) Photoinjektors unter Verwendung einer Na_2KSb-Photokathode berichtet, bei dem im SEALab SRF-Photoinjektor der erste Betrieb erzielt wurde.

Acknowledgements

I would like to express my deepest gratitude to everyone who supported and guided me during my doctoral studies. The completion of this dissertation would not be possible without their helps.

First of all, I would like to thank my supervisors, Prof. Dr. Xin Jiang, Prof. Dr. Thorsten Kamps and Dr. Julius Kühn. You have given me key support and guidance, and placed great trust and freedom in my research, enabling me to devote myself to the research project.

At the same time, I would like to express my sincere gratitude to all my colleagues in the photocathode laboratory, where I spent the last four years working wholeheartedly. Dr. Julius Kühn, we worked together and went through the best days and the worst days, you are not only my supervisor but also a true friend. Jonas Dubes, thank you very much for updating the spectral response system and vacuum suitcase, I wish you great success in your doctoral research. Prof. Alice Galdi, thank you for coming and sharing your wisdom. Without you, we would not have been able to develop the best ever Na-K-Sb photocathode growth method. I also thank Dr. Sonal Mistry for her guidance during the first half of my PhD, and Hugh and Marija for working with me and exchanging ideas.

I am grateful to the SEALab photoinjector team for their dedicated work, especially Dr. Guido Klemz for his support with the QE measurements in the SRF photoinjector. I thank my second advisor, Prof. Dr. Marcus Bär, for his guidance on XPS analysis, and Dr. Regan Wilks for conducting synchrotron-based X-ray measurements. I thank Grzegorz Gwalt for roughness measurements and Christiane Förster for her wonderful skill in polishing Mo substrates. My thanks also go to our collaborators Prof. Dr. Caterina Cocchi and Dr. Holger-Dietrich Saßnick in Oldenburg for theoretical calculations, as well as Dr. Rong Xiang and Jana Schaber in Dresden, and Dr. Lee Jones in Daresbury for scientific exchanges.

I also want to thank my colleagues and friends—Benat, Emily, Ezgi, Tasha,

Staedler, Brombach, Hameed, Guo Tianxiao, Chen Xinyue, Dong Ximan, Bharath, Li Changli, Li Yao, and Akif—for the inspiring discussions, and constant encouragement.

Finally, I would like to express my special thanks to Dr. Rong Xiang for introducing me to a new position, enabling me to continue my passion for research in this field.

This work was funded by the Deutsche Forschungsgemeinschaft (DFG) - Project number 490940284, the German Bundesministerium für Forschung, Technologie und Raumfahrt, Land Berlin and grants of the Helmholtz Association.

Wang Chen

Publication list

Publication:

1. J Dube, J Kühn, C Wang, S Mistry, G Klemz, A Galdi, and T Kamps, Triple evaporation growth and photoemission characterization of bialkali antimonide photocathodes. Journal of Applied Physics 138.4 (2025).

2. C Wang, J Dube, A Galdi, T Kamps and J. Kühn, Triple evaporation growth of Sodium-Potassium-Antinominde thin films as photoemission source for electron accelerators. Journal of Physics D: Applied Physics 59 (2026) 075102.

Conference:

1. C. Wang, M. Vogel, X. Jiang, J. Schaber, P. Murcek, R. Xiang, Initial Study of GaN Thin Films for Photocathodes Prepared by Magnetron Sputtering on Copper Substrates, IPAC Conference Proceedings, 2021.

2. C. Wang, Multi-alkali Antimonide Photocathodes for High Brilliant Electron Beams, EWPAA Invited Talk, 2022.

3. S. Mistry, T. Kamps, J. Kühn, C. Wang, Multi-Alkali Antimonide Photocathode Development for High Brightness Beams, IPAC Conference Proceedings, 2022.

4. S. Mistry, J. Dube, T. Kamps, J. Kühn, C. Wang, Evalution of the In-situ Photocathode Handling for SRF Photoinjector of SEALAB, IPAC Conference Proceedings, 2023.

5. C. Wang, Na-K-Sb Photocathodes for High Brilliant Electron Beams, EWPAA Invited Talk, 2024

6. T. Kamps et al., First Beam Commissioning of The HZB SRF Photoelectron Gun, IPAC Conference Proceedings, 2025.

Contents

Symbol List **IV**

Abstract **IX**

1 Motivation **1**

1.1 Motivation 1

1.2 Thesis Outline 2

2 Fundamentals **5**

2.1 SEALab Photoinjector 5

2.2 Requirements of photocathodes 6

2.3 Photoinjector related Photoelectric Properties of Photocathodes . . 8

2.3.1 Quantum Efficiency 8

2.3.2 Storage Lifetime 9

2.3.3 Photoemission Models 10

2.4 Alkali-Antimonides as Photoemissive Materials 15

2.4.1 Na-K-Sb Photocathode System 16

2.4.2 Thermal Stability of Na-K-Sb Compounds 19

2.4.3 Na_2KSb Synthesis Method 20

2.4.4 Thermodynamics of Na_2KSb Synthesis 21

2.5 Challenges in Na-K-Sb Synthesis 23

3 Experimental methods **25**

3.1 Substrate Preparation 25

3.2 Na-K-Sb Photocathodes Growth Chamber 26

3.2.1 Dispenser Chamber 27

3.2.2 Triple Evaporation Chamber 28

3.3 Spectral Response Setup 35
3.4 X-ray Photoelectron Spectroscopy 36
3.4.1 Fundamental Principles 36
3.4.2 XPS Experimental Setup 39
3.4.3 Chemical Composition Calculation 40
3.4.4 Chemical Shifts 41
3.4.5 Interference and Solutions 42

4 Growth Study of Na-K-Sb Photocathodes 45
4.1 Dispenser Chamber Based Experiment 45
4.1.1 Modified Sequential Deposition 45
4.1.2 Alkali Co-Deposition 47
4.1.3 Discussion of the Two Growth Procedures 47
4.1.4 Reaction Mechanism in Alkli Co-Deposition 48
4.1.5 Stoichiometry and Quantum Efficiency 50
4.1.6 Storage Lifetime 52
4.1.7 Conclusion 53
4.2 Triple Evaporation Chamber Based Experiments 53
4.2.1 Triple Evaporation Method 54
4.2.2 Stoichiometry and Photoemissive Properties 56
4.3 Surface Homogeneity of Na-K-Sb Photocathode Films 60
4.3.1 Model Flux Density on the Film 62
4.3.2 Reaction Model and Stoichiometry 64
4.3.3 Correlation with QE Maps 66
4.4 Maximizing QE in the Center of the Na-K-Sb Photocathode Films 68
4.4.1 Maximizing QE for Na Oversaturated Samples 69
4.4.2 Maximizing QE for Na deficient samples 69
4.4.3 Reducing Inhomogeneity by Decreasing the Angular Separation between Na and Sb Sources 71

4.5 Statistical Results of Stoichiometry and Photoemissive Properties . 73
4.5.1 QE and Stoichiometry 73
4.5.2 Storage Lifetime and Stoichiometry 76
4.6 Spectral Response Curve 79
4.6.1 Photoemission Models and Curve Fitting 79
4.6.2 Spectral Response Dependence on Growth Method 81

5 Beam Commissioning at SEALab with Na_2KSb Photocathodes 85
5.1 First Successful Beam Commissioning with SEA02 85
5.2 Second Beam Commissioning with SEA03 86
5.2.1 Growth of SEA03 87
5.2.2 Transfer to SEALab 89
5.2.3 Performance in SEALab 91

6 XPS Results and Data Analysis 93
6.1 Pure Metallic Antimony 93
6.2 K-Sb System 94
6.3 Na-Sb System 97
6.4 Na-K-Sb System 99
6.4.1 Phase Transformation from Na_2KSb to NaK_2Sb 99
6.4.2 Phase Transformation from Na_2KSb to Na_3Sb 100
6.4.3 Core Level Peak Shifts 102
6.5 Thermal Dissociation and Oxidation of Na_2KSb Photocathodes . . 105
6.5.1 Thermal Dissociation 105
6.5.2 Oxidation 107
6.6 Summary of XPS peak fitting results 111

7 Conclusion and Outlook 113
7.1 Conclusion 113
7.2 Outlook 114

7.2.1 Synchrotron Radiation Based X-ray Characterization . . . 115
7.2.2 Epitaxial Growth . . . 116

A Appendix **119**
A.1 Additional XPS Studies . . . 119
A.1.1 Sequential and Triple Evaporation . . . 119
A.1.2 Transformation from Na_2KSb to NaK_2Sb . . . 120
A.1.3 High-QE K-Sb Film . . . 121
A.1.4 Valence Band Structure . . . 122
A.2 Thermal Stability of Na_2KSb Photocathodes . . . 123
A.2.1 Thermal Stability of TWH15-17 . . . 123
A.2.2 Thermal Stability of WH17 in Dispenser Based Chamber . 126
A.2.3 Temperature-Dependent QE Behavior of Na-oversaturated Samples . . . 128
A.3 Additional Spectral Response Studies . . . 129
A.3.1 Spectral Response at increased Temperature . . . 129
A.3.2 Spectral Response at different positions . . . 130
A.4 Full Dataset . . . 130

Bibliography **133**

Symbol List

Abbreviations

AFM	Atomic Force Microscopy
CW	Continuous-Wave (Mode)
DFT	Density Functional Theory
DOS	Density of States
ERLs	Energy Recovery Linacs
FELs	Free-Electron Lasers
FWHM	Full Width at Half Maximum
HAXPES	Hard X-ray Photoelectron Spectroscopy
IGP	Ion Getter Pump
IMFP	Inelastic mean free path
MBPT	Many-Body Perturbation Theory
MTE	Mean Transverse Energy
NEG	Non-Evaporable Getter
RGA	Residual Gas Analysis
SRF	Superconducting Radio-Frequent (Photoinjector)
TCC	Thermal Cracker Cell
UED	Ultrafast Electron Diffraction
UHV	Ultra High Vacuum
XPS	X-ray Photoelectron Spectroscopy
XRD	X-ray Diffraction
XRR	X-ray Reflectivity
VBM	Valance Band Maximum

Chemicals

Ag	Silver
Ar	Argon
C	Carbon
CO	Carbon Monoxide
CO_2	Carbon Dioxide
Cs	Cesium
Cs-Sb	Cesium Antimonide
Cs-K-Sb	Cesium Potassium Antimonide
Cu	Copper
H	Hydrogen
H_2O	Water
K	Potassium
K-Sb	Potassium Antimonide
Mo	Molybdenum
N	Nitrogen
Na	Sodium
Na-Sb	Sodium Antimonide
Na-K-Sb	Sodium Potassium Antimonide
O	Oxygen
Sb	Antimony

Symbols

c	Speed of Light	$2.998 \times 10^8\,\mathrm{m/s}$
e	Elementary Charge	$1.602 \times 10^{-19}\,\mathrm{C}$
E_A	Electron Affinity	eV
E_B	Binding Energy	eV
E_CBM	Conduction Band Minimum	eV
E_F	Fermi Level	eV
E_G	Band Gap	eV
E_K	Kinetic Energy	eV
E_T	Threshold Energy	eV
E_U	Urbach Energy	eV
E_vac	Vacuum Level	eV
E_VBM	Valence Band Maximum	eV
E_WF or ϕ	Work Function	eV
G	Gibbs Free Energy	cal
H	Enthalpy	cal
h	Planck's Constant	$6.626 \times 10^{-34}\,\mathrm{J \cdot s}$
I	Current	A
I_int	Intensity	-
J	Particle Flux	[number of particles] $\mathrm{m^{-2} \cdot s^{-1}}$
K_p	Equilibrium Constant	-
k_B	Boltzmann Constant	$1.38 \times 10^{-10}\,\mathrm{J \cdot K^{-1}}$
p	Pressure	mbar
P	Power	W

QE	Quantum Efficiency	-
r	Reaction Rate	s^{-1}
r_{a}	Radius	m
R	Gas Constant	$1.987\,\mathrm{cal}\cdot\mathrm{K}^{-1}\cdot\mathrm{mol}^{-1}$
R_q	Surface Roughness (RMS)	nm
S	Entropy	cal
t	Time	s
T	Temperature	K or °C
T_{tran}	Transmission Function	-
α_t/α_p	Total/ Effective Optical Absorption Coefficient	m^{-1}
ν	Frequency	HZ
λ	Wavelength	nm
λ_{imfp}	Inelastic Mean Free Path	nm
Φ	Dissociation Energy	$\mathrm{kcal}\cdot\mathrm{mol}^{-1}$
σ_{cs}	Photoionization Cross-Section	-
σ_{T}	Steepness Parameter	-
τ	Lifetime	-

Abstract

State-of-the-art and future accelerators such as energy recovery linacs (ERLs),[1,2] free electron lasers (FELs)[3,4] and ultra-fast electron diffraction (UED)[5] facilities have increasing demands on the brightness and robustness of the electron source. To meet these requirements, photocathodes are employed in a variety of material systems. Among them, multi-alkali antimonide photocathodes are promising candidates for high-brightness applications due to their high quantum efficiency (QE) and low intrinsic emittance in the visible range.[6]

Na–K–Sb photocathodes exhibit QE values comparable to Cs–K–Sb in the visible range, reaching several percent in the green region,[7,8] while offering superior thermal robustness—a critical attribute for many applications, especially ERLs.[9] Despite these advantages, the widespread adoption of Na–K–Sb photocathodes has been hindered by poor reproducibility and low success rates, stemming from three fundamental challenges: (1) an exceptionally narrow stoichiometric window for high QE, (2) the extremely low equilibrium vapor pressure of sodium required for the high-QE Na_2KSb phase, and (3) insufficient control over key deposition parameters, particularly alkali metal flux rates.

In this work, these challenges are systematically addressed through the design and commissioning of a new preparation chamber and the development of an optimized triple evaporation method. Through detailed spectral response and X-ray photoelectron spectroscopy (XPS) characterization, the reproducible growth of Na_2KSb photocathodes under highly controlled conditions is demonstrated for the first time on substrates suitable for electron accelerators. A control variable approach establishes clear correlations between growth parameters, stoichiometry, and photoemissive properties. Comprehensive analysis of QE homogeneity, supported by a growth model, enables rapid and precise tuning of photoemissive performance. Furthermore, an extensive XPS database is compiled from over 35 Na–K–Sb photocathodes based on their stoichiometry. Finally, the successful op-

eration of a superconducting radio-frequency (SRF) photoinjector using a Na_2KSb photocathode is reported, achieving first beam in the SEALab SRF photoinjector.

1. Motivation

1.1. Motivation

Photoinjectors are capable of generating high-brightness electron beams for advanced electron accelerator applications, including energy recovery linac (ERL),[10] ultra-fast electron diffraction,[11] and X-ray free electron laser.[12,13] These applications place stringent demands on photocathodes, which serve as the critical subsystem in the electron beam generating. Among various photocathode materials, multi-alkali antimonides are particularly promising candidates due to their high quantum efficiency (QE) and low intrinsic emittance in the visible range,[6] making them ideally suitable for high-brightness applications.

At Helmholtz-Zentrum Berlin (HZB), a new generation of superconducting RF (SRF) electron accelerators is being developed under the SEALab project. This project establishes specific requirements for photocathode performance, including: high quantum efficiency ($>1\%$) at visible wavelengths, low emittance contribution, long shelf and operational lifetime, and enhanced thermal stability under high-current operation.

Na-K-Sb photocathodes present a particularly attractive option for meeting these demanding specifications. Historical research has demonstrated that Na-K-Sb films achieve QE comparable to Cs-K-Sb in the visible range, with values reaching several percent at 520 nm.[7,8] More significantly, Na-K-Sb photocathodes exhibit superior thermal robustness compared to Cs-K-Sb cathodes,[9] a critical advantage in high-current applications such as ERL applications and electron beam water treatment.

Despite these promising characteristics, the widespread adoption of Na-K-Sb photocathodes in photoinjector applications has been consistently hindered by fundamental challenges in material synthesis. Over the past decades, poor reproducibility and low success rates have resulted in significant variations of photoe-

missive properties between growths. These limitations primarily stem from three interrelated factors:

1. The exceptionally narrow stoichiometric window required for optimal photoemissive performance

2. The extremely low equilibrium vapor pressure of Na required for forming of the high-QE Na_2KSb phase

3. Insufficient control over critical deposition parameters, particularly alkali metal flux rates

1.2. Thesis Outline

To address these challenges, a new photocathode laboratory was established at Helmholtz-Zentrum Berlin in 2024, featuring a novel preparation chamber capable of simultaneous deposition of all three elements with improved flux stability. This thesis presents a comprehensive development program for Na_2KSb photocathodes as green photocathode for the SEALab SRF photoinjector.[14]

The primary objectives of this work are:

1. Preliminary experiments using conventional dispenser chambers to understand the basic growth mechanism of Na_2KSb photocathodes (December 2021- June 2023)

2. Commissioning of novel triple evaporation system (July 2023- August 2024)

3. Developing triple evaporation growth recipes for Na_2KSb photocathodes and establishing precise correlations between growth parameters, stoichiometry, and photoemissive properties through systematic experiments (September 2024- May 2025)

4. Demonstrating reproducible fabrication of high-QE Na_2KSb photocathodes with extended dark lifetime (June 2025- July 2025)

5. Validating photocathode performance through successful integration and operation in the SEALab photoinjector (July 2025)

The research methodology includes the preliminary development in existing dis-

penser growth chambers, followed by advanced optimization using the newly built triple evaporation system. Characterization techniques mainly include spectral response measurements of photoemissive properties and X-ray photoelectron spectroscopy of stoichiometry and chemical shifts. The successful transfer and characterization of two Na_2KSb photocathodes in the SEALab photoinjector during beam commissioning represents the ultimate validation of the developed methodologies.

This thesis is structured as follows: Chapter 2 covers the theoretical fundamentals of SEALab photoinjector physics and photocathode physics and chemistry. Chapter 3 details the experimental setups for photocathode growth, spectral response measurement, and XPS characterization. Chapter 4 discusses the preparation methodology and research findings for Na-K-Sb photocathodes. Chapter 5 introduces the first beam achievement in the SEALab photoinjector. Chapter 6 focuses on XPS measurements and the establishment of a comprehensive database for Na-K-Sb photocathodes, providing fundamental insights for future development.

2. Fundamentals

2.1. SEALab Photoinjector

Photoinjectors are critical for generating high-brightness electron beams required for advanced accelerator applications, including energy recovery linacs (ERLs),[10] ultrafast electron diffraction (UED)[11] and free electron lasers (FELs).[3,4] The primary types of photoinjectors developed for these purposes are DC photoinjectors,[15,16] normal conducting radio frequency (NCRF) photoinjectors,[17,18] superconducting RF (SRF) photoinjectors,[14,19] and DC-SRF photoinjectors.[20]

At HZB, a new generation of SRF photoinjector has been constructed under the SEALab project. Based on beam dynamics studies, the photoinjector consists of two main components: an SRF gun and an SRF booster. After years of dedicated commissioning, first beam was successfully achieved in the SRF gun in March 2025. The structure of this SRF gun is illustrated in Figure 2.1.

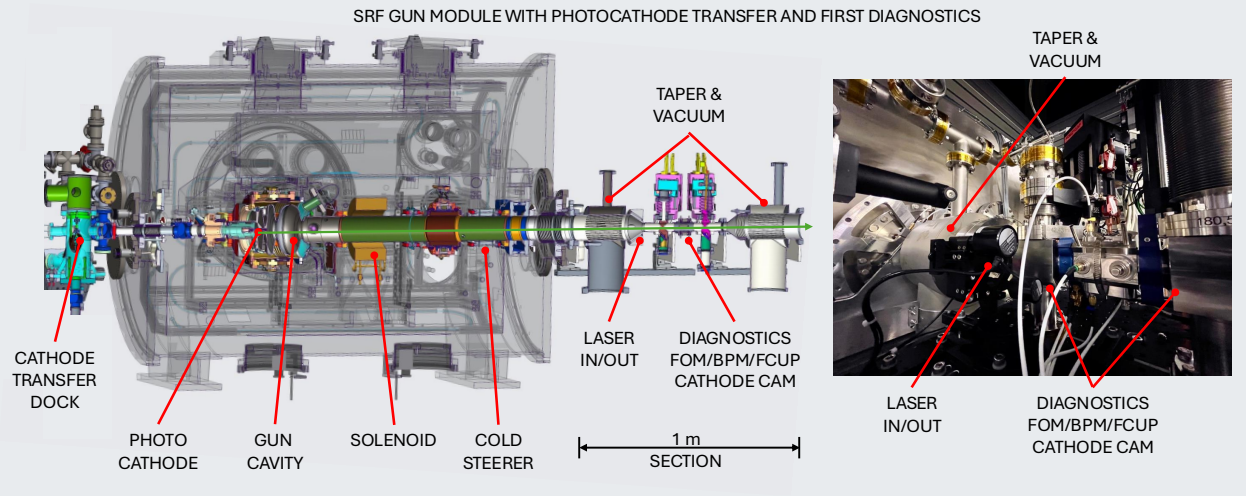


Figure 2.1: *SEALab SRF gun system for the first beam commissioning. Left: CAD drawing, Right: First meter of diagnostics beam line.*[14]

Prior to operation, a photocathode needs to be transferred into its operational position in the back wall of the gun cavity via the cathode transfer system (transfer

system 2).

For the first beam commissioning, a drive laser operating at a wavelength of 521 nm and a power of 2 W in continuous-wave (CW) mode was used, with a tunable repetition rate of up to 50 MHz. The laser is delivered to the SRF gun (see entrance in Figure 2.1b) through a 30-meter-long beam pipe, achieving a transmission efficiency of 85%.[14] A relay imaging system for optical transport and a variable beam-shaping aperture located near the cathode are employed to stabilize the beam against vibrations from nearby water cooling pumps.

During operation, the electron beam emitted from the photocathode is accelerated within the core of the SRF gun, a niobium (Nb) cavity designed for 1.3 GHz in CW operation. The superconducting state of the cavity is maintained via liquid helium cooling at 4 K. Upon exiting the cavity, beam-based alignment is conducted using a solenoid, and the beam position is adjusted in the X-Y plane by a cold steerer. Initial beam characterization is performed using a viewscreen (FOM), beam position monitors (BPMs), and a Faraday cup (FCUP) located within the first meter of the diagnostic beamline. The beam current emitted from the cathode is measured directly using a cathode bias power supply.

The SRF gun is a highly complex and integrated system, demanding meticulous design and engineering of all subsystems—including power supplies, vacuum, cooling, drive laser, cavity, solenoid, and steerer, and, most critically, their precise coordination.

2.2. Requirements of photocathodes

As a critical subsystem, the photocathode must be designed and operated in close coordination with all other components. Its performance and integration impose several specific requirements:

1) High Quantum Efficiency at visible wavelengths:

The photocathode must exhibit high quantum efficiency (QE $>1\%$) at the operational wavelength (521 nm at SEALab) to generate a high beam current within

the limited power budget of the drive laser system. A high QE at visible wavelengths reduces the demands on the optical components and increase the flexibility of the laser system, enables higher effective power on the cathode, and is essential for high-current operation. Alkali-antimonide photocathodes are the only materials applied to SRF photoinjectors that currently meet this requirement. However, their extreme sensitivity to residual gases—particularly oxygen and water vapor—necessitates an ultra-high vacuum (UHV) environment during both transfer and operation in the photoinjector. The liquid helium-cooled superconducting cavity is an advantage in this regard, as it helps maintain the UHV environment. For instance, K_2CsSb photocathodes have demonstrated high-current operation (3–4% QE at 532 nm) with month-long lifetimes in SRF guns.[19] Na_2KSb is a promising alternative, offering higher thermal stability and the potential for longer operational lifetime and greater robustness, which is anticipated to benefit the SEALab commissioning and operation. Its thermal stability also reduces the risk of material evaporation and contamination of the superconducting cavity.

2) Thermal Coupling and Substrate Choice:

Since the photocathode is located at the back wall of the superconducting cavity, efficient thermal management is crucial for transferring the heat from the photocathode out of the cryomodule. Insufficient heat transfer could raise the temperature of the superconducting cavity beyond its critical transition temperature. The photocathode subsystem must therefore maintain excellent thermal contact with the cooling system, which uses 80 K gaseous helium. As detailed in previous work,[21] the design of the cathode inserts and RF filters in the SEALab system can maintain the cathode temperature below 300 K under a total thermal load of 30 W. This load comprises 5 W of RF power dissipation from the cavity and up to 25 W of incident laser power, based on the assumption of a 1% QE photocathode to achieve the original ERL design goal of a 100 mA beam current.

Metallic molybdenum (Mo) was selected as the substrate due to its high thermal conductivity, excellent chemical stability in air, and adequate machinability. A

significant challenge, however, is polishing its surface to a roughness (Rq) of less than 10 nm due to the material's high hardness. Furthermore, the lattice mismatch between Mo and alkali-antimonide films prevents the epitaxial growth of single-crystal photocathodes. The surface roughness could increase the mean transverse energy (MTE) of emitted electrons. Despite these drawbacks, Mo remains the optimal substrate material, primarily due to its compatibility with the strict thermal requirements of the cooling system.

3) Mitigation of Multipacting and Field Emission:

The photocathode subsystem must be designed to avoid negatively impacting other subsystems. Specifically, the presence of photoemissive material on the side of the plug (parallel to the cavity wall) can exacerbate multipacting, while deposition on the sharp edges of the plug may cause field emission. To prevent these unfavorable effects, the photoemissive film must be strictly confined to the center of the plug, with no deposition on the sides or edges.

2.3. Photoinjector related Photoelectric Properties of Photocathodes

2.3.1. Quantum Efficiency

The quantum efficiency (QE) is the most critical photoelectric property of photocathode materials, defined as the ratio of the number of emitted electrons (N_{electron}) to the number of incident photons (N_{photon}), as expressed in Equation 2.1:

$$QE = \frac{N_{\text{electron}}}{N_{\text{photon}}} = \frac{I \cdot h \cdot c}{P \cdot e \cdot \lambda} \tag{2.1}$$

where I is the measured photocurrent (A), P is the power (W) of the incident light, λ is its wavelength (m), h is Planck's constant ($6.626 \times 10^{-34}\,\mathrm{J \cdot s}$), c is the speed of light ($2.998 \times 10^{8}\,\mathrm{m/s}$), and e is the elementary charge ($1.602 \times 10^{-19}\,\mathrm{C}$).

For the SEALab photoinjector at HZB, the maximum achievable beam current can be estimated from the QE of photocathode, given the driving laser's maximum power (25 W) and operational wavelength (521 nm). High-QE photocathodes are particularly beneficial for high-brightness applications such as ERLs.

It is important to note that QE depends not only on the photocathode material but also on the operational environment, including the driving laser wavelength. Therefore, QE is usually plotted as a function of wavelength, known as a spectral response curve. It is highly sensitive to the growth process as presented in Section 4.6.

2.3.2. Storage Lifetime

The storage lifetime of a photocathode depends on multiple factors, including the material itself and the environment, especially vacuum conditions. Alkali-antimonide photocathodes are highly sensitive to residual gases, particularly oxygen and water vapor, which limits their storage lifetime. In photocathode lab, this lifetime is measured in the growth chamber with UHV environment ($< 1 \times 10^{-10}$ mbar), by monitoring the QE decay over time and fitting it to an exponential decay model:

$$QE(t) = A \times \exp(-t/\tau) \tag{2.2}$$

where t is time, A represents the initial QE, and the time constant τ represents the calculated storage lifetime, defined as the time required for the QE to decay to $1/e$ (approximately 37%) of its initial value. A long storage lifetime is a necessary for practical application in a photoinjector. For instance, the cathode transfer process at HZB takes approximately four days to a week, requiring QE to remain stable.

In photocathode lab, the storage lifetime is measured under low illumination (on the order of μW). Under the UHV condition, as described in Section 3.2.2.1, the measured lifetime primarily reflects the "intrinsic stability" of the photocathode material, which is highly sensitive to the growth process. Consequently, it serves as a key parameter for recipe development and optimization. With an appropriate growth method, τ usually exceed 500 hours for Na_2KSb photocathodes, as to be discussed in Section 4.5.2.

It is crucial to distinguish storage lifetime from operational lifetime. The latter is measured within the photoinjector and is influenced by additional factors beyond vacuum conditions, such as high beam density, high field gradient, and incidents like multipacting, ion back-bombardment and field emission.

2.3.3. Photoemission Models

Photoemission models are essential for describing the photoemission process of a photocathode. Here, we focus on models for p-type semiconductors, as all alkali-antimonide materials demonstrating a QE exceeding 1% at 520 nm are p-type, for instance, Cs_3Sb, K_2CsSb and Na_2KSb.[22]

2.3.3.1. Three Step Model

The three-step model, first proposed by Spicer in 1960,[22] remains widely used for alkali-antimonide photocathodes as it provides a fundamental framework for interpreting spectral response data. A schematic diagram of this model is shown in Figure 2.2. The photoemission process is divided into three distinct steps: (1) photon absorption and electron excitation, (2) transport of excited electrons toward the surface, and (3) emission to vacuum.

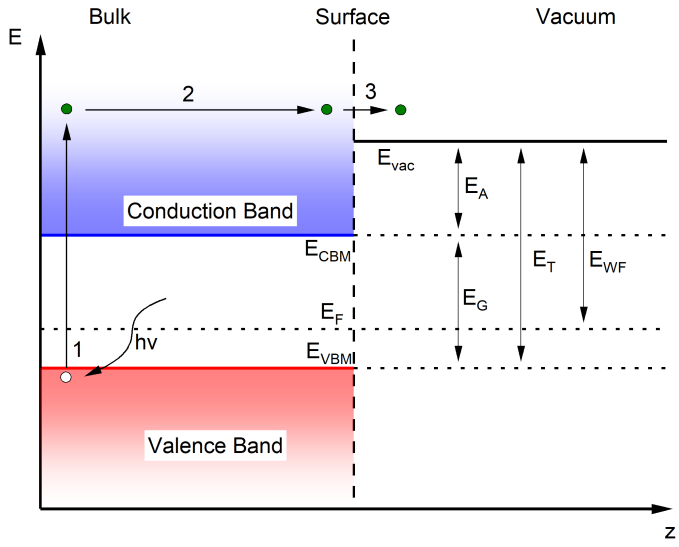


Figure 2.2: *Schematic of three step photoemission model, demonstrated with the band structure of a p-type semiconductor.*

Step 1: Excitation

In photocathode material, The photon flux density $J(x, h\nu)$ decays exponentially with depth (x) into the material:

$$J(x, h\nu) = J_0 \exp(-\alpha_{\mathrm{t}}(h\nu)x) \tag{2.3}$$

where J_0 is the incident photon flux density ([number of photons] $\mathrm{m}^{-2} \cdot \mathrm{s}^{-1}$).

An electron in the valence band absorbs the energy of an incident photon ($h\nu$) and is excited to a higher energy state. The total optical absorption coefficient (α_{t}) is divided into a productive part, α_{p}, representing transitions where the excited electron's energy exceeds the vacuum level (E_{vac}), and a non-productive part, α_{c}, for transitions where the final energy remains below E_{vac}.

Step 2: Transport

The excited electrons (hot electrons with $E_{\mathrm{electron}} > E_{\mathrm{vac}}$) travel toward the surface. During this transport, a fraction of these electrons lose energy through scattering processes (e.g., with phonon) and may fall below the vacuum energy level, becoming unable to escape.

Step 3: Emission

Electrons that reach the surface with kinetic energy greater than the vacuum level can be emitted into vacuum. Spicer combined the probabilities of steps 2 and 3 into an exponential escape probability function that also decays with depth:

$$P(x, h\nu) = B(h\nu) \exp(-\beta(h\nu)x) \tag{2.4}$$

where the parameters $B(h\nu)$ and $\beta(h\nu)$ depend on the photon energy. In metals, energy loss is dominated by efficient electron-electron scattering due to the high electron density. In semiconductors like alkali-antimonides, electron-electron scattering is negligible, and energy loss is primarily due to electron-phonon scattering.[23]

Based on experimental observations near the threshold energy, Spicer proposed

$\alpha_{\mathrm{p}} = C(h\nu - E_{\mathrm{T}})^{3/2}$, where C is a constant and E_{T} is the threshold energy (the sum of the band gap E_{G} and electron affinity E_{A}). The overall QE is obtained by integrating the contributions over all depths:

$$QE(h\nu) = \int_0^{\infty} \frac{\alpha_{\mathrm{p}} F(x, h\nu) P(x, h\nu)}{F_0} dx = \frac{B\alpha_{\mathrm{p}}}{\alpha_{\mathrm{t}} + \beta} = \frac{B(h\nu - E_{\mathrm{T}})^{3/2}}{(h\nu - E_{\mathrm{T}})^{3/2} + \gamma} \quad (2.5)$$

where $\gamma = (\alpha_{\mathrm{c}} + \beta)/C$. Assuming α_c, B, and β are constants for a given material, γ can be treated as a constant fitting parameter. Thus, only three parameters need to be fitted to the spectral response curve: E_{T}, B, and γ, making the model practical for application.

The Spicer model treats photoemission as a bulk effect, where excitation and transport within the material are crucial, rather than a purely surface phenomenon. As $h\nu$ increases, α_{p} becomes comparable to $\alpha_{\mathrm{c}} + \beta$, causing the QE to increase more slowly than α_{p}.

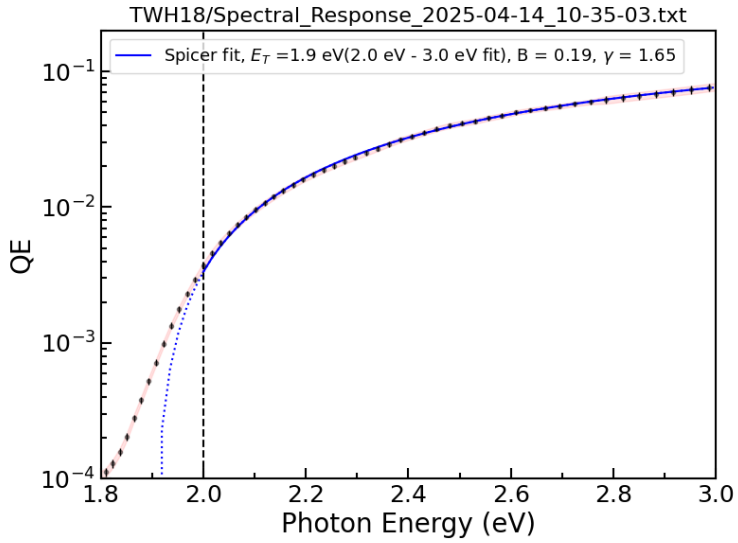


Figure 2.3: *An example of spectral response curve (TWH18) fitted with Spicer model.*

For our study of Na-K-Sb photocathodes, this model provides an good fit to the experimental spectral response curve for photon energies above approximately

2.0 eV (E_{T}+0.1 eV). The spectral response curve taken from TWH18 ($Na_{2.3}K_{1.0}Sb_{1.0}$) is fitted with Spicer model and shown as an example in Figure 2.3.

2.3.3.2. Urbach Model

Interestingly, in the lower photon energy region (1.8–1.9 eV in Figure 2.3), the experimental spectral response data diverge from the three-step model, exhibiting an exponential "tail" in quantum efficiency (QE) that requires a distinct fitting function. This "tail" is an universal feature observed in alkali-antimonide photocathodes.[24]

One common explanation is that the originally sharp valence band maximum (VBM) is broadened due to energy uncertainty, with additional density of states (DOS) from impurities or disorders distributed exponentially above the VBM. This phenomenon, known as the Urbach tail, was proposed to explain the exponential absorption edge in semiconductors:

$$\alpha(h\nu) = \alpha_0 \exp\left(\frac{h\nu - E_{\mathrm{G}}}{E_{\mathrm{U}}}\right), \quad h\nu < E_{\mathrm{G}} \tag{2.6}$$

where α_0 is a material-dependent coefficient, $h\nu$ is the photon energy, E_{G} is the band gap energy at 0 K, and E_{U} is the Urbach energy, which quantifies the degree of band edge broadening. The Urbach energy E_{U} is related to temperature and disorder, and can be expressed as $E_{\mathrm{U}} = k_{\mathrm{B}} T \sigma_T$, where k_B is the Boltzmann constant, T is temperature, and σ_T is a steepness parameter. According to Dow and Redfield's phonon theory,[25] σ_T is given by:

$$\sigma_T = \sigma_0 \frac{2k_{\mathrm{B}}T}{h\nu} \tanh\left(\frac{h\nu}{2k_{\mathrm{B}}T}\right) \tag{2.7}$$

where σ_0 is a temperature-independent constant. Near room temperature, σ_T varies slowly, and E_U can be approximated as proportional to $k_B T$.

To model the spectral response in the low-energy region, I similarly assume an exponential distribution of density of states ($g(E)$) above the VBM (Figure 2.4):

$$g(E) = \exp\left(\frac{-(E - E_{\text{VBM}})}{\Delta E(T)}\right), \quad E > E_{\text{VBM}} \tag{2.8}$$

where $\Delta E(T)$ represents the energy broadening of the valence band at VBM, which increases with temperature and impurity concentration, analogous to the Urbach energy.

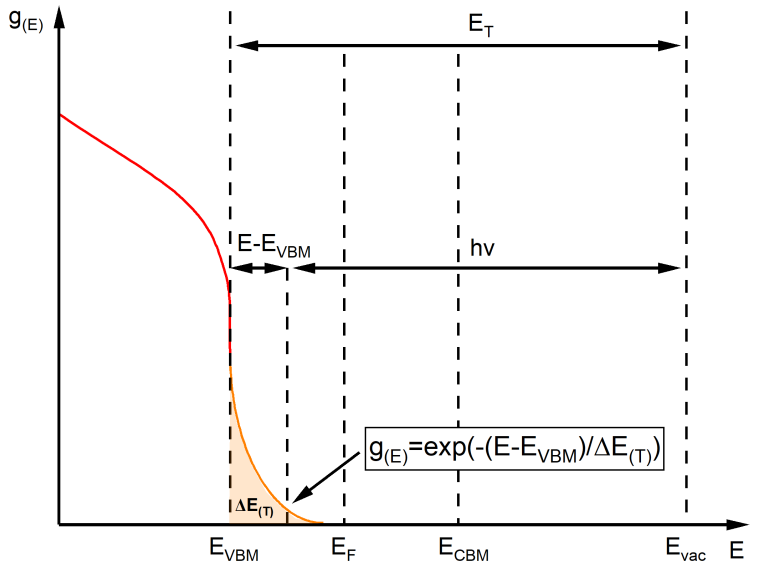


Figure 2.4: *Schematic of the density of states of a p-type semiconductor photocathode (e.g. K_2CsSb and Na_2KSb), with an exponential tail distributed above the VBM from impurities or disorders of the material.*

Assuming all states in this exponential tail are filled (occupancy $f(E) = 1$ below the Fermi level), and the productive absorption coefficient α_p is proportional to the number of electrons distributing $E_{\text{T}} - h\nu$ above E_{VBM} before excitation. For $h\nu < E_{\text{T}}$, this yields:

$$\alpha_{\text{p}}(h\nu) = D\int_{E_{\text{T}}-h\nu}^{\infty} \exp\left(\frac{-(E - E_{\text{VBM}})}{\Delta E(T)}\right) d(E - E_{\text{VBM}}) = D\Delta E(T)\exp\left(\frac{h\nu - E_{\text{T}}}{\Delta E(T)}\right) \tag{2.9}$$

where D is a constant. Since $\alpha_{\text{p}} \ll \alpha_{\text{t}} + \beta$ in this energy range, the QE is approximately proportional to α_{p}. Substituting into the three-step model (Equation 2.5)

gives:

$$QE(h\nu) = \frac{B\alpha_{\mathrm{p}}}{\alpha_{\mathrm{t}} + \beta} \propto \Delta E(T) \exp\left(\frac{h\nu - E_{\mathrm{T}}}{\Delta E(T)}\right), \quad h\nu < E_{\mathrm{T}} \tag{2.10}$$

For Na-K-Sb photocathodes, the Equation 2.10 reduce to the empirical fitting function for the exponential QE tail:

$$QE(h\nu) = \exp(a + b \cdot h\nu), \quad h\nu < E_{\mathrm{T}} \tag{2.11}$$

where a and b are fitting parameters, with $b = 1/\Delta E(T)$ and $a = \ln(QE(hv = E_{\mathrm{T}})) - bE_{\mathrm{T}}$, and $QE(hv = E_{\mathrm{T}})$ is the QE value at the threshold energy.

2.4. Alkali-Antimonides as Photoemissive Materials

This section provides an overview of various alkali-antimonide compounds, particularly Na-K-Sb system, as it is the focus of this study. In addition to the photoelectric emission properties, I also discuss their crystal structure, thermal stability, and the challenges encountered in the synthesis.

To address the challenges outlined in Section 2.1, photoemissive materials operating efficiently at visible wavelengths are essential. Among these, alkali-antimonide compounds are well known as photocathode materials demonstrating a QE over 1% at green wavelengths, making them a suitable choice for SEALab photoinjector. Properties of several alkali-antimonides are summarized in Table 2.1. Beyond the compounds listed, more complex multi-alkali-antimonides—such as the well-known S-20 photocathode ($Na_2KSb(Cs)$)—have been developed to achieve even higher QE. A general correlation emerges between macroscopic photoelectric properties and microscopic crystal structure: all high-QE, low-electron-affinity compounds in this family exhibit cubic crystal structures and are naturally p-type semiconductors due to alkali metal vacancies.

Table 2.1: *Summary of crystal structures, conductivity types, band gaps (E_G), electron affinities (E_A) and QE of common alkali-antimonide compounds*

Material	Crystal structure	Conductivity type	E_{G} (eV)	E_{A} (eV)	QE at 532 nm
Na_3Sb	hexagonal [a)]	n [a)]	1.1 [a)]	~ 2.4 [a)]	$< 0.1\%$ [a,h)]
K_3Sb	hexagonal [a,b)]	n [a)]	1.1 [a)]	~ 1.6 [a)]	$\sim 0.1\%$ [a,b,h)]
K_3Sb	cubic [a,b)]	p [a)]	1.4 [a)]	0.9 [a)]	$> 0.1\%$ [a,b,h)]
NaK_2Sb	hexagonal [c)]	n [h)]	-	-	$< 0.1\%$ [h)]
Na_2KSb	cubic [a,c)]	p [a,c)]	1.0[a)],1.1[e)]	1.0[a)],0.7[e)]	$\sim 5\%$ [h)]
Cs_3Sb	cubic[a,c)]	p [a)]	1.6 [a)]	0.45 [a)]	$\sim 5\%$ [d)]
Cs_2KSb	cubic [c)]	p [a)]	-	-	$\sim 8\%$ [h)]
CsK_2Sb	cubic [a,c)]	p [a)]	1.0 [a)],1.2 [e)]	1.1 [a)],0.7[e)]	$\sim 5\%$ [h)]

[a)] Ref.[22]; [b)] Ref.[26,27]; [c)] Ref.[28,29]; [d)] Ref.[30,31]; [e)] Ref.[32]; [h)] Experimental data at HZB.

2.4.1. Na-K-Sb Photocathode System

According to the X-ray powder diffraction results of Mccarroll,[28] as shown in Figure 2.5, the $Na_{3-x}K_xSb$ system can be divided into 6 phase zones as a function of gross K_3Sb content. In thermodynamic equilibrium state, the phase composition can be determined based on the chemical composition through the phase diagram and the lever rule. From left to right, the 6 phase zones including 4 signal phase zones and 2 double phases zones: (1) hexagonal phase of Na_3Sb; (2) mixed phase of Na_2KSb and Na_3Sb; (3) cubic phase of $(Na,K)_2KSb$; (4) mixed phase of $Na_{1.95}K_{1.05}Sb$ and NaK_2Sb; (5) hexagonal phase of $(Na,K)K_2Sb$; and (6) hexagonal phase of K_3Sb.

2.4.1.1. Mono-Alkali-Antimonides: Na_3Sb and K_3Sb

The Na-K-Sb system includes two mono-alkali-antimonides with hexagonal Na_3As-type structures: Na_3Sb and K_3Sb. As shown in Table 2.1, both exhibit low QE at 532 nm and have received only limited study, particularly Na_3Sb. Its only known use is as an intermediate, though very rare: P. Dolizy successfully transformed Na_3Sb films into the high-QE Na_2KSb phase by subsequent deposition of Sb and K.[33]

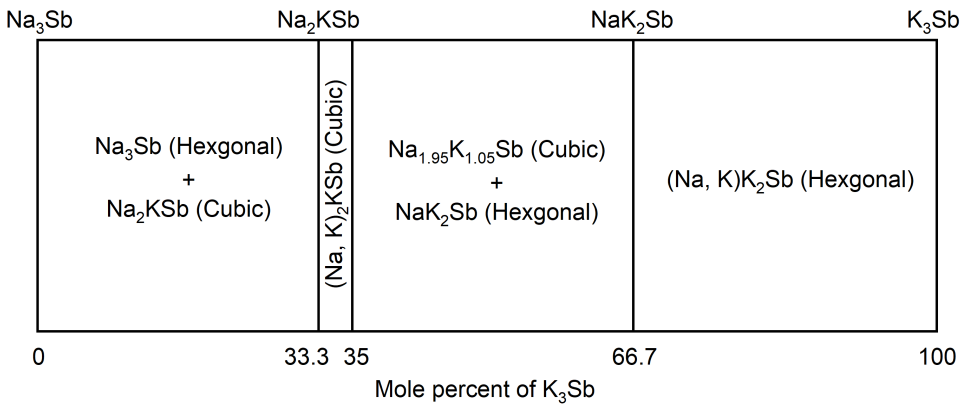


Figure 2.5: *Diagram showing the phases present in the $Na_{3-x}K_xSb$ system as a function of gross K_3Sb content.*[28]

K_3Sb has been more extensively studied due to its role as a common intermediate in synthesizing Na_2KSb and K_2CsSb photocathodes. It exhibits two polymorphs: a common hexagonal phase and a metastable cubic phase. The hexagonal is readily synthesized by depositing excess K onto Sb at elevated temperatures ($\sim$160 °C) and is relatively stable under thermal load and K excess. The cubic phase (p-type), initially reported by Sommer,[34] is observed to deliver higher QE up to 1% in green.[26] Mixtures of hexagonal and cubic K_3Sb can be synthesized at lower temperatures (e.g.room temperature to 100 °C) with moderate K deposition.[26,27] As an intermediate, these two polymorphs have different impacts on the synthesis of K_2CsSb photocathode: Schubert concluded that the conversion of K_3Sb to K_2CsSb proceeds most readily when the initial K_3Sb is in the metastable cubic phase rather than the stable hexagonal form.[27] However, the synthesis of pure cubic K_3Sb films remains poorly explored since Sommer's 1968 observation that its formation may be related to the participation of oxygen during growth[34].

2.4.1.2. Bi-Alkali-Antimonides: Na_2KSb and NaK_2Sb

This thesis focuses on the two bi-alkali-antimonides in the Na-K-Sb system: cubic Na_2KSb and hexagonal NaK_2Sb, with their crystal structures shown in Figure 2.6.

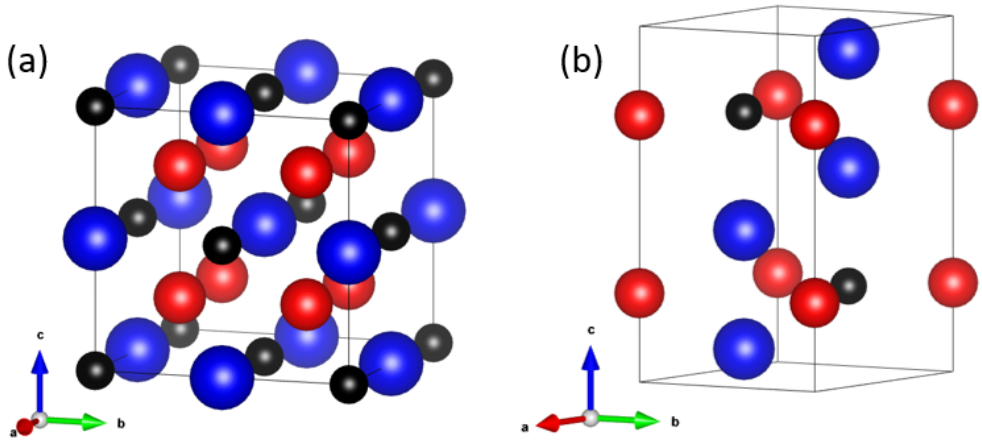


Figure 2.6: *Crystal structures of (a) cubic Na_2KSb and (b) hexagonal NaK_2Sb. Na atoms are shown in red, K in blue and Sb in black. Graphs is generated by VESTA.*[35]

Na_2KSb has a high-symmetry face-centered cubic (fcc) structure with a lattice parameter of a=7.72 Å.[28] The single-phase region exists from stoichiometric Na_2KSb down to approximately $Na_{1.95}K_{1.05}Sb$, with the lattice parameter expanding to 7.74 Å, as larger K ions substitute smaller Na ions. Sommer's early work[7] identified the optimal composition for high QE to be near the Na:K=2:1 ratio. In addition, considerably photosensitive Na-K-Sb layer only exists when Na:K from 2.5 to 1.0,[28] corresponding to stoichiometry near Na_2KSb single-phase region. This narrow stoichiometric window for peak QE performance contrasts with the broader range observed in the K-Cs-Sb system (Cs_3Sb to $K_{2.08}Cs_{0.92}Sb$),[29] making the reproducible synthesis of high-QE Na_2KSb films particularly challenging.

NaK_2Sb can be described as derivative of hexagonal K_3Sb where Na atoms partially substitute for K. This solid solution spans from pure K_3Sb (a=6.03 Å, c=10.64 Å) to approximately $Na_{0.99}K_{2.01}Sb$ (a=5.61 Å, c=10.93 Å), with Na atoms occupying specific positions as shown in red in Figure 2.6b. While no experimental evidence indicates high QE for NaK_2Sb at visible wavelengths, recent theoretical calculations using density functional theory (DFT) and many-body perturbation theory (MBPT) predict a direct band gap and electronic properties favorable for photoemission.[36,37] Consequently, the photoelectric properties of the NaK_2Sb

phase are also investigated in this work.

2.4.2. Thermal Stability of Na-K-Sb Compounds

The thermal stability of alkali-antimonide photocathodes is a critical property for their practical application and for the reaction kinetics. In a seminal study, P. Dolizy and F. Groliere (1986) systematically investigated the dissociation energies of various alkali-antimonide phases to quantify their thermal stability.[38]

Their experimental method involved depositing alkali-antimonide films on transparent glass substrates and heating them to elevated temperatures. They used the difference in optical absorption rates between the original phase (e.g., K_3Sb) and its dissociation products (e.g., K_2Sb) to evaluate the reaction progress. By measuring the change in absorption over time, they calculated the reaction rates and determined the dissociation energy for each alkali-antimonide film.

Their results, summarized in, Table 2.2 revealed a clear trend: the thermal dissociation energy (Φ, in kJ·mol^{-1}) decreases linearly with increasing alkali atomic radius (r_a, in Å), following the relationship:

$$\Phi = -20 r_\mathrm{a} + 81 \tag{2.12}$$

Furthermore, within the Na-K-Sb system, Dolizy and Groliere found that dissociation energy increases with Na content. To experimentally compare the stability of Na_2KSb and NaK_2Sb, they subjected both compounds to isothermal annealing at 180 °C and 200 °C. At 180 °C, Na_2KSb remained highly stable, while NaK_2Sb degraded significantly (only 60–70% remained after 120 minutes). At 200 °C, Na_2KSb retained considerable stability, whereas NaK_2Sb almost completely dissociated within the same duration.

These experiments demonstrate that the dissociation energy (Φ) of Na_2KSb is significantly higher than that of NaK_2Sb, resulting in a markedly lower dissocia-

Table 2.2: *Summary of the dissociation energies and temperatures of various alkali antimonides.*[38]

Compound	Cs_3Sb	K_3Sb	NaK_2Sb	Na_2KSb	Na_3Sb
$\Phi\,(\mathrm{kcal}\cdot\mathrm{mol}^{-1})$	29.6	33.7	∼37	40.5	44.6
$\theta_m\,(^\circ\mathrm{C})$	117	170	-	257	309

tion rate. This relationship is quantitatively described by the Arrhenius equation:

$$k = A \exp\left(\frac{-\Phi}{RT}\right) \tag{2.13}$$

where k is the rate coefficient of their dissociation reaction, A is the pre-exponential factor, R is the universal gas constant, T is the absolute temperature.

Based on these studies on thermal stability and the photoelectric properties, it can be conclude that Na_2KSb is a photocathode material with high thermal stability in the alkali-antimonide family, making it particularly suitable for applications demanding prolonged operational lifetime under thermal load.

2.4.3. Na_2KSb Synthesis Method

The synthesis of Na_2KSb photocathodes has historically relied on sequential deposition methods, as reported in prior studies.[9,34] The established procedure consists of four primary steps: (1) Deposition of a 20 nm Sb film at a substrate temperature of 180 °C. (2) K deposition onto the Sb film at 160 °C until the QE plateaus. (∼0.1% at 532 nm), indicating the formation of K_3Sb phase. (3) Na deposition onto the K_3Sb film at 220 °C. The process is monitored until the QE peaks and suddenly begins to decline, signaling the formation of Na_2KSb phase followed by unavoidable Na oversaturation. Halting the reaction precisely at the ideal Na:K stoichiometric ratio of 2:1 has proven extremely challenging. (4) Fine-tuning through alternating depositions of small amounts of Sb and K at 160 °C to restore QE and optimize the stoichiometric ratio towards the desired composition.

In contrast, the synthesis of Cs-K-Sb photocathodes employs a comparatively

simpler sequential recipe: (1) Deposition of a 10 nm Sb film at 100 °C. (2) K deposition at 100 °C until the QE plateaus or stop at an certain thickness. (3) Cs deposition at 90 °C until the QE reaches a stable maximum.[39]

The comparative synthesis methods reveals a significant difference in process complexity. The Cs-K-Sb system allows for optimization in a quasi-static, controlled manner, whereas the Na-K-Sb process is widely known as difficult to control, particularly during the Na substitution stage (step 3). This challenge arises from the extremely low equilibrium vapor pressure of Na and a narrower optimal stoichiometric window.[9]

To develop more efficient and reproducible synthesis recipes for Na-K-Sb, a fundamental understanding of the underlying reaction thermodynamics is essential.

2.4.4. Thermodynamics of Na_2KSb Synthesis

The thermodynamic principles governing Na_2KSb and K_2CsSb synthesis were intensively studied by B. Erjavec in the 1990s.[40,41] Their work included calculating the standard Gibbs free energy change ($\Delta G^0 T$) and equilibrium constants (K_p) for key reactions using the standard enthalpy of formation (ΔH^0_{298}) and standard entropy (S^0_{298}):

$$\Delta G^0 T = \Delta H^0_{298} - T \Delta S^0_{298} \tag{2.14}$$

$$\log K_\mathrm{p} = \frac{\Delta S^0_{298}}{2.3R} - \frac{\Delta H^0_{298}}{2.3RT} \tag{2.15}$$

where R is the universal gas constant ($1.987\,\mathrm{calK^{-1}mol^{-1}}$) and T is the absolute temperature.

For mono-alkali-antimonide formation (e.g., K_3Sb), the addition reaction and its associated K equilibrium vapor pressure (p_K) are considered:

$$\mathrm{K_2Sb}(s) + \mathrm{K}(g) \rightarrow \mathrm{K_3Sb}(s) \tag{2.16}$$

For bi-alkali-antimonide synthesis (corresponding to step 3 in sequential Na_2KSb deposition), the substitution reaction and its equilibrium vapor pressure ratio (p_K/p_{Na}) are considered:

$$K_3Sb(s) + 3Na(g) \rightarrow Na_3Sb(s) + 3K(g) \tag{2.17}$$

Calculated values of ΔG_T^0 and equilibrium vapor pressures are summarized in Table 2.3. For mono-alkali-antimonide, the equilibrium vapor pressures at 200 °C are $p_{Na} = 5.1 \times 10^{-11}\,\mathrm{mbar}$ for Na_3Sb and $p_K = 5.4 \times 10^{-7}\,\mathrm{mbar}$ for K_3Sb. For bi-alkali-antimonide, the equilibrium ratio p_K/p_{Na} for the substitution reaction in the Na-K-Sb system at 200 °C is approximately 230. While, this ratio is much lower in Cs-K-Sb system, where $p_K/p_{Cs} \approx 0.11$ at 100 °C.

Table 2.3: *Summary of equilibrium vapor pressure (mbar), ratio of various alkali antimonides.*[40,41]

Reaction	$\Delta G_T^0\,(\mathrm{calmol}^{-1})$	Equilibrium vapor pressure, ratio
$NaSb(s) + 2Na(g) \rightarrow Na_3Sb(s)$	-83400+55.1T	$\log p_{Na} = 9.0 - 41700/(2.3RT)$
$K_2Sb(s) + K(g) \rightarrow K_3Sb(s)$	-34000+29.5T	$\log p_K = 9.5 - 34000/(2.3RT)$
$K_3Sb(s) + 3Na(g) \rightarrow Na_3Sb(s) + 3K(g)$	-16300+2.1T	$\ln p_K/p_{Na} = -0.35 + 5450/(RT)$
$K_3Sb(s) + 3Cs(g) \rightarrow Cs_3Sb(s) + 3K(g)$	6700-3.4T	$\ln p_K/p_{Cs} = 0.74 - 2230/(RT)$

These thermodynamic data reveal a critical challenge in Na_2KSb photocathode synthesis: the extremely low equilibrium vapor pressure of Na necessitates a high p_K/p_{Na} ratio to maintain the phase stability of Na_2KSb. However, considering the reality, maintaining such a high ratio is neither efficient nor realistic. Unlike the Cs-K-Sb system—where Cs and K substitution is reversible—the substitution of K by Na is almost "irreversible" under typical growth temperatures. This irreversibility prevents the fine-tuning of stoichiometry and the optimization of QE through quasi-static processes that rely on equilibrium vapor pressure (Section 4.1.4). Consequently, achieving highly reproducible Na_2KSb photocathodes ne-

cessitates a deposition method capable of precise kinetic control, as developed in Section 4.2.1.

2.5. Challenges in Na-K-Sb Synthesis

As described in last section, among the (multi-)alkali antimonide photocathodes, Na-K-Sb films exhibit quantum efficiency (QE) comparable to that of Cs-K-Sb in the visible range.[8] Additionally, Na-K-Sb photocathodes demonstrate superior thermal robustness compared to Cs-K-Sb, making them suitable for high-current operations, aligning with the goals of ERL applications.[9] However, the widespread adoption of Na-K-Sb photocathodes in photoinjectors has been limited by low synthesis success rates and poor reproducibility, causing significant QE variations between film growths. These challenges arise from three key factors:

(1) Stoichiometric Sensitivity:

High QE is confined to a narrow stoichiometric range. Both theoretical and experimental studies indicate that the Na_2KSb phase primarily contributes to QE, with high photosensitivity achievable only within specific Na/K (2.5–1.0) molar ratios under alkali-sufficient conditions,[22] while deviations from this window severely degrade performance.

(2) Reaction Kinetics:

Na over-saturation remains a persistent issue, as Na readily substitutes for K even in low vapor pressure.[40] This substitution is nearly irreversible under standard growth conditions, rendering the final composition highly sensitive to reaction kinetics (temperature and time). The narrow stoichiometric window for Na_2KSb formation further exacerbates reproducibility challenges.

(3) Uncontrolled Alkali Flux:

Many synthesis methods rely on alkali dispensers, which exhibit large flux variations and unpredictable decay with time, likely due to inconsistencies in product manufacture, mounting/contact resistance, and degassing duration.

Due to the difficulties and uncertainties mentioned above, experiments often highly rely on operators' experience—factors that are difficult to standardize across laboratories. Consequently, growth optimization often follows trial-and-error approach, though time consuming, yielding low reproducibility and limited knowledge deepening.

Despite these challenges, our lab has its unique advantages through a combination of rigorous effort and recent improvements in alkali source technology:

(1) In-situ XPS:

As to be described in Section 3.4, XPS provides critical insights into contamination and stoichiometry, enabling rapid and accurate diagnosis of problems in film growth, especially for non-photosensitive films, as a common situation during new recipe development. This ensures that each experiment yields valid data for further optimization.

(2) Triple evaporation chamber with the controllable alkali sources:

The new chamber equips effusion cell loaded with SAES AlkaMax pills for alkli source, which deliver more stable alkali flux (as measured by QCM in Section 3.2.2), enabling precise growth parameter control.

These technical advancements establish the foundation for quantitative growth parameter optimization and provided the basis for all the results presented in this study.

3. Experimental methods

3.1. Substrate Preparation

Molybdenum (Mo) substrates were selected for film growth in this study due to their high thermal and electrical conductivity, making them suitable for high-current operation in RF photoinjectors. Additionally, Mo's high melting point (2623 °C) minimizes its diffusion into photocathode films, and its compatibility with alkali antimonides film has been well studied by previous researchers.[42,43,44]

As illustrated in Figure 3.1a, an all-Mo plug integrated with a flag-style sample holder was used for routine experiments. This type of substrate was employed for nearly all recipe development in this work, as it withstands repeated surface cleaning at higher temperatures than the gun-compatible Mo plug, as called real-Mo plug (Figure 3.1b). Its substrate is secured to the holder via a Cu-Be alloy crown-shaped spring, specially designed for photocathode transfer to SEALab.[45]

The Mo substrate was mechanically polished sequentially with diamond paste (6, 3, and 1 μm) and finished with a 0.05 μm OP-U silica suspension to achieve a smooth surface. Subsequent ultrasonic cleaning in acetone and isopropanol (10 min each), followed by ionized nitrogen drying, removed residual polishing compounds and organic contaminants.

White-light interferometry revealed a surface roughness (R_q) of $\sim$10 nm at the plug center as shown in Figure 3.1c and d. Despite being made of high-purity molybdenum and finely polished, relatively deep and wide scratches are still visible in random direction. As measured by AFM, the large scale scratch in the top left corner of Figure 3.1f is approximately 100 nm in depth and 600 nm in width.

Additionally, surface particles were observed in Figure 3.1d and e. Dry ice cleaning (CO_2 flakes + high-pressure N_2) could be a solution to remove these surface contamination, however, at the risk of damaging the edge of the plug.

Before going in the deposition chamber, the Mo plug is placed in 0.1 M citric

acid in ultrasonic bath for 10 minutes to dissolve the surface oxide and cleaned with de-ionised water to remove the solution. Then it is cleaned with ultrasonic bath in acetone and isopropanol and blown dry with nitrogen and transfer into the preparation chamber, where the Mo plug is heated to 550 °C (all Mo plug)/230°C (real Mo plug) and sputtered with argon (Ar) ions to ensure surface cleanliness. This process is repeated until no contamination peaks, such as oxygen (O), carbon (C) are detected in the XPS spectrum.

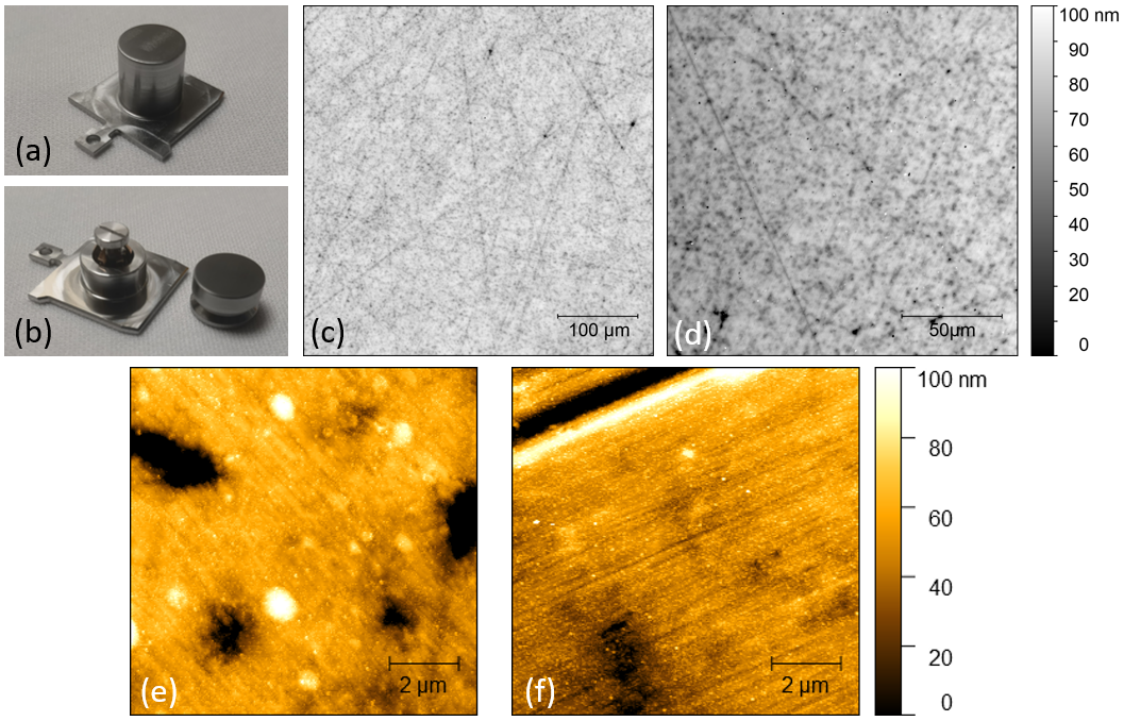


Figure 3.1: *Mo substrates and their surface roughness measurements: Pictures of all-Mo plug for recipe development (a) and real-Mo plug (b) designed for SEALab; white light interferometry (WLI) images of real Mo plug in (c) 20x magnification and (d) 50x magnification; (e) and (f) for atomic force microscopy (AFM) images of real Mo plug in 10 µm x 10 µm area.*

3.2. Na-K-Sb Photocathodes Growth Chamber

This section describes the two ultra-high vacuum (UHV) preparation chambers used for the growth of Na-K-Sb photocathodes in this thesis: the dispenser chamber and the triple evaporation chamber. The dispenser chamber was used for the

experiments presented in Section 4.1, while the triple evaporation chamber was used for the rest of the work.

3.2.1. Dispenser Chamber

Since 2014, a UHV system has been successfully used for the growth of Cs-K-Sb photocathodes.[39] A detailed description of this system can be found in the PhD thesis of Martin Schmeisser (2019).[46] Since 2019, several upgrades have been implemented to this system, as shown in Figure 3.2:

Vacuum system: The original vertical manipulator was replaced with a new one (UHV Design) with a micro-stepper motor for finer sample positioning and reduced residual gases production during the movement. The initial pump was also upgraded to a combination of a scroll pump and a turbo-molecular pump (Pfeiffer HiCube).

Evaporation system: The anode was separated from the deposition aperture to reduce measurement error and increase flexibility in experiments. The current feedthroughs for the alkali dispensers were redesigned for better structural rigidity, ensuring stable source positioning.

For this study on Na-K-Sb photocathodes, the original Cs dispensers were replaced with Na dispensers. The experimental configuration in the preparation chamber is showing in Figure 3.2: An antimony (Sb) effusion cell, loaded with 99.999% purity Sb beads (Alfa Aesar), is positioned 50 mm from the sample. Operated at 400 °C, it provides a constant deposition rate of 0.2 Å/s, as calibrated by a quartz crystal microbalance (QCM) at the sample position. Following Sb deposition through an 8 mm diameter aperture, the sample is transferred vertically via the manipulator to the position in front of the Na and K dispensers, where Na and K can be deposited either sequentially or simultaneously through a 5 mm diameter aperture. Each alkali metal is evaporated using two SAES dispensers, which are mounted on current feedthroughs and positioned 60 mm from the sample at a 30-degree angle.

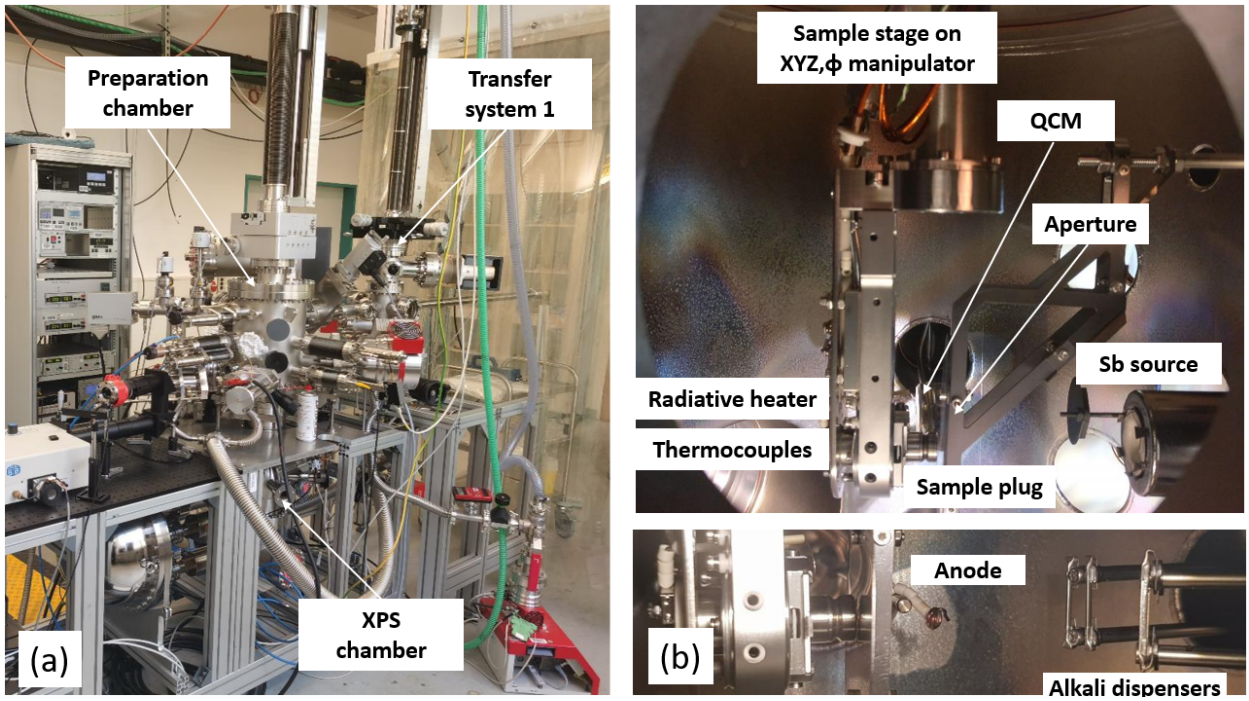


Figure 3.2: *(a) Photo of the UHV system in the photocathode lab (as of August 2023), including the preparation chamber, XPS chamber, and transfer system 1. (b) Internal view of the preparation chamber.*

However, a significant limitation of this chamber's design is the vertical separation of the sources: the Sb effusion cell and the QCM are on one level, while the alkali dispensers are on a lower level. This geometry complicates recipe development and prevents the deposition rate measurement of alkali metals. These constraints have hindered systematic parameter studies and made the reproducible growth of high-QE Na-K-Sb photocathodes extremely challenging. To overcome these limitations, a new triple evaporation chamber was designed and commissioned within the photocathode lab as described in next section.

3.2.2. Triple Evaporation Chamber

In June 2023, a cyberattack on HZB paralyzed the laboratory control systems. And the photocathode team decided to use this time to move the photocathode lab closer to the SEALab facility, thereby simplifying future cathode transfers, and to construct a new triple evaporation system designed to overcome the limitations of

the previous chamber. After a year of dedicated commissioning, the new chamber was finally in operation by June 2024.[47] Following three months of testing and optimization, the first high-performance Na-K-Sb photocathode (TWH11-2) with a QE exceeding 5% was successfully synthesized in September 2024. Following I introduce the key features of the new chamber.

3.2.2.1. Ultra-high Vacuum

The triple evaporation chamber uses the same pumping system as the dispenser chamber, including a primary pump (Pfeiffer HiCube), a main turbo pump, an ion getter pump (IGP), and a non-evaporable getter (NEG) pump.[39] Following a standard vacuum commissioning procedure—including chamber baking, activation of the IGP and NEG pumps, and degassing of the Sb, K, and Na sources—the preparation system achieves a base pressure below 1×10^{-10} mbar. The residual gas analysis (RGA) spectrum in Figure 3.3, recorded during a photocathode storage lifetime measurement, confirms a low partial pressure of residual gases (e.g., H_2O, N_2/CO, CO_2). The oxygen signal (amu=32) is negligible and buried in the background noise, indicating an excellent vacuum environment in the chamber.

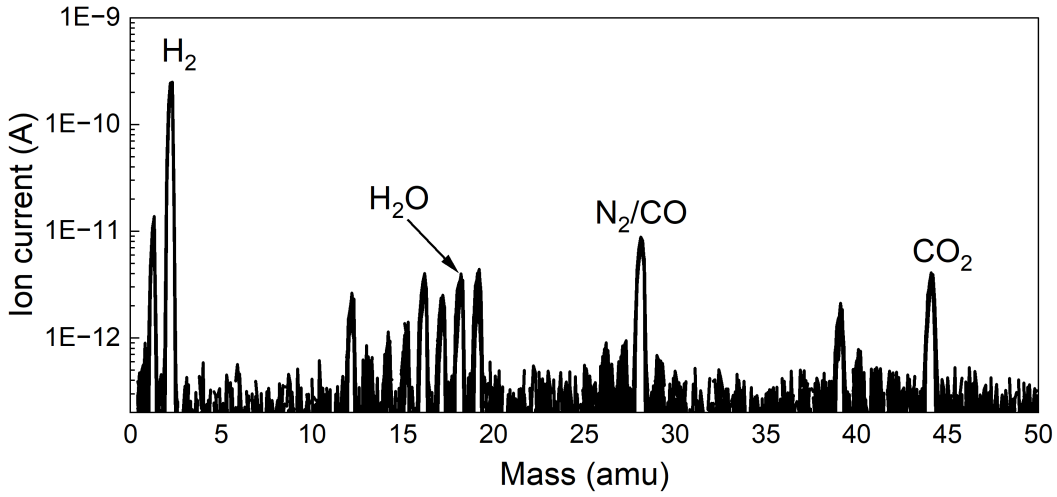


Figure 3.3: *Residual gas analysis (RGA) spectrum for triple evaporation chamber, measured on 19 February 2025, showing low partial pressure of residual gases.*

3.2.2.2. Deposition Geometry

The most significant improvement of this system is its capability for simultaneous deposition of three elements. The source configuration is illustrated in Figure 3.4: Sb is supplied by a thermal cracker cell (TCC) located 148 mm from the substrate at a 52° angle from the surface normal. The cell is loaded with 99.999% purity Sb beads (Alfa Aesar). And Na and K are evaporated from effusion cells positioned 60 mm from the substrate (distance is adjustable) at a 30° angle. Each cell is loaded with five SAES AlkaMax pills.

During growth, an aperture with an 8 mm diameter bevelled-edge hole is placed in front of the 10 mm diameter substrate plug. This confines the deposited material to the plug's center, mitigating multipacting and field emission risks in the photoinjector, as discussed in Section 2.1.

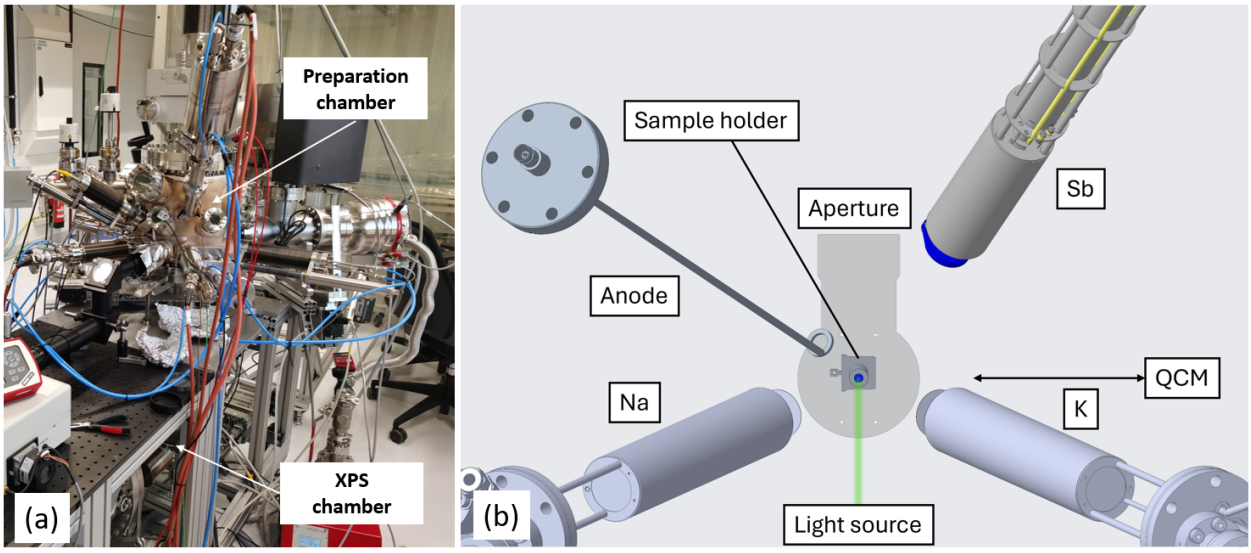


Figure 3.4: *(a) Photo of the newly built triple evaporation chamber for Na-K-Sb photocathode preparation. (b) Schematic of the deposition geometry. A water-cooled quartz crystal microbalance (QCM) can be moved into the sample position to calibrate deposition rates.*

The growth process is monitored in-situ via photoemission. Initially, a 520 nm laser provides high illumination power to detect the small QE. For detailed spectral response measurements, the light source is later switched to the to a Xenon

lamp and monochromator setup, enabling QE measurements across a 370–700 nm range.

3.2.2.3. Deposition Rate Measurement

The use of AlkaMax pills in effusion cells offers significant advantages over traditional dispensers, including extended operational lifetime and superior control over evaporation rates. This is particularly critical for Na, whose flux must be carefully regulated during Na-K-Sb growth, as discussed in Section 4.3.2. A single SAES Na pill contains 10 mg of sodium. With five pills loaded in effusion cell, the total available Na content is 50 mg—more than a 10 times increase compared to the 4.4 mg provided by two dispensers. Experimental confirms that this content is sufficient to grow over fifteen 50 nm Na-K-Sb films. Furthermore, the effusion cells provide exceptional temperature stability ($\pm$0.1 °C), resulting in more stable evaporation rate from Na pills. This is crucial for the success of the experiment since even minor deviations of a few degrees in the crucible temperature can shift the Na flux outside the optimal window required for Na_2KSb synthesis.

To ensure reproducibility, the deposition rates of Sb, Na, and K are calibrated before each growth using a water cooled QCM (20°C) positioned at the substrate location. The element-dependent parameters used for the QCM are listed in Table 3.1.

Table 3.1: *Parameters setup for QCM calibration (source: KJLC FTC-2800 operation manual).*

Element	Density ($\mathrm{g/cm^3}$)	Acoustic impedance ($10^5\,\mathrm{g\cdot cm^{-2}s^{-1}}$)
Sb	6.62	11.49
Na	0.97	1.84
K	0.86	0.87

The calibration sequence follows Sb, Na and K. The Sb deposition rate from the TCC at a crucible temperature of 420 °C is highly stable, maintaining 0.01Å/s

from the 5th (TWH14) to the 10th (TWH17) growth. During the measurement the thickness is recorded every 60 seconds after temperature stabilization, and the whole measurement takes 20 to 30 minutes, as shown in Figure 3.5a.

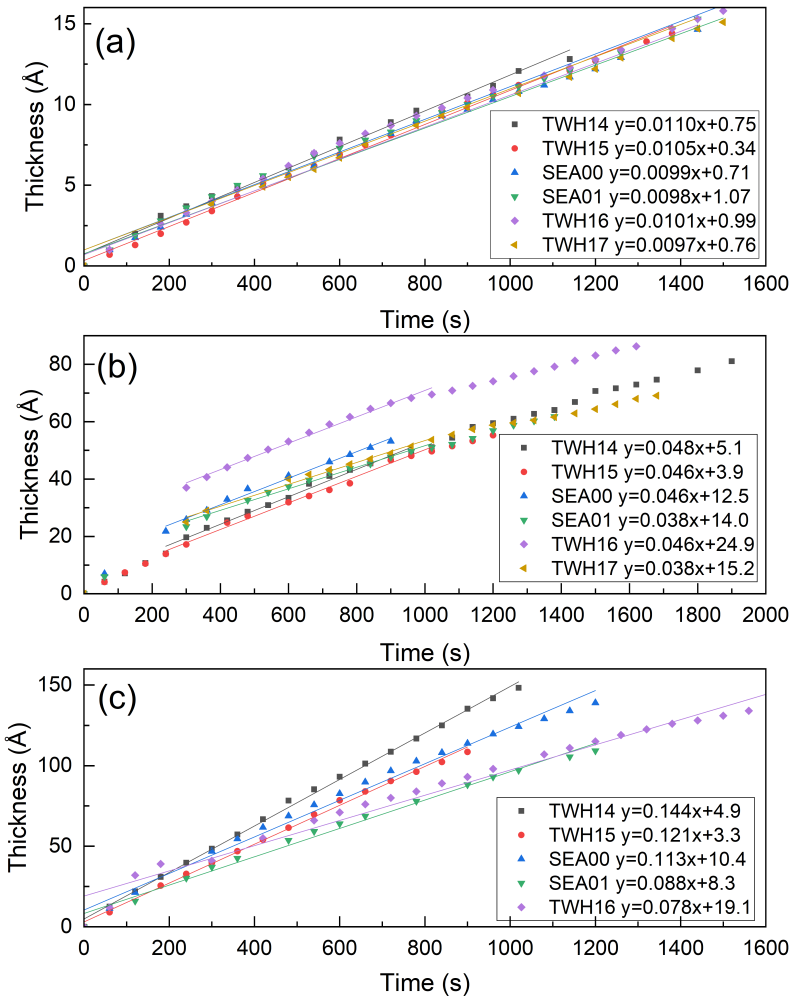


Figure 3.5: *Deposition rates calibrated by QCM for consecutive growths (TWH14 to TWH17) at constant crucible temperatures: (a) Sb at 420 °C, (b) Na at 375 °C, and (c) K at 370 °C.*

While, Na deposition rate measurement is the most complicated among the three elements-pure Na does not stick to a clean QCM crystal in UHV, preventing direct measurement. Therefore, the Na rate is inferred from the mass increase during the reaction of Na with a pre-deposited 2 nm Sb layer on the QCM. While this indirect method yields noisier data, as shown in Figure 3.5b, the calculated

deposition rate shows minor variations between growths.

The K deposition rate is measured after Na. A gradual decrease of 10-20% is observed between consecutive growths, as shown in Figure 3.5c. To compensate, the crucible temperature must be gradually raised after each use (approximately 4.5 hours of operation per growth) to maintain a consistent flux, as detailed in Table 3.2.

Table 3.2: *Crucible temperature settings for six consecutive Na_2KSb growths.*

Sample	Crucible temperature (°C)			Sample	Crucible temperature (°C)		
	Sb	Na	K		Sb	Na	K
(1) TWH14	420	372	370-375	(2) TWH15	420	373	375
(3) SEA00	420	375	377	(4) SEA01	420	377	378-380
(5) TWH16	420	379	381	(6) TWH17	420	381	383

3.2.2.4. Film Thickness Estimation

The final film thickness is a critical parameter, as it must exceed the electron attenuation length to maximize QE. While X-ray reflectivity (XRR) is the standard technique for measuring alkali-antimonide film thickness,[48] it is not available in the triple evaporation chamber. Therefore, the Na_2KSb film thickness is estimated from the calibrated Sb deposition, multiplied by a volume expansion factor of 3.8 as shown in Table 3.3.

There are two reasons to rely on Sb deposition rate to estimate the film thickness-stability and sticking coefficient: Sb is evaporated from pure Sb beads in TCC, provides a highly consistent deposition rate across growth runs. In addition, the QCM is cooled to 20°C, while the growth is at the substrate temperature of 110°C. Sb has a high desorption temperature ($\sim$400 °C), resulting in a sticking coefficient of 1 at the growth temperature, which has been cross-calibrated with XRR.[48] In contrast, alkali metals have low desorption temperatures, and their temperature-dependent sticking coefficients are unknown, making their direct QCM readings unreliable for thickness estimation.

Table 3.3: *Crystal structure data and volume expansion factors for common alkali-antimonides (source: Materials Project[49]).*

Compound	Structure	Unit cell volume (Å^3)	Sb position	Volume expansion factor
Sb	-	181.5	6c	1.0
Na_3Sb	hex	237.3	2c	3.9
Na_2KSb	cubic	463.7	4a	3.8
NaK_2Sb	hex	298.0	2c	4.5
K_3Sb	hex	338.2	2c	5.8
CsK_2Sb	cubic	639.4	4a	5.3

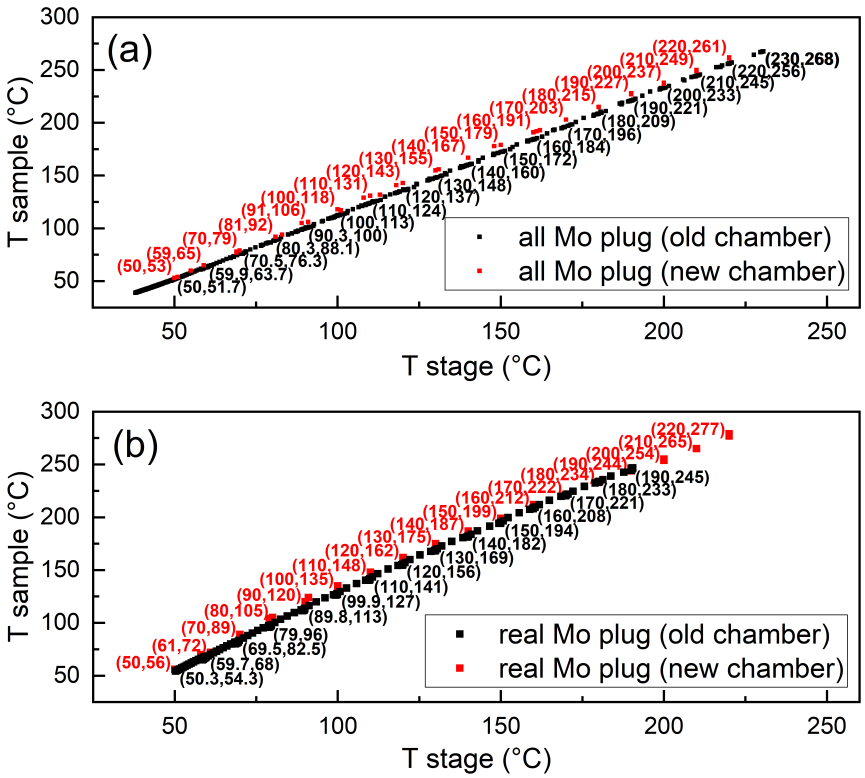


Figure 3.6: *Temperature calibration curves for (a) the all-Mo plug and (b) the real-Mo plug.*

3.2.2.5. Substrate Temperature Calibration

In the experiments, the substrate surface temperature (T_{Sample}) is not measured directly but is calibrated from the stage temperature (T_{Stage}). The relationship

between these two was calibrated by attaching a thermocouple to the surface of a dummy plug (Figure 3.6). For consistency, all temperatures reported in subsequent experimental sections refer to the stage temperature.

3.3. Spectral Response Setup

Spectral response measurements characterize the QE of a photocathode as a function of the incident light wavelength. The reliability of this measurement is critical, as the QE curve is used to fit photoemission models and determine photoemissive properties such as the threshold energy, as detailed in Section 2.3.3.

The experimental setup, initially commissioned by Hans Kirschner,[50] was recently upgraded by Jonas Dube in 2025. As shown in Figure 3.7, white light from the Xe arc lamp passes through the monochromator to generate monochromated light in selected wavelength; alternatively, a diode laser can be guided into the system for higher power and sensitivity. The light is then split by a 50:50 beamsplitter (BSW16, Thorlabs), directing one beam to the photocathode in the preparation chamber and the other to the photodiode for simultaneous power monitoring. The emitted photocurrent is collected by an anode and measured with pA-meter Keithley 6487 with a bias voltage of 150 V.

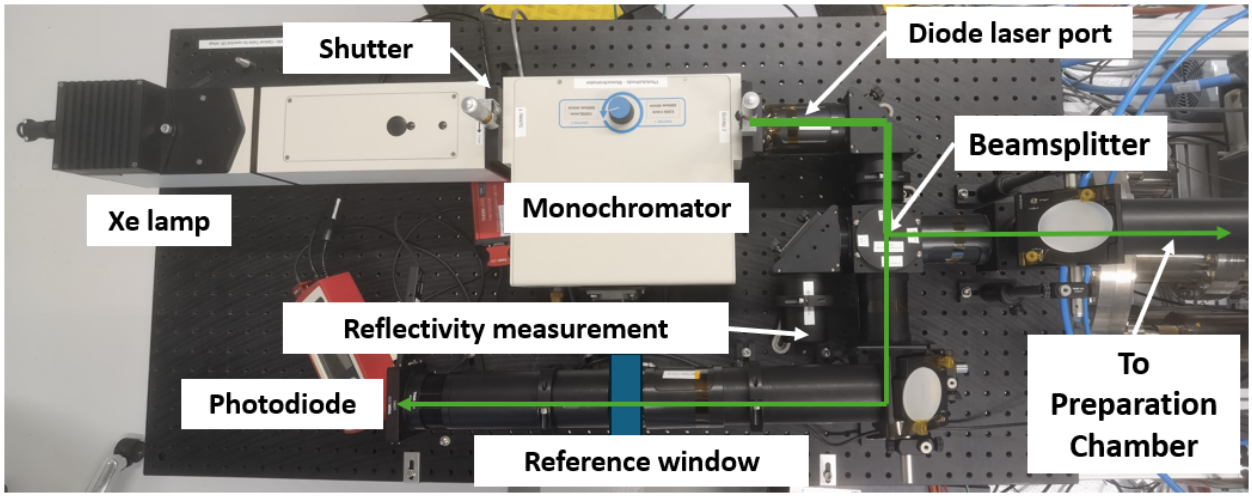


Figure 3.7: *Schematic of the upgraded spectral response measurement setup.*

For Na-K-Sb photocathodes, the spectral response is typically measured in vis-

ible range (370–700 nm). The QE and its uncertainty (ΔQE) are calculated as follows:

$$QE(\lambda) = \frac{1240(\text{eV·nm}) \cdot (I_{\text{ph}}(\lambda) - I_{\text{dark}})}{\lambda \cdot (P_{\text{ph}}(\lambda) - P_{\text{dark}})} \tag{3.1}$$

$$\Delta QE(\lambda) = QE(\lambda)\sqrt{\left(\frac{\Delta I}{\overline{I}}\right)^2 + \left(\frac{\Delta P}{\overline{P}}\right)^2 + \left(\frac{\Delta \lambda}{\lambda}\right)^2} \tag{3.2}$$

where $I_{\text{ph}}(\lambda)$ and I_{dark} are the measured photocurrent and dark current, $P_{\text{ph}}(\lambda)$ and P_{dark} are the light power and dark power and λ is the wavelength in nm.

The key advantages of this upgraded system are its high responsibility and precision: Unlike the previous design, where the measurement of photocurrent and light power have to be done sequentially with a rotatable periscope, now they can be measured simultaneously. The fixed optical path maintains a consistent light spot position on the sample, enabling direct comparison between successive QE maps.

In addition, the fully enclosed light path minimizes background light, reducing the detected background below 0.01 μW. This significantly reduces the QE uncertainty, particularly in the high-energy range where monochromated light power is low, as demonstrated in Figure 3.8.

3.4. X-ray Photoelectron Spectroscopy

In-situ X-ray photoelectron spectroscopy (XPS) is employed in this research to investigate the stoichiometry and elemental chemical states on the surface of thin-film alkali-antimonide photocathodes. This information is valuable for deeper understanding the growth mechanism, correlating them with photoemissive properties, and finally guiding the optimization of growth processes.

3.4.1. Fundamental Principles

In XPS experiments, samples are irradiated with an X-ray beam, causing the emission of photoelectrons that are subsequently analyzed by an electron spectrometer. For conductive materials, the sample's Fermi level aligns with that of

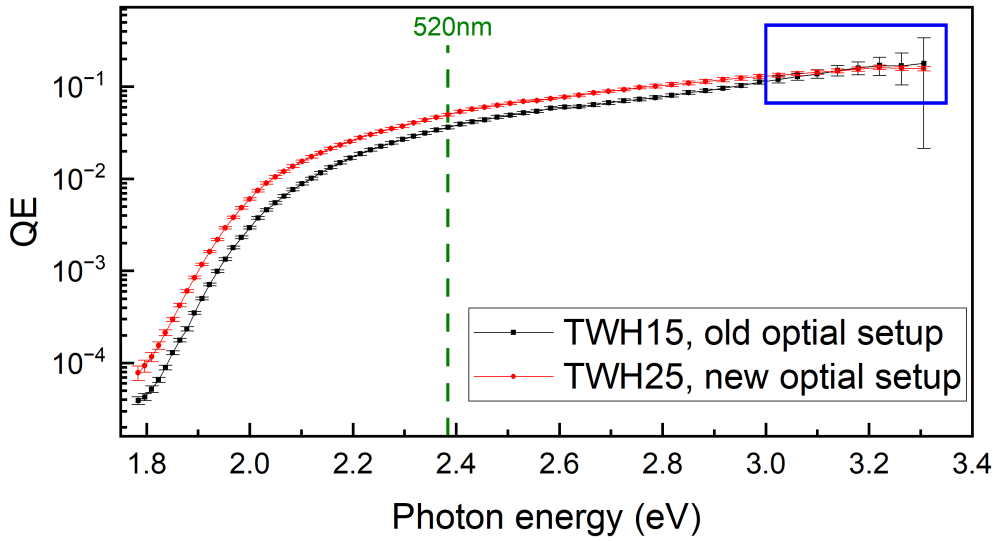


Figure 3.8: *Comparison of spectral response curves measured with the old (TWH15) and new (TWH25) optical setups, showing a significant reduction in QE uncertainty at high photon energy region in the blue box.*

the spectrometer. This alignment allows the principle of energy conservation to be applied:[51]

$$E_{\mathrm{K}} = h\nu - E_{\mathrm{B}}^{\mathrm{F}} - \phi_{\mathrm{sp}} \tag{3.3}$$

where E_{K} is the measured kinetic energy of the emitted electron, $h\nu$ is the incident X-ray photon energy, $E_{\mathrm{B}}^{\mathrm{F}}$ is the binding energy of the core-level electron relative to the Fermi level, and ϕ_{sp} is the work function of the spectrometer, calibrated using a clean silver (Ag) sample.

Figure 3.9a shows a representative XPS survey spectrum taken during the calibration of electron spectrometer with a Ag sample, where intensity is plotted against binding energy. The primary peaks corresponding to Ag core levels (3s, 3p, 3d, 4d) are clearly resolved, excited from the direct photoemission of core-level electrons. Additionally, Ag MNN Auger peaks are present. Unlike photoelectron peaks, Auger peaks appear at a fixed kinetic energy, independent of the excitation source. This can sometimes lead to peak overlap, for example, the Na KL_1L_{23} Auger peak coincides with the O 1s peak when using an Al Kα source. To miti-

gate this, a Mg Kα source is often employed for detection of oxides in Na-K-Sb films.

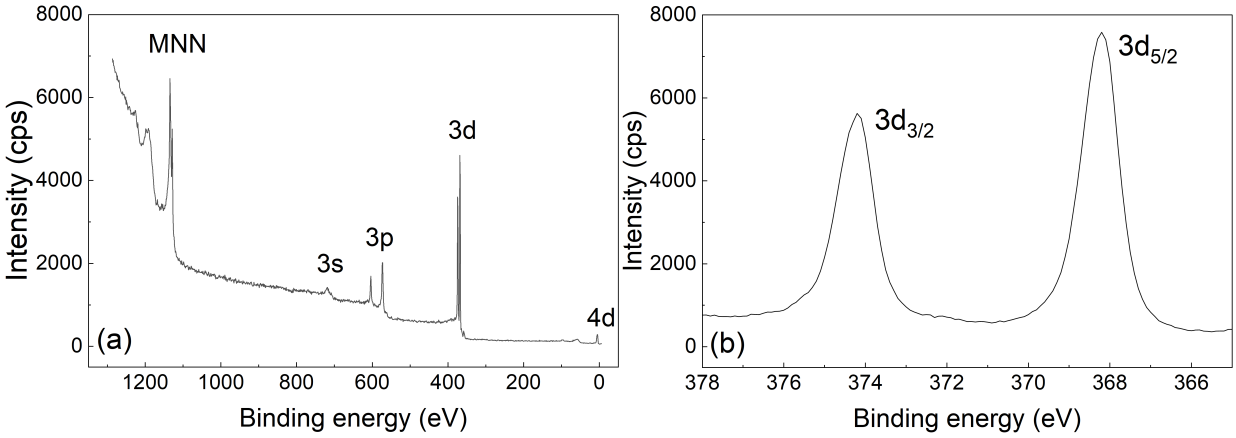


Figure 3.9: *XPS spectra from a cleaned Ag sample, measured with an Al anode for spectrometer energy calibration (medium magnification mode, 7x20 mm entrance slit, 10 eV pass energy): (a) Survey scan and (b) Ag 3d region scan, showing a FWHM of around 1.07 eV for the Ag 3d$_{5/2}$ peak and peak area of 16.8 kcpseV over background.*

Although X-rays penetrate micrometers into the material, the detected signal is highly surface-sensitive, typically originating from the top few nanometers. This is due to the short inelastic mean free path (IMFP) of electrons, which ranges from 5 Å to 30 Å for kinetic energies between 100-1500 eV.[52] The sampling depth is described by Beer-Lambert's Law:

$$I_{\text{int}}(z) = I_{\text{int}}(0)\exp(-z/\lambda\sin\theta) \tag{3.4}$$

where $I_{\text{int}}(z)$ is the intensity from atoms at depth z, $I_{\text{int}}(0)$ is the intensity from surface atoms, θ is the electron take-off angle relative to the surface plane, and λ is the IMFP. The characterization depth of XPS is usually expressed as the depth of $3\lambda\sin\theta$, because approximately 95% of the signal originates from this depth. Varying the X-ray source (Al Kα at 1486.6 eV, Mg Kα at 1253.6 eV) changes the kinetic energy of the photoelectrons and thus the IMFP, enabling depth-dependent analysis. Angle-resolved measurements were not feasible in our setup due to the

unfocused X-ray source, which would lead to an increased sampling area and signal contamination from the inhomogeneous film edges, as shown in Figure 4.9a.

The background signal in XPS spectra increases monotonically with binding energy. This arises from photoelectrons that undergo inelastic scattering while traveling to the surface, losing energy and contributing to the signal on the higher-binding-energy side of primary peaks.

3.4.2. XPS Experimental Setup

As shown in Figure 3.4, the XPS analysis chamber is directly connected to the preparation chamber, a configuration that was preserved during the laboratory relocation. Samples are transferred between chambers under ultra-high vacuum (UHV) conditions (pressure maintained in the $10^{-10}\,\mathrm{mbar}$ range) using the same vertical manipulator.

Within the XPS chamber, the electron spectrometer (SPECS Phoibos 100 CCD) is positioned at a 54° angle relative to the dual-anode X-ray source (SPECS XR-50, Mg/Al) in the horizontal plane. The X-ray source is unfocused and non-monochromatic, producing a broad illumination area. However, the acceptance of the analyzer lens system imposes narrow constraints on the position and emission angle of the detected photoelectrons.

Consequently, alignment of the sample center is essential before each measurement, particularly for triple evaporation samples which exhibit inhomogeneity in the edge (Figure 4.9a). The sample plane is positioned 40 mm from the analyzer to maximize signal acceptance. The center position (X, Y, Z) is calibrated by translating the sample to maximize the peak intensity of the Sb $3d_{5/2}$ transition at 526.3 eV, with the final coordinates determined to be (0, 0, 641), as illustrated in Figure 3.10.

The energy resolution of the instrument was characterized using the Ag $3d_{5/2}$ peak. The measured full-width-at-half-maximum (FWHM, ΔE_{FWHM}) results from

several contributions:

$$\Delta E_{\mathrm{FWHM}} = (\Delta E_{\mathrm{n}}^2 + \Delta E_{\mathrm{p}}^2 + \Delta E_{\mathrm{a}}^2)^{1/2} \tag{3.5}$$

where ΔE_{n} is the natural linewidth of Ag $3d_{5/2}$ peak equals to 0.33 eV,[53] and ΔE_{p}=0.85 eV is the energy width of Al Kα source.[54] With a measured ΔE_{FWHM} of 1.07 eV (from a fit using 60% Lorentzian and 40% Gaussian components), the analyzer resolution ΔEa is calculated to be 0.56 eV at a pass energy of 10 eV, contributing to an additional 0.15 eV FWHM.

Standard XPS operations were performed using either Al Kα radiation at 250 W or Mg Kα at 200 W. The analyzer was operated in medium magnification mode with a 7x20 mm entrance slit and a 10 eV pass energy for region scans, consistent with the spectrometer setup described by Schmeisser.[46]

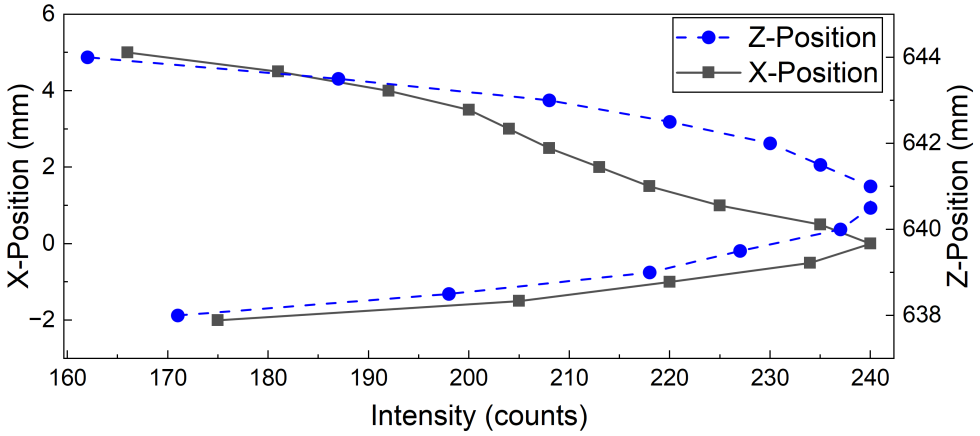


Figure 3.10: *Alignment of the Na-K-Sb film center for XPS measurement by maximizing the intensity of the Sb $3d_{5/2}$ peak at 526.3 eV.*

3.4.3. Chemical Composition Calculation

The surface stoichiometry of the photocathodes was determined from high-resolution region scans of the Na 1s (1065–1087 eV), K 2p (288–310 eV), and Sb 3d (522–550 eV) core levels, acquired with a 10 eV pass energy. After applying a Shirley background subtraction, the atomic concentration ratio of an alkali metal

(A = Na or K) to antimony (B = Sb) is calculated using the standard formula:

$$\frac{c[A]}{c[B]} = \frac{I_{\text{int}}[A]}{I_{\text{int}}[B]} \cdot \frac{\sigma_{\text{cs}}[B] \cdot \lambda_{\text{imfp}}[B] \cdot T_{\text{tran}}[B]}{\sigma_{\text{cs}}[A] \cdot \lambda_{\text{imfp}}[A] \cdot T_{\text{tran}}[A]}, \tag{3.6}$$

where c is the atomic concentration, I_{int} is the peak intensity (background-subtracted peak area), σ_{cs} is the photoionization cross-section,[55] λ_{imfp} is the inelastic mean free path (IMFP),[56,57] and T_{tran} is the energy-dependent transmission function of the electron analyzer.

A critical consideration is the difference in IMFP for the various core levels, as summarized in Table 3.4. The IMFP for Na 1s photoelectrons is significantly lower than for K 2p and Sb 3d, making the measured Na concentration more surface-sensitive. In addition, the characterization depth of XPS (governed by the IMFP of high-energy photoelectrons) is significantly smaller than the attenuation length for the low-energy photoelectrons excited by green light, and will be discussed further in Section 4.5.1.

Table 3.4: *Inelastic mean free path (IMFP) and normalized photoionization cross-sections for relevant core levels excited by Al Kα and Mg Kα radiation.*[55,56,57]

Element	Alka		Mgka	
	IMFP (Å)	Cross Section	IMFP (Å)	Cross Section
Na 1s	15.9	8.52	9.15	7.99
K 2p	35.4	3.97	29.9	4.04
Sb 3d	29.9	27.7	3.97	27.3

3.4.4. Chemical Shifts

The binding energy of a core-level electron is sensitive to its local chemical environment. The resulting binding energy difference relative to the pure element, is called the “chemical shift”.

In general, the formation of cations leads to an increase in binding energy (positive shift), while the formation of anions results in a decrease (negative shift).

This is primarily an initial-state effect, governed by changes in the electrostatic potential. A modified point charge model describes the chemical shift (ΔE_{i}) as:[51]

$$\Delta E_{\mathrm{i}} = k\Delta q_{\mathrm{i}} + l\Delta V_{\mathrm{M}} + \Delta E_{\mathrm{R}} \tag{3.7}$$

where $k\Delta q_{\mathrm{i}}$ represents the change in potential of atom i due to the gain (negative) or loss (positive) of electrons, $l\Delta V_{\mathrm{M}}$ is the change in the Madelung potential from the surrounding crystal lattice, and ΔE_{R} is the final-state relaxation energy correction.

For many elements, the charge transfer term ($k\Delta q_{\mathrm{i}}$) dominates. This is clearly observed in antimony, where the Sb 3d peak exhibits a linear shift with the charge transfer.[58] Consequently, the Sb chemical shift serves as an effective indicator of whether antimony has fully reacted with alkali metals to form A_3Sb (A = Na or K) compounds, as demonstrated in Section 6.2 for K-Sb series compounds.

However, for heavy alkali metals (K, Rb, Cs), the final-state relaxation term (ΔE_{R}) is significant. Their large atomic radius leads to delocalized valence electrons and extremely efficient relaxation in the metallic state. This results in a greater relaxation energy in the pure metal than in its compounds, often causing a negative binding energy shift in their compound,[58] as well as in alkali-antimonides.[31,59,60]

3.4.5. Interference and Solutions

When analyzing semiconductor materials like Na-K-Sb compounds, two phenomena can interfere with the measured binding energies: charging effects and Fermi level pinning at the surface.

Charging effect: Although the conductivity of small band gap semiconductors (for example the alkali-antimonides) are sufficient to maintain good electrical contact with spectrometer, the possibility of surface charging during XPS analysis must be ruled out: multiple region scans of the Sb 3d peak were acquired at the beginning and end of each measurement sequence. As shown in Figure 3.11, the

relative peak shift of the Sb 3d level was less than the measurement step size of 0.1 eV, confirming that no significant charge accumulation occurred.

A separate problem observed was a decrease in peak intensity (up to 5%) between the first and last scan. This is attributed to the degassing from the anode, whose bypass is directed facing the sample surface, causing a pressure increase to several $10^{-9}\,\mathrm{mbar}$. This degassing also reduced the QE of the photocathode by approximately 50%. While the exact mechanism remains unclear (as no RGA data was collected and no obvious oxygen peak was detected), most of the lost QE could be recovered by depositing a small amount of K at 110°C.

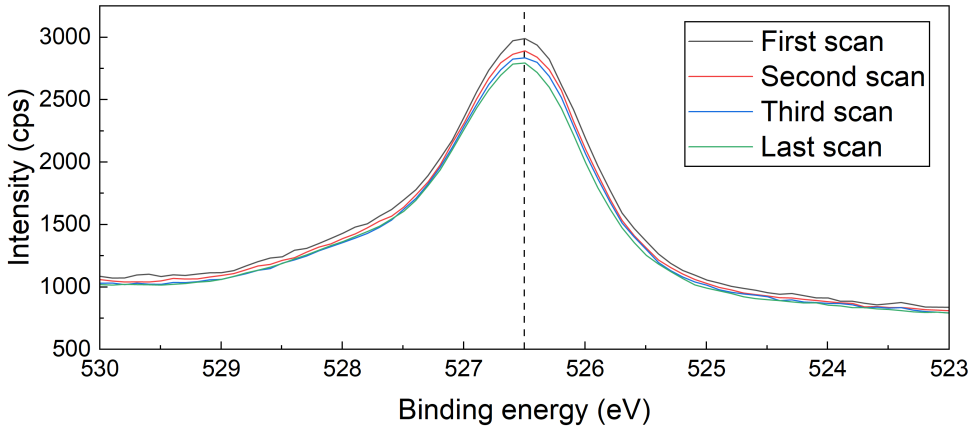


Figure 3.11: *Region scans of Sb $3d_{5/2}$ were acquired at the beginning (First scan, Second scan and Third scan) and at the end (50 minutes later, Last scan) of the XPS measurement sequence of TP01. The peak positions are highly consistent, indicating no significant charge accumulation during XPS analysis.*

Surface Band Bending: The Na-K-Sb system contains both n-type (e.g., hexagonal K_3Sb, Na_3Sb, NaK_2Sb) and p-type (e.g., cubic K_3Sb, Na_2KSb) semiconductors, which exhibit different band bending behaviors at interfaces. Given that the XPS characterization depth (5–11 nm) is much less than the film thickness ($\sim$50 nm), the measured binding energies mainly reflect the band bending at the surface.

At the surface, Fermi level pinning induces surface band bending (Figure 3.12). For p-type semiconductors, this typically shifts core-level peaks to lower bind-

ing energies, while n-type doping causes a shift to higher binding energies.[61,62] The band bending in p-type alkali-antimonides like Cs_3Sb has been estimated at $\sim$0.3 eV with a space-charge region extending 10 nm.[63] The exact magnitude depends on carrier concentration and surface states, requiring experimental confirmation for each material, as discussed in Section 6.4.3.

The Auger Parameter: To minimize the energy reference problems including surface band bending, the modified Auger parameter α' can be used. It is defined as the sum of the Auger electron kinetic energy ($E_{\mathrm{K}}(C_1C_2C_3)$) from C_1, C_2 and C_3 core level and the XPS photoelectron binding energy ($E_{\mathrm{B}}(C)$) from core level C:

$$\alpha' = E_{\mathrm{K}}(C_1C_2C_3) + E_{\mathrm{B}}(C) \tag{3.8}$$

Since both energies are similarly affected by band bending or charging, their influences largely cancel in the sum. While, the actual situation is much more complicated than what is discussed, but the use of α' can normally significantly reduce the influence of surface band bending.

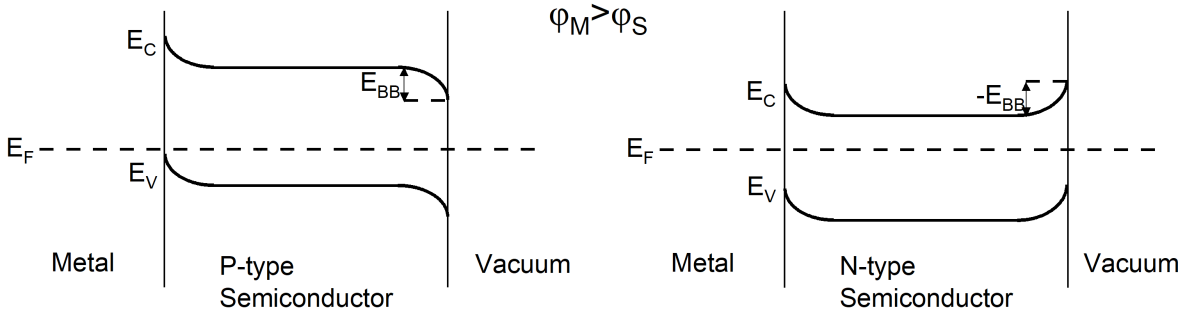


Figure 3.12: *Schematic band bending model of thick p-type (left) and n-type (right) semiconductor films on metal substrate with a higher work function.*[61,62]

4. Na-K-Sb Growth Studies

This chapter details the development of growth process for Na-K-Sb photocathodes, with a primary focus on a novel triple evaporation method. This method enables, for the first time, the reproducible growth of Na-K-Sb films with stoichiometries approaching the ideal Na_2KSb composition, achieving QE of approximately 5% at 520 nm. Utilizing this controlled growth method, key photoemissive properties of the Na-K-Sb photocathodes—including surface QE homogeneity, storage lifetime, and spectral response—are systematically investigated. This work also establishes clear correlations between the key growth parameters, the final stoichiometry, and the resulting photoemissive properties, thereby providing a framework for the rapid optimization of Na-K-Sb photocathodes.

4.1. Dispenser Chamber Based Experiment

This section provides an overview of preliminary studies on the growth process of Na-K-Sb photocathodes in the dispenser chamber, covering both sequential and alkali co-deposition methods. Throughout this study, substrate temperature is represented by stage temperatures: a calibration curve between the two is provided in Figure 3.6a (old chamber).

4.1.1. Modified Sequential Deposition

The modified sequential deposition protocol follows Cultrera's recipe,[9] but employs a lower substrate temperature due to reduced alkali metal flow rates caused by the large dispenser-to-sample distance in the chamber (see Section 3.2.1).

The growth process begins with the deposition of 40 nm Sb at 90 °C (rate: 0.2 Å/s) through a 5 mm diameter aperture. Subsequently, K dispensers are activated (6 A per dispenser), while the photocurrent is monitored under 515 nm illumination (Figure 4.1). At this temperature, K reacts with Sb to form K_3Sb, typically achieving a QE of $\sim$0.1% upon a duration of $\sim$3 hours. XPS study of the K-Sb phases

is detailed in Section 6.2.

Following K_3Sb formation, the substrate temperature is increased to approximately 150 °C for Na deposition. The photocurrent drops to zero shortly, as the K_3Sb phase become unstable at elevated temperatures. Previous studies have shown that K_3Sb dissociates at temperatures above 120 °C.[38]

At 130 °C, Na dispensers are activated (5.75–6 A per dispenser), while K dispensers remain on to compensate for K loss at high temperatures. The photocurrent initially rises, peaks, and then declines due to Na oversaturation—a consequence of the low Na/K equilibrium vapor pressure ratio in Na-K-Sb phases.[9,40] For instance, in the growth of sample WH13 (Figure 4.1), the Na dispensers were turned off 5 minutes after the photocurrent plateaued at 150 °C, resulting in a slightly Na-oversaturated $Na_{2.2}K_{0.9}Sb$ film. Notably, the photocurrent decreases as the substrate cools (Figure 4.1, after 250 minutes).

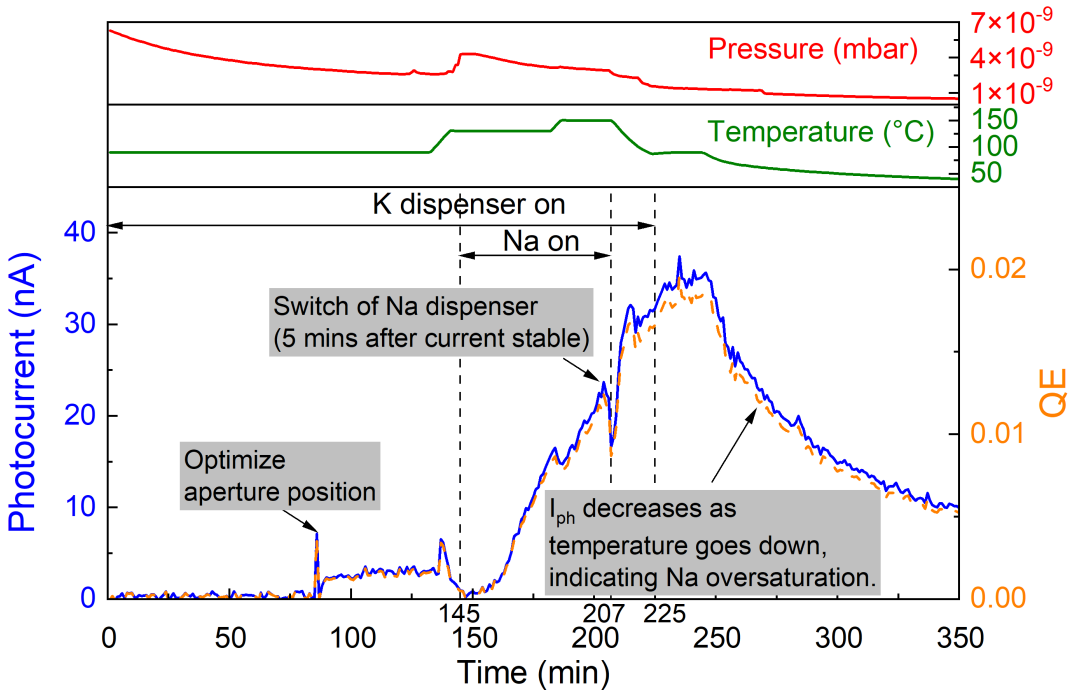


Figure 4.1: *Sequential growth process of Na-K-Sb photocathode film (WH13).*

Although Na oversaturation can theoretically be compensated by additional Sb

and K deposition,[9] the dispenser chamber's design—where Sb and alkali sources located in two height layers—makes this impractical. Thus, Na dispensers must be turned off immediately after photocurrent plateauing to minimize this oversaturation.

4.1.2. Alkali Co-Deposition

The alkali co-deposition method was developed to enhance the success rate (>50%) and simplify the growth process, offering a more practical approach for routine fabrication by providing a larger time window for each step.

As shown in Figure 4.2, this method also begins with the deposition of a 40 nm Sb layer, followed by direct heating of the substrate to 150 °C. At this temperature, both K and Na dispensers are activated (K: 5.75–6 A per dispenser; Na: 5.25–5.5 A per dispenser), with the K flow rate maintained significantly higher than that of Na. Alkali co-deposition proceeds for approximately 3 hours, during which the photocurrent rises. To accelerate the formation of Na_2KSb phases, the substrate temperature can optionally be increased. Typically, in the final stage, the temperature is raised to 180 °C for 20 minutes before the Na dispensers are turned off. The sample is then cooled with the K dispensers remaining active until 90 °C to minimize decomposition of the Na-K-Sb phases.

This recipe mitigates the Na oversaturation, a common issue in earlier experiments. However, the resulting stoichiometric Na/K ratio (<2.0) often deviates from the optimal value reported by Sommer.[7] Consequently, the measured QE (515 nm) for co-deposited films—e.g., WH17 ($Na_{1.5}K_{1.8}Sb$) at 2.3%—remains lower than literature values over 5% in 515 nm.[24]

4.1.3. Discussion of the Two Growth Procedures

The co-deposition method enhances both the success rate and practicality of Na-K-Sb photocathode growth by exploiting the low equilibrium vapor pressure ratio of Na to K required for Na_2KSb phase formation. Compared to the sequential method, co-deposition employs a significantly lower Na flow rate and longer

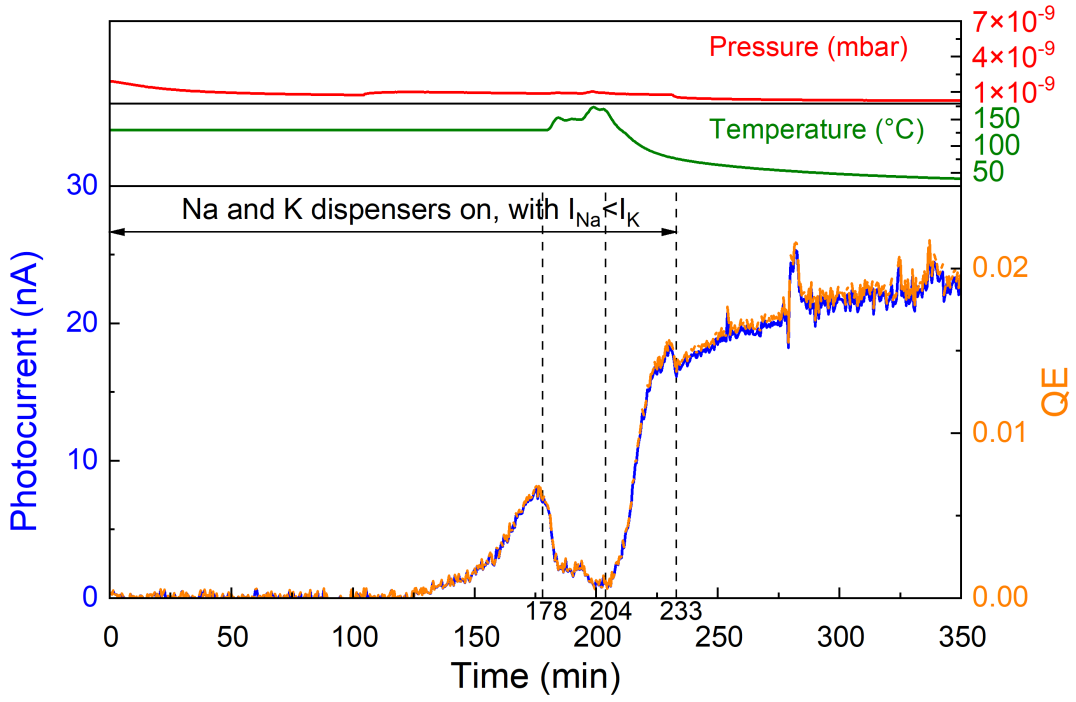


Figure 4.2: *Alkali metal co-deposition growth process of Na-K-Sb photocathode film (WH17).*

deposition time, reducing the need for precise control.

In the sequential method, achieving the phase transition from K_3Sb to Na_2KSb necessitates a higher Na deposition rate, resulting in an extremely short response window. For instance, delaying the termination of Na deposition by just 5 minutes after photocurrent plateauing leads to oversaturation (Figure 4.1). In contrast, the co-deposition method provides a larger time window for Na deposition. As long as the final K/Sb stoichiometric ratio remains between 1.0 and 2.0, the QE consistently exceeds 1% (Section 4.1.5).

4.1.4. Reaction Mechanism in Alkli Co-Deposition

Combining the possible phases in Na-K-Sb system[28] and multiple experimental data, the co-deposition growth process is concluded into two key steps:

(1) Addition Reaction:

K and Na simultaneously react with Sb, while the higher K flow rate enhances the formation of K dominated phase, yielding a Na-K-Sb compound with K/Na $>$ 2. Since no Na_2KSb phase is generated, no photocurrent is observed in this stage (Figure 4.2, 0–125 min), the reaction is described by:

$$(2+m)\mathrm{K}(g) + (1-m)\mathrm{Na}(g) + \mathrm{Sb}(s) \rightarrow (\mathrm{Na}_{1-m}, \mathrm{K}_m)\mathrm{K}_2\mathrm{Sb}(s), \quad 0 < m < 1. \tag{4.1}$$

(2) Substitution Reaction:

At 150–180 °C, Na gradually substitutes K resulting in the formation of Na_2KSb and increasing photocurrent:

$$(\mathrm{Na}_{1-m}, \mathrm{K}_m)\mathrm{K}_2\mathrm{Sb}(s) + m\mathrm{Na}(g) \rightarrow \mathrm{NaK}_2\mathrm{Sb}(s) + m\mathrm{K}(g), \quad 0 < m < 1. \tag{4.2}$$

$$\mathrm{NaK}_2\mathrm{Sb}(s) + \mathrm{Na}(g) \rightarrow \mathrm{Na}_2\mathrm{KSb}(s) + \mathrm{K}(g) \tag{4.3}$$

Prolonged Na deposition leads to Na_3Sb formation and photocurrent decay:

$$\mathrm{Na}_2\mathrm{KSb}(s) + \mathrm{Na}(g) \rightarrow \mathrm{Na}_3\mathrm{Sb}(s) + \mathrm{K}(g) \tag{4.4}$$

Samples WH14 and WH16 (Table 4.1), grown under identical co-deposition conditions (K flow $\gg$ Na), demonstrate this mechanism: WH16 extended 6-hour reaction (vs. WH14's 3 hours) reduced the K/Sb ratio from 1.6 to 0.5 due to continued Na substitution. These results align with literature reports of a Na/K equilibrium vapor pressure ratio $<$ 1:50.[38,40]

Furthermore, the high stability of Na-rich phase like Na_3Sb was confirmed by depositing K for 2 hours on the Na-oversaturated sample WH06 (Table 4.1). The negligible change in K/Sb ratio confirms that Na-Sb phases are more stable[38] and cannot be reversed by subsequent K deposition alone.

These experiments further proved the two critical aspects governing Na-K-Sb

Table 4.1: *Stoichiometry and QE at 515 nm of 15 Na-K-Sb photocathodes grown in dispenser chamber*

Sample	Method	QE	Stoichiometry (Na:K:Sb)	Na/K	(Na+K)/Sb
WH04	co-dep	0%	1.3:0.6:1.0	2.3	1.9
WH05	co-dep	0%	2.2:0.8:1.0	2.7	3.0
WH06	co-dep	0.5%	2.3:0.4:1.0	5.9	2.7
WH06+K	-	0.4%	2.6:0.6:1.0	4.8	3.2
WH07	seq	0%	1.8:0.5:1.0	3.7	2.3
WH08	seq	0.2%	0.9:2.1:1.0	0.4	3.1
WH09	seq	2.6%	2.1:1.2:1.0	1.7	3.4
WH10	seq	0.5%	0.7:1.3:1.0	0.6	2.0
WH11	seq	0.5%	2.4:0.7:1.0	3.3	3.1
WH12	seq	0.3%	2.6:0.4:1.0	6.7	2.9
WH13	seq	1.3%	2.2:0.9:1.0	2.5	3.1
WH14	co-dep	2.3%	1.7:1.6:1.0	1.1	3.3
WH15	seq	0%	0.9:2.3:1.0	0.4	3.2
WH16	co-dep	0%	2.4:0.5:1.0	4.5	2.9
WH17	co-dep	1.9%	1.5:1.8:1.0	0.8	3.4

photocathode growth: The extremely low equilibrium vapor pressure of Na_2KSb phase and high stability of Na-rich phase. These two characteristics also highlight the differences between Na-K-Sb and Cs-K-Sb film growth. In Cs-K-Sb system, the substitution reaction of K by Cs is reversible, and can be adjust in equilibrium conditions: During alkali co-deposition of Cs-K-Sb, the Cs-to-K flow rate can be maintained at approximately 1:1[64] and the final Cs/K stoichiometric ratio in the film can be adjusted and depends on the Cs-to-K flow rate.[46] However, the substitution reaction of K by Na is irreversible, and the extent of reaction has to depend on the control of reaction speed (temperature/ alkali flow rate) and reaction time.

4.1.5. Stoichiometry and Quantum Efficiency

To identify the optimal stoichiometric range for high QE, I analyzed the surface composition of 15 Na-K-Sb films using XPS. Measurements were performed at

room temperature within 12–24 hours post-growth. The K/Sb ratio is more reliable than Na/Sb due to the similar inelastic mean free paths (IMFP) of Sb 3d and K 2p, whereas the IMFP of Na 1s is only half that of Sb 3d in Al Kα.

As shown in Table 4.1, samples with QE $>$ 1.0% consistently satisfy two criteria: sufficient alkali content and optimal K/Sb ratio. All high-QE films (WH09, WH13, WH14, WH17) meet the stochiometric conditions of alkali to Sb ratio $\approx$ 3, and the K to Sb ratio between 0.9 to 1.8.

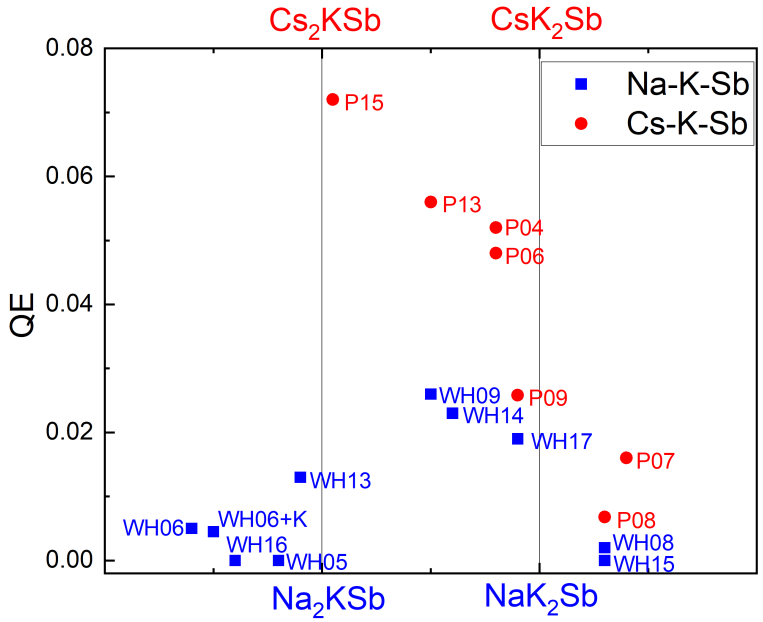


Figure 4.3: *Chemical Composition (given by K/Sb ratio) and QE of Na-K-Sb and Cs-K-Sb*[39] *photocathode films, QE for Na-K-Sb measured at 515 nm and for Cs-K-Sb at 532 nm.*

In order to explore the impact of stoichiometry as a single factor on the QE, excluding the alkali-deficient samples (WH04, WH07 and WH10), the QE values of 12 Na-K-Sb and 9 Cs-K-Sb films and their stoichiometry in K to Sb ratio are shown in Figure 4.3. Cs-K-Sb system exhibits a broad stoichiometric window (Cs_3Sb to CsK_2Sb) with QE $>$ 2%, and the maximum QE is over 7%. In contrast, the acceptable window in Na-K-Sb system is narrower, with peak QE observed for WH09 ($Na_{2.1}K_{1.2}Sb$) at 2.6%. However, the ideal Na_2KSb phase (K/Sb = 2.0), predicted to achieve at least 5% QE at 515 nm,[24] is absent in our database. If

such a high QE sample exists, it should be present in the gap between WH13 ($Na_{2.2}K_{0.9}Sb$) and WH09 ($Na_{2.1}K_{1.2}Sb$), which will be discussed in Section 4.5.1. This very narrow gap underscores the need for finer control of growth parameters, especially the alkali metal flow rate, for high-QE Na_2KSb phase.

4.1.6. Storage Lifetime

The storage lifetime for both Na-K-Sb and Cs-K-Sb photocathode films is presented in Figure 4.4. All QE measurements were performed in preparation chamber under ultra-high vacuum conditions (base pressure in low 10^{-10} mbar). Here the storage lifetime (τ) is defined as the duration (in days) during which the QE remains above 1.0% - the optimal operational requirement for photocathodes in SEALab.

Na-K-Sb films consistently demonstrate superior storage lifetime compared to Cs-K-Sb. Notably, samples WH14 and WH09 show exceptional stability, with QE degradation of $<$20% after two weeks. In contrast, WH17 (with suboptimal K/Sb stoichiometry) exhibits significantly reduced stability (τ = 16 days), indicating the correlation between chemical composition and storage lifetime.

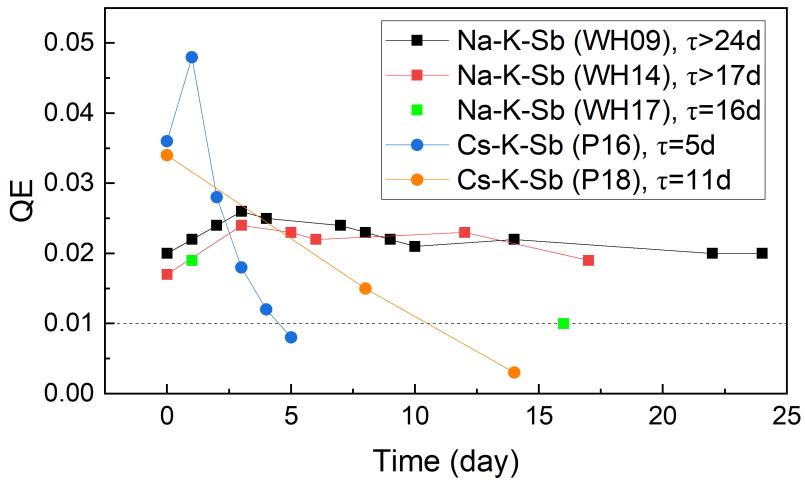


Figure 4.4: *Storage lifetime of Na-K-Sb and Cs-K-Sb[39] photocathode films, QE for Na-K-Sb measured at 515 nm and for Cs-K-Sb at 532 nm.*

Additionally, samples WH09 and WH13 display a QE increase during the first 72 hours, potentially attributable to: evaporation of excess alkali metals or gradual formation of the Na_2KSb phase through diffusion. A similar QE increase process has been reported in Cs-K-Sb systems, though it occurs over a shorter timescale.[65]

4.1.7. Conclusion

The preliminary experiments successfully demonstrate the growth of Na-K-Sb photocathode films on Mo plugs, achieving a QE $>2\%$ at 515 nm with week-scale stability. However, the maximum QE achieved (2.6%) remains significantly lower than literature values (7% at 532 nm),[9] highlighting unresolved challenges in stoichiometric control.

Despite depositing 15 films with different compositions, none reached the ideal Na_2KSb stoichiometry. Low equilibrium vapor pressure of Na often leads to unavoidable Na oversaturation samples and resulting in low QE. While alkali co-deposition improved success rates, the narrow stoichiometric window for high QE (Na/K ≈ 2.0) demands finer control.

Additionally, unpredictable alkali flow rates from dispensers led to inconsistent results—identical parameters yielded varying stoichiometries and QE values, producing irreproducibility and complicating systematic optimization.

4.2. Triple Evaporation Chamber Based Experiments

To address the irreproducibility and stoichiometric control challenges outlined earlier, critical upgrades have been implemented in the triple evaporation chamber, including stabilized alkali flow rates via effusion cells loaded with AlkaMax pills and the triple evaporation setup for simultaneous Na-K-Sb deposition.

This section provides an overview of the studies on the triple evaporation of Na-K-Sb photocathodes in the triple evaporation chamber. Substrate-stage temperature correlations are calibrated (Figure 3.6, new chamber). However, during Sb deposition, radiated heating from the Sb thermal crack cell (700 °C, 148 mm distance) elevates the actual substrate temperature beyond calibrated values.

For triple evaporation, preliminary experiment (TWH13) revealed a lower threshold at around 110 °C for the growth of high-QE Na-K-Sb photocathode.[47] No photocurrent was observed at 100 °C, while a 10 °C increase activates the Na_2KSb phase formation with the increasing of photocurrent. Therefore, 110 °C was adopted to conserve alkali sources in the following studies, while theoretically the combination of higher substrate temperatures and larger alkali flow rates is also feasible.

Optimal deposition rates were established at 0.01 Å/s for Sb, 0.04 Å/s for Na (requiring precise control as it directly governed QE development) and 0.14 Å/s for K (tolerable down to 0.08 Å/s or lower). Before each growth, the deposition rates of the three element are measured with the QCM and adjusted to the optimal values (Sec. Section 3.2.2). The system demonstrated stable operation without flux adjustment during growth for the first 10 cycles after AlkaMax pill refills, after which Na flux decay necessitated manual temperature compensation—for example, during TWH22 growth (15th film growth), the Na cell required a 0.3 °C increase every 10 minutes to maintain the increase of photocurrent. Nevertheless, this refined growth system represents a significant advancement toward reproducible high-QE Na_2KSb photocathodes with precise stoichiometry control.

4.2.1. Triple Evaporation Method

The Na_2KSb triple evaporation growth procedure, illustrated in Figure 4.5, includes three phases: simultaneous Na-K-Sb co-deposition at 110 °C (Phase I), controlled K and Sb deposition for stoichiometric tuning (Phase II) and low-rate K deposition during cooling to mitigate alkali loss (Phase III).

In Phase I, during simultaneous evaporation of Na, K, and Sb (substrate temperature: 110 °C), QE is monitored via 520 nm laser illumination, and can typically be observed within 10 minutes after opening source shutter. The increase of QE follows the logistic growth, and peaking at 4.5% $\pm$0.5% in 100 to 150 minutes (6-9 nm Sb)—approximately twice as fast as Cs-K-Sb systems, suggesting

differences in low-energy-photoelectron escape depths (2.4 eV) between the two systems.[42] The subsequent QE decline (5–10%) likely causes by Na flux decay. At the end of Phase I, Na and K deposition rate can be adjusted to maximize QE.

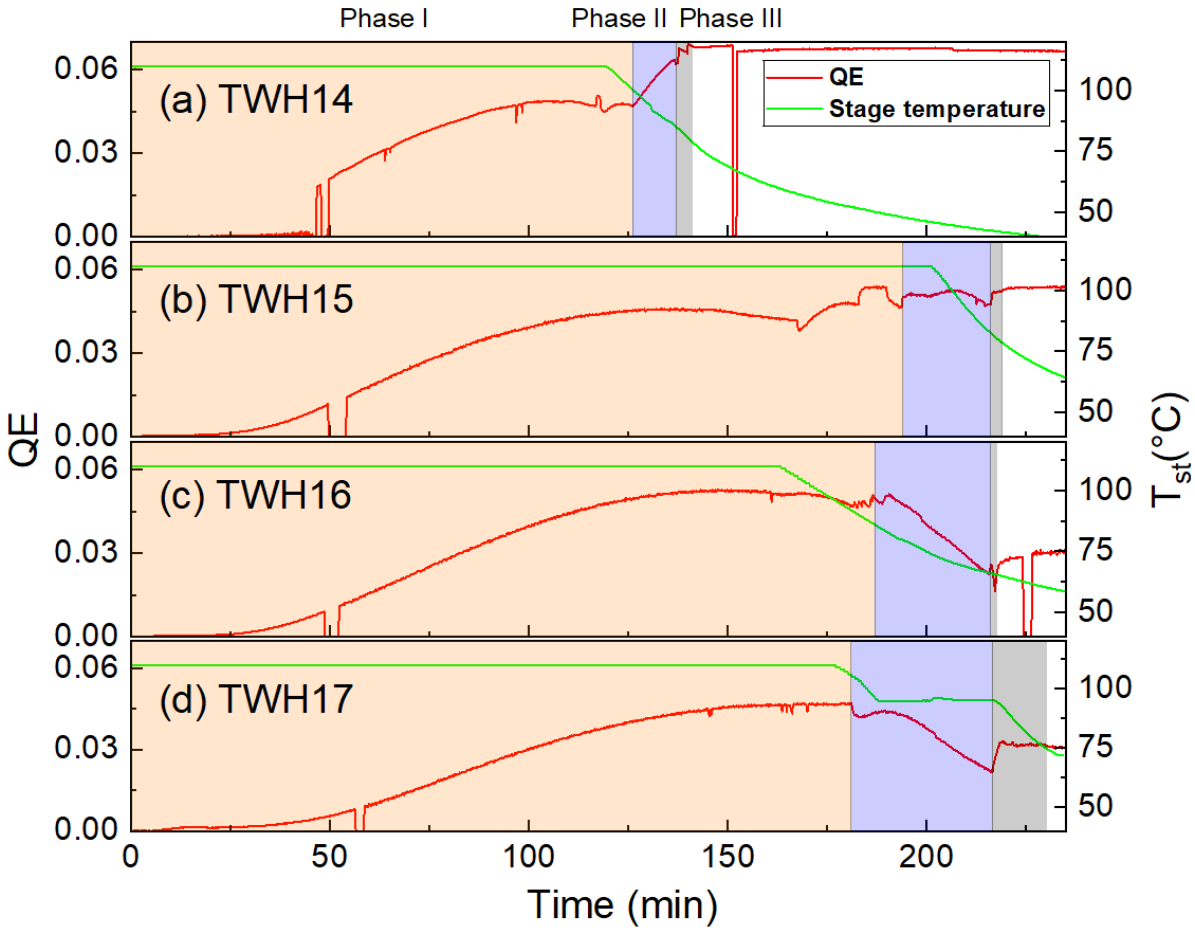


Figure 4.5: *QE (at 520 nm) and substrate temperature in triple evaporation growth (Tri-1) of four Na_2KSb photocathode films. (a) TWH14 (4th growth), (b) TWH15 (5th growth), (c) TWH16 (8th growth) and (d) TWH17 (9th growth).*

In Phase II, the shutter of the Na is closed, while Sb and K are continue to evaporate on the substrate at a desired temperature. This phase is required to obtain the ideal stoichiometry and improved the lifetime of the photocathode. This phase is still in developing process, here we demonstrate 2 recipes (Tri-1 and Tri-2): In Tri-1, lower substrate temperature (around 90 °C) is adopt to induce surface n-type

NaK_2Sb phase formation, aiming at creating downward band bending to reduce threshold energy.[66] In Tri-2, substrate temperature is kept at 110 °C, enhancing the Na diffusion and the in-depth homogeneity of Na_2KSb films, as detailed in Section 5.2.1.

Focusing on Tri-1 (employed for TWH14–TWH17), Phase II duration varied from 10 to 35 minutes to refine stoichiometry. For TWH15–TWH17, total Sb deposition (Phases I+II) maintained 220 minutes (rate: 0.01 Å/s ±5%), yielding 13 nm Sb, assuming a sticking coefficient of 1 as measured by Liang .[48] Accounting for the 3.8 times lattice space expansion from Sb to Na_2KSb (Section 2.4.1.2), final film thickness reached around 50 nm.

In phase III, the Sb shutter is closed and the heater of the sample stage is turned off to cool down the photocathode to room temperature at 5 °C/min. K deposition continues at reduced rates (10 °C lower than Phase I) until QE saturation or substrate temperature below 75 °C. This process mitigates alkali deficiency, preserving QE and storage lifetime.[47]

4.2.2. Stoichiometry and Photoemissive Properties

All photocathodes were monitored for four days post-growth to determine their 1/e storage lifetime, followed by spectral response measurements, QE mapping and XPS analysis. This section presents these results and explores the correlation between stoichiometry and photoemissive performance.

4.2.2.1. Stoichiometry of the Photocathodes

XPS measurements were conducted after photoelectric characterization, as the QE was observed to degrade after XPS analysis—likely due to the pressure increases from degassing of the X-ray gun or radiation damage.

The core-level peak shapes and positions for Na, Sb, and K demonstrated high consistency across all samples (Figure 4.6), highlighting the reproducibility of the triple evaporation method. The Na 1s peak appeared at 1071.5 eV in all samples, with no detectable oxide formation of second peak as shown in Figure 4.6a.

Figure 4.6b shows the region scans of Sb 3d with annotations of Sb^0, Sb^{3-} peaks locating in 528.2 eV and 526.5 eV.[60,67] The Sb $3d_{5/2}$ and Sb $3d_{3/2}$ main peak lie in 526.5 eV and 535.9 eV, respectively, comprising approximately $95\,\%$ intensity. A minor peak is observed at higher binding energy (around 528.0 eV) corresponding to metallic Sb, likely due to the shadowing effects (Figure 4.9a) rather than alkali deficiency.

The peak at 532.6 eV between the Sb 3d doublet peaks corresponds to the Na KL_1L_{23} auger peak, which overlaps with the O 1s peak. The samples did not undergo severe oxidation since no second peaks of Na or K oxides were found in their spectra, though the peak intensity of the O 1s peak is not measured directly.

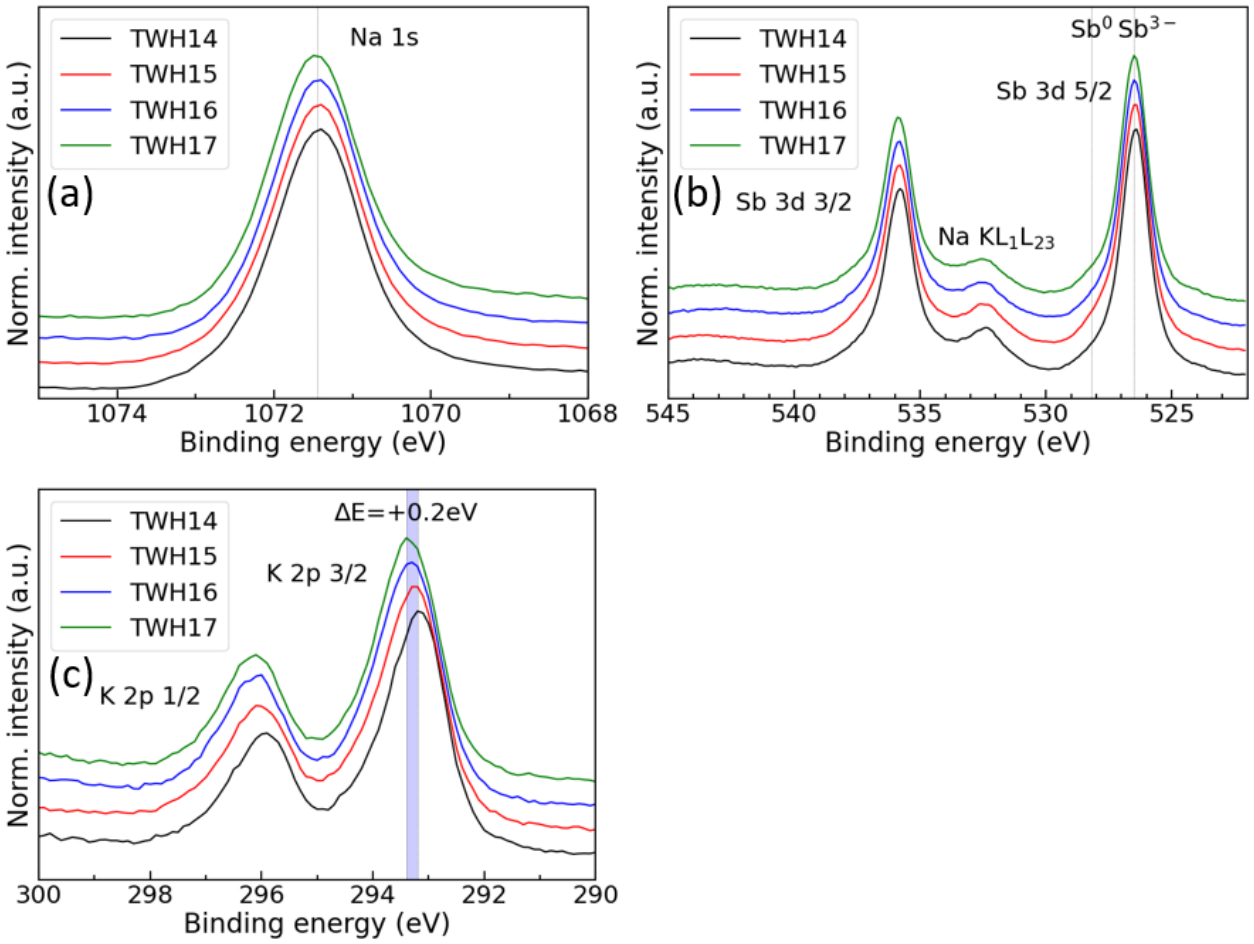


Figure 4.6: *Al Kα XPS spectra of four Na_2KSb photocathodes synthesis by triple evaporation method (Tri-1). (a), (b) and (c) are the region scans of Na 1s, Sb 3d and K 2p, respectively.*

The K $2p_{3/2}$ binding energy increased progressively from TWH14 (293.2 eV) to TWH17 (293.4 eV). This shift suggests extended Phase II duration in TWH16 and TWH17 potentially influencing their peak positions by enhanced surface NaK_2Sb formation. Further investigation of this trend is presented in Section 6.4.3.

Additionally, stoichiometry calculated from XPS (Al kα) (Table 4.2) revealed high Na mobility during growth. For sample in TWH17, despite depositing an additional 2.2 nm Sb (corresponding to 12.7 nm of hexagonal K_3Sb) during Phase II - a thickness exceeding the 3 times IMFP (4.8 nm) of Na 1s photoelectrons - a considerable Na concentration is still detected on the surface. This high mobility of Na helps to explain why the K/Sb ratio plateaued at 1.2 for both TWH16 and TWH17 despite extended Phase II deposition times. These observations demonstrate that Na exhibits high mobility in Na-K-Sb phases in the presence of metallic Sb.

Table 4.2: *Summary of growth parameters, stoichiometry and photoemissive properties of the four Na_2KSb photocathodes*

Sample	Phase II/Total Thickness of Sb	Stoichiometry	Peak QE	1/e Lifetime
TWH14	0.7/8nm	$Na_{2.4}K_{1.0}Sb_{1.0}$	6.8 %	63h
TWH15	1.3/13nm	$Na_{2.2}K_{1.2}Sb_{1.0}$	5.6 %	220h
TWH16	1.8/13nm	$Na_{1.9}K_{1.2}Sb_{1.0}$	3.1 %	>500h
TWH17	2.2/13nm	$Na_{1.9}K_{1.2}Sb_{1.0}$	3.4 %	>500h

4.2.2.2. Storage Lifetime and Spectral Response

The photoelectric properties were characterized at the center of photocathode, the same as the growth monitoring position. The peak QE (highest QE achieved post-growth) and storage lifetime (τ) were measured once the sample stage cooled below 50 °C. Lifetime values were calculated by fitting the QE decay to function $QE = A \times \exp(-t/\tau)$, where A represents the initial QE as shown in Figure 4.7a and summarized in Table 4.2.

TWH14 achieved the highest peak QE (6.8%) but the shortest lifetime (63 h),

correlating to its Na-rich surface (Na/Sb = 2.4, (Na+K)/Sb = 3.4), deviating from the ideal Na_2KSb stoichiometry. This suggests Na surface enrichment may accelerate the QE degradation (further studied in Section 4.5.2). TWH15-TWH17 demonstrated improved stability (τ = 220-500h+) but at the cost of reduced QE (5.6% to 3.4%). This performance decline correlates with suboptimal Na/K ratios (<2.0) and increased NaK_2Sb surface content during extended Phase II deposition at lower temperatures. These results reveal the limitation of the Tri-1 recipe: the competing requirements for high QE (needing Na_2KSb stoichiometry) and long lifetime (avoiding Na-rich surfaces) cannot be simultaneously optimized. The formation of NaK_2Sb on the surface was hypothesized to lower the threshold energy through band bending, however, this phase instead significantly degraded the QE because of its low intrinsic QE (Section 6.4). To resolve this, we developed the Tri-2 recipe that enhances the formation of more homogeneous Na_2KSb layers with higher substrate temperature at Phase II, achieving better compatibility between performance and stability as to be discussed in Section 5.2.1.

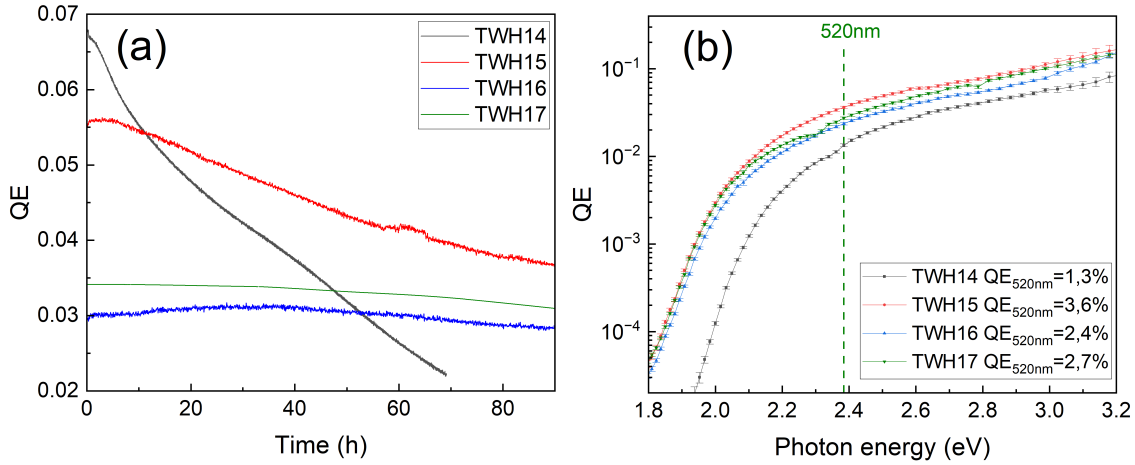


Figure 4.7: *Storage lifetime and spectral response of the four Na_2KSb photocathodes: (a) storage lifetime of Na_2KSb photocathodes, (b) spectral response curve taken four days after growth.*

Following storage lifetime characterization, spectral response curves were acquired for all four samples four days post-growth (Figure 4.7b). The curve for

TWH14 is significantly suppressed across the measured spectrum, consistent with its shorter storage lifetime. In contrast, the spectra for TWH15, TWH16, and TWH17, while similar, exhibit distinct fine structures: the QE of TWH15 rises more rapidly between 2.1 and 2.5 eV. These differences in shape suggest variations in the surface structure, which will be explored in Section 4.6.

4.2.2.3. Surface QE Homogenetiy

To investigate the QE distribution across the film, QE maps were measured 4 days after the growth. Measurements were performed at 520 nm wavelength using a 2 mm diameter light spot with 1 mm step resolution.

As shown in Figure 4.8, TWH15 (Na/K $\approx$ 2.0) exhibited the most homogeneous QE distribution, consistent with its near-ideal stoichiometry. Na-oversaturated TWH14 showed a QE gradient opposite to that of Na-deficient TWH16 and TWH17, indicating a correlation between QE gradient and stoichiometry variation, which will be discussed in next section.

4.3. Surface Homogeneity of Na-K-Sb Photocathode Films

This section presents a systematic investigation of surface homogeneity in Na-K-Sb photocathodes through combined experimental and modeling approaches, aiming at reducing the inhomogeneity and maximizing the QE in the center of the film, which is critical for photoinjector applications.

In Photoninjecter, cathode position is fixed and the photocathode laser is focus on the center of the cathode to make sure the electron beam aligning with the center line of cavity. However, QE mapping reveals significant QE variations across the 4 mm radius films (Figure 4.8), with the edge of the film marked by the white contour line with QE= 1%. The peak QE does not always coincide with the geometric center, especially for TWH14 and TWH16.

Given the sensitivity of QE to stoichiometry shown in Figure 4.3 as well as indicated by previous researches,[7,22] it is reasonable to assume the QE inhomogeneity originates from the variations in Na/K stoichiometric ratio, though direct

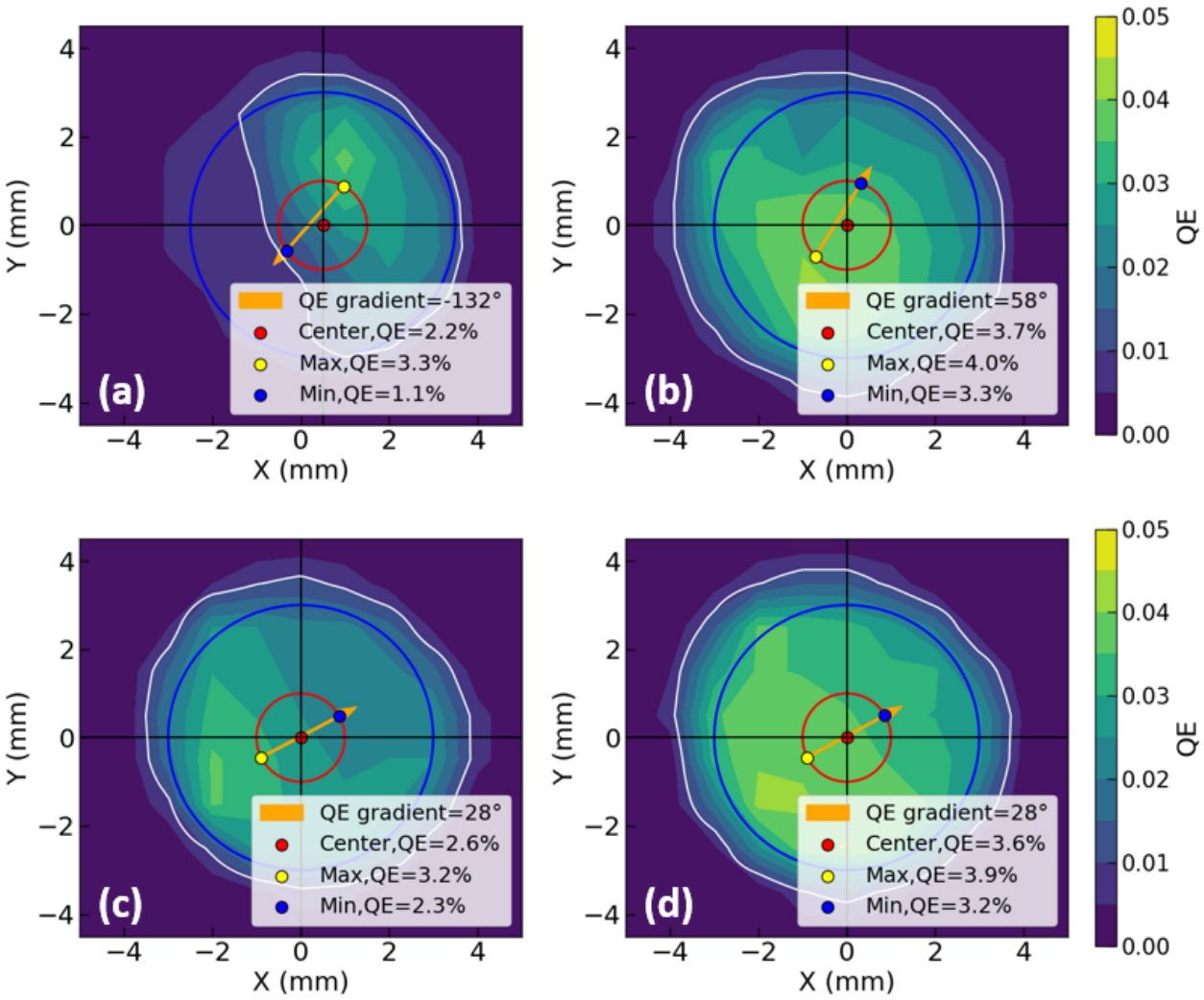


Figure 4.8: *QE maps of Na_2KSb photocathodes measured at 520 nm: (a) TWH14, (b) TWH15, (c) TWH16, and (d) TWH17.*

experimental verification proves challenging:

Accurate XPS analysis is avoid by both shadowing effects at the film edges (Figure 4.9a), and the unfocused X-ray source limiting spatial resolution. The XPS results (Figure 4.9b) show a K-rich and a Na-rich regions lying on the far left and far right of the film, corresponding to the K-Sb and Na-Sb corner in Figure 4.9a. The central area (-2 to +2 mm) exhibits a weak gradients of Na/K ratio, but not clear enough for definitive interpretation. Furthermore, the recipe-dependent nature of very surface-sensitive stoichiometry measured by Al Kα (Section 4.5.1) precludes simple universal correlations between different samples.

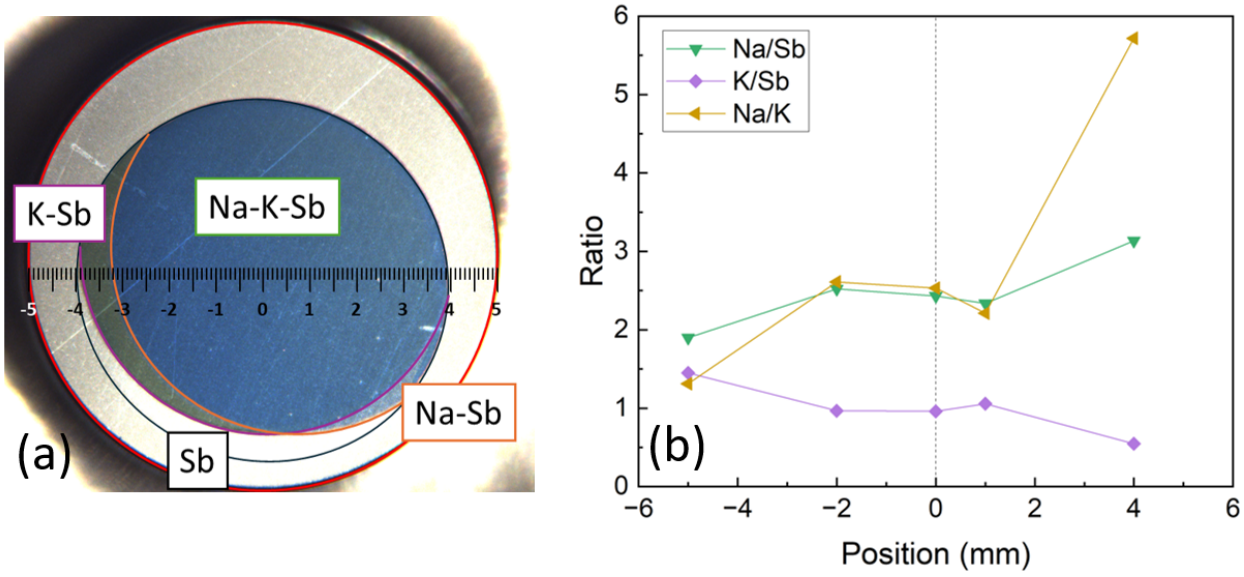


Figure 4.9: *Demonstration and local stoichiometry measurement of the TWH14 Na-K-Sb film: (a) illustration of the Na-K-Sb film with shadowing effect in the edge of the film, and (b) stoichiometry calculated from XPS (Al Kα) in different positions along the horizontal centerline of the film.*

To overcome these limitations, a model has been built to calculate the stoichiometric gradients based on geometric parameters, then correlates these predictions with measured QE maps. This integrated approach enables establishing relationships between growth parameters, reaction kinetics and QE maps, as well as guiding the optimization of the QE.

4.3.1. Model Flux Density on the Film

A coordinate system is established for flux calculations as shown in Figure 4.10, with the Mo substrate positioned in the X-Y vertical plane centered at the origin. Each effusion cell is oriented such that its crucible opening at coordinates (x_k, y_k, z_k) directs flux toward the substrate center. Given the relatively low substrate temperatures, we neglect surface diffusion effects and model the effusion cells as ideal Knudsen sources,[68] where the angular flux distribution follows the cosine law.

The flux density J(A) at any point A on the substrate decreases with the inverse

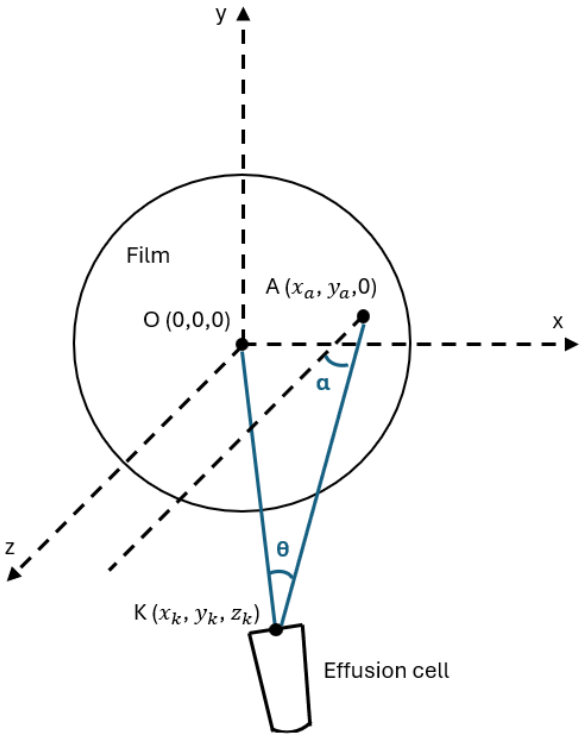


Figure 4.10: *Schematic of effusion cell, substrate in coordinate system to calculate the flux density distribution across the film.*

square of the distance d = |AK| from the source. Considering the oblique angle α between the flux direction and substrate normal, the effective flux density is:

$$J(A) = cos(\theta)\frac{J_{\text{Total}} \cdot cos(\alpha)}{4\pi d^2} = cos(\theta)\frac{J_{\text{Total}} \cdot |z_k|}{4\pi |\text{AK}|^3}. \tag{4.5}$$

where J_{Total} represents the total source flux and θ is the emission angle relative to the crucible normal. Normalizing to the central flux density at origin O yields:

$$\frac{J(\text{A})}{J(\text{O})} = cos(\theta)\frac{|\text{AK}|^3}{|\text{OK}|^3}. \tag{4.6}$$

Our calculations reveal flux variations across the 4 mm radius film: for Na/K sources, boundary values range from 90% to 110%, while Sb shows slightly better uniformity (94-107%). Figure 4.11 presents the calculated flux density ratios (Na/Sb, Na/K, and K/Sb), with the film boundary indicated by a white circle. These flux gradients provide the foundation for understanding stoichiometric vari-

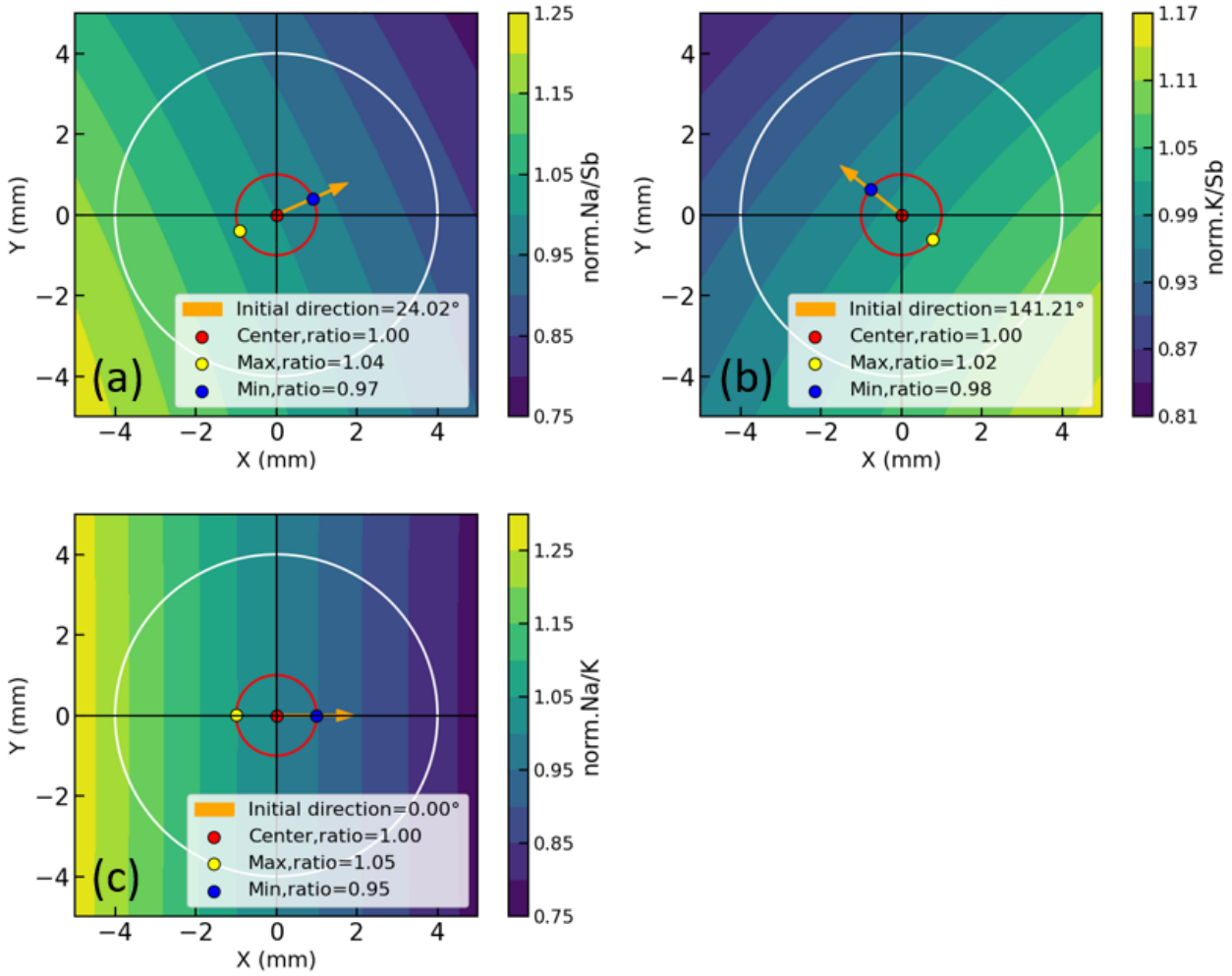


Figure 4.11: *Calculated flux density ratio of (a) Na/Sb, (b) K/Sb and (c) Na/K.*

ations across the photocathode surface.

4.3.2. Reaction Model and Stoichiometry

To establish the relationship between flux gradients and stoichiometric variations in the Na-K-Sb ternary system, a reaction model need to be built, accounting for the possible competitive reaction between alkali metals and Sb. Unlike binary systems where stoichiometry directly follows flux density gradients,[69] the ternary system introduces complexity through competing reactions:

$$\mathrm{Sb}(s) + a\mathrm{Na}(g) \xrightarrow{r_1} \mathrm{Na}_a\mathrm{Sb}(s), \quad 0 \leq a \leq 3. \tag{4.7}$$

$$\mathrm{Sb}(s) + b\mathrm{K}(g) \xrightarrow{r_2} \mathrm{K}_b\mathrm{Sb}(s), \quad 0 \leq b \leq 3. \tag{4.8}$$

We consider three distinct kinetic regimes based on the relative reaction rates of r_1 and r_2:

Case 1: Sodium-Dominated Kinetics ($r_1 \gg r_2$)

This is the most likely scenario, since Na-rich films exhibit higher stability at elevated temperature as supported by Section 2.4.2, proceeds through two sequential non-competitive reactions, with the intermediate product of $\mathrm{Na}_m\mathrm{Sb}$:

$$\mathrm{Sb}(s) + m\mathrm{Na}(g) \rightarrow \mathrm{Na}_m\mathrm{Sb}(s), \quad 0 \leq m \leq 3. \tag{4.9}$$

$$\mathrm{Na}_m\mathrm{Sb}(s) + (3-m)\mathrm{K}(g) \rightarrow \mathrm{Na}_m\mathrm{K}_{3-m}\mathrm{Sb}(s) \tag{4.10}$$

The Na/K stoichiometry gradient in film center aligns with the Na/Sb flux ratio, yielding a gradient of vector $\vec{A}$ = (0.194, 24°).

Case 2: Potassium-Dominated Kinetics ($r_1 \ll r_2$)

The reverse reaction pathway occurs with the intermediate product of $\mathrm{K}_n\mathrm{Sb}$:

$$\mathrm{Sb}(s) + n\mathrm{K}(g) \rightarrow \mathrm{K}_n\mathrm{Sb}(s), \quad 0 \leq n \leq 3. \tag{4.11}$$

$$\mathrm{K}_n\mathrm{Sb}(s) + (3-m)\mathrm{Na}(g) \rightarrow \mathrm{Na}_{3-n}\mathrm{K}_n\mathrm{Sb}(s) \tag{4.12}$$

Here, the Na/K stoichiometry gradient follows K/Sb flux, producing vector $\vec{B}$ = (0.063, -39°).

Case 3: Competitive Kinetics ($r_1 \approx r_2$)

When both reactions compete, the resultant gradient vector $\vec{C}$ becomes a linear combination:

$$\vec{C} = a\vec{A} + (1-a)\vec{B} \tag{4.13}$$

where a ∈ [0,1] represents the relative competitiveness ($a = 0.5$ for $r_1 = r_2$ yields $\vec{C}$ = (0.092, 0°)).

The model predictions are verified by comparing calculated gradient vectors ($\vec{A}$, $\vec{B}$, $\vec{C}$) with measured QE gradient directions in Figure 4.12. This analysis also provides deeper insights into the reaction kinetics of Na_2KSb formation in triple evaporation growth.

4.3.3. Correlation with QE Maps

QE mapping is performed using 520 nm monochromatic light across a 5×5 mm active area, with measurements taken at the cross of 1x1 mm grid (spot radius ≈1 mm). To enable continuous data analysis across the surface, linear interpolation is applied to the discrete QE data. The QE gradient direction at the center (0,0) was determined by calculating the angle between maximum and minimum QE values within a 1 mm radius circle - this approach minimizes uncertainties from both the exact center position determination and limited active area.

As shown in Figure 4.12, generally, the QE gradient aligns with the Na/Sb flux density gradient, supporting Case 1 ($r_1 \gg r_2$) from the reaction model. This confirms that under excess K deposition, the QE and stoichiometry are primarily governed by the Na/Sb flux ratio, consistent with our experimental observations during film growth.

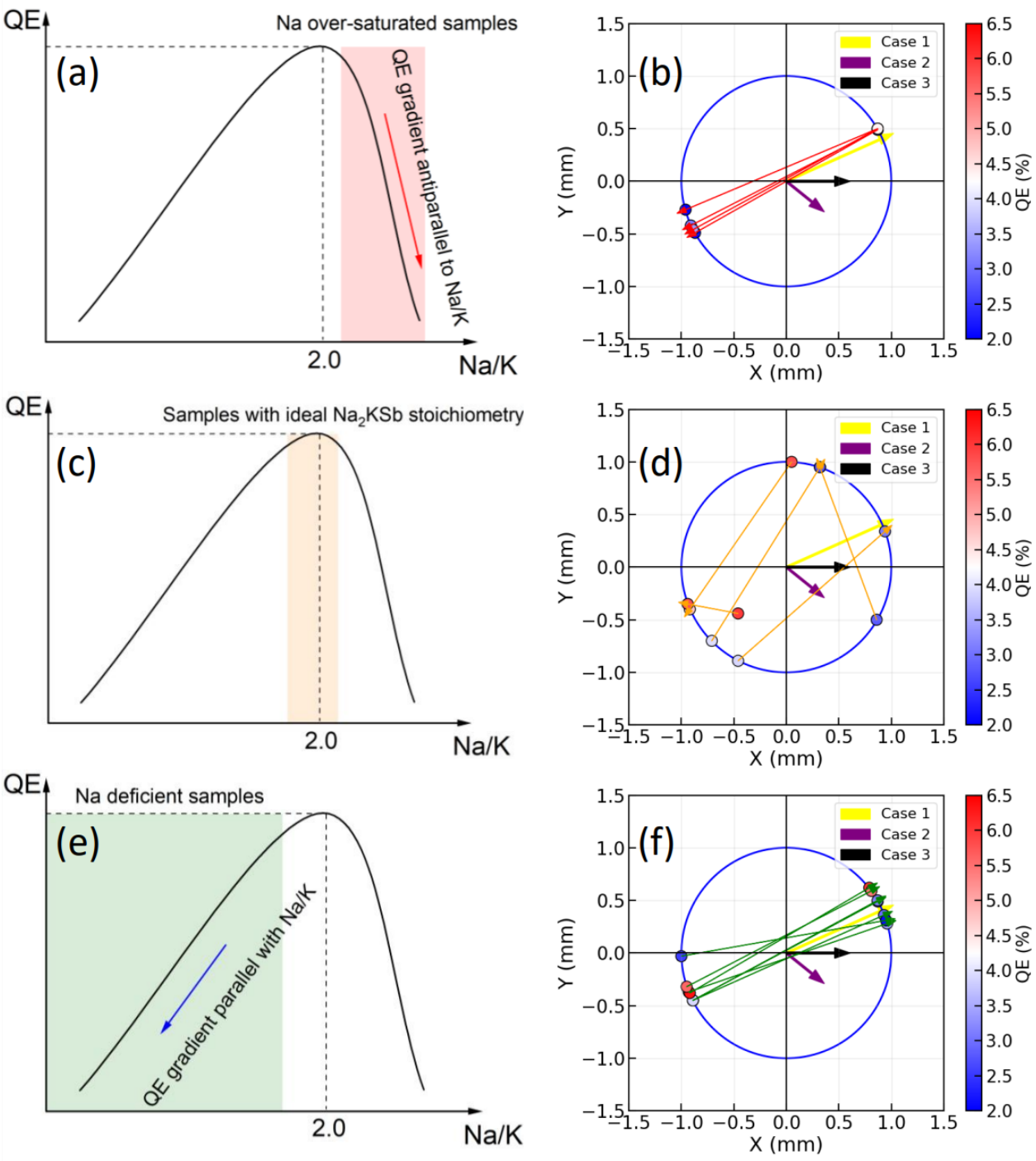


Figure 4.12: *Experimental measured QE gradient and simulated Na/K stoichiometric gradient, where Case 1, Case 2, and Case 3 represent Na-dominant, K-dominant, and competitive kinetics, respectively. (a) and (b) represent the Na-deficient (Na/K<2) samples, (c) and (d) represent the samples with near-ideal stoichiometry (Na/K≈2), and (e) and (f) represent the Na-oversaturated samples (Na/K>2).*

The QE gradients can be categorized into three distinct groups with different stoichiometric ratio between Na and K, each exhibiting characteristic behavior:

Group 1: Na-deficient samples (Na/K$<$2)

As shown in Figure 4.12a and b, they display positive correlation between QE and Na/K ratio, and demonstrate QE gradient directions parallel to Na/Sb flux gradient.

Group 2: Near-ideal stoichiometry (Na/K$\approx$2)

As shown in Figure 4.12c and d, They have a near-ideal stoichiometry and show irregular gradient direction as the optimal composition is achieved near center.

Group 3: Na-oversaturated samples (Na/K$>$2)

As shown in Figure 4.12e and f, they show an inverse correlation between QE and Na/K ratio, with the direction of QE gradient anti-parallel to Na/Sb gradient.

This systematic analysis demonstrates that the QE gradient direction serves as an effective indicator of the stoichiometry. Therefore, theoretically, we are able to do appropriate fine-tuning after growth to achieve the optimal stoichiometry and approaching the maximal QE of Na_2KSb film.

4.4. Maximizing QE in the Center of the Na-K-Sb Photocathode Films

To validate the relationships between QE and stoichiometric gradient established in previous sections, we conducted systematic experiments to optimize the QE in Na-K-Sb photocathodes. Two distinct sample series (TWH22 and TWH19) were used to demonstrate fine-tuning methods for Na-oversaturated and Na-deficient films, respectively.

4.4.1. Maximizing QE for Na Oversaturated Samples

TWH22 was a slightly Na oversaturated sample synthesis using triple evaporation method described in Section 4.2.1, the duration of Phase II was set to 0 to create a Na oversaturated sample. Following initial growth, I implemented stepwise Sb+K compensation to it including a co-deposition of extra 0.3 nm (5 min, 0.01Å/s) Sb and excessive K (0.04Å/s) until QE peaks at 110 °C, followed by standard Phase III, corresponding to Tri-2 recipe. 48-hour storage lifetime measurement and QE mapping was implemented after the initial growth and each 5-min-Sb+K compensation.

As shown in Figure 4.13, this approach progressive tuned the film properties. Initial QE gradient of TWH22 (-151°) confirmed Na over-saturation with relative low QE (4.0%) in the center of the film (Figure 4.13a). After 5 minutes compensation, 6.0% QE with homogeneous distribution (Figure 4.13b) was achieved. After 10 min compensation, peak QE increased to over 6.5%, locating in the lower left corner, as shown in Figure 4.13c. After 15 min compensation, the film was transited to a Na-deficient sample (QE gradient 27°, center QE reduced to 5.5%, as shown in Figure 4.13d.

This series experiment demonstrates that controlled Sb+K compensation can effectively optimize Na-oversaturated films to achieve 6% in the center of the film.

4.4.2. Maximizing QE for Na deficient samples

TWH19 series is a parallel experiments on Na deficient sample. The initial growth procedure is in consist with TWH22, apart form a reduced Na deposition rate in Phase I. After the initial deposition, extra 1.8 nm (10 min, 0.03Å/s) Na was deposited onto the film at 170 °C, with K effusion cell on to compensate K loss until sample cooling down. 24-hour storage lifetime measurement, QE mapping and XPS was implemented between the initial growth and each 10-min-Na deposition.

After initial deposition, TWH19 is a Na deficient sample, with 1.4% central

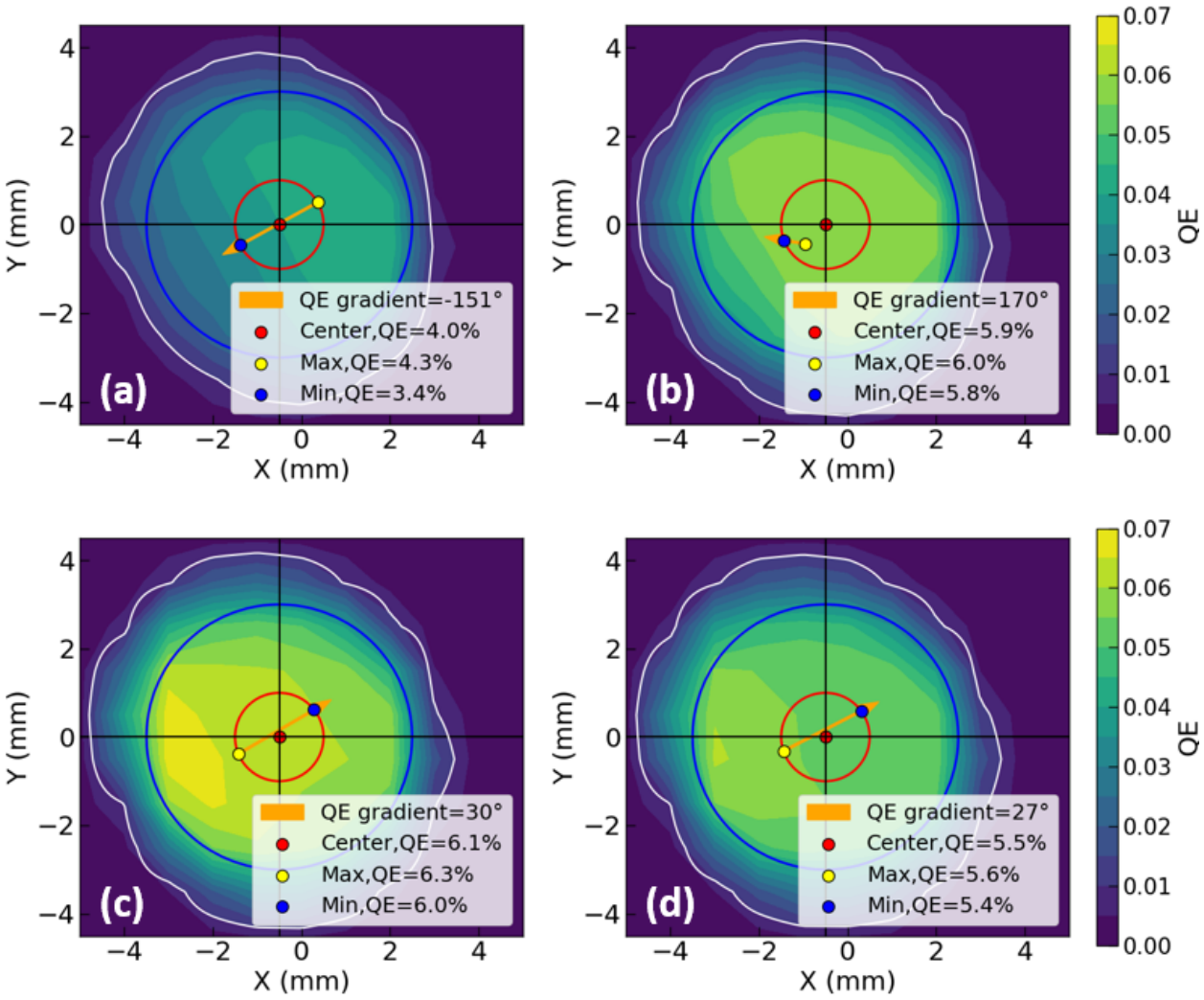


Figure 4.13: *QE maps of TWH22, measured at 520 nm: (a) TWH22, (b) TWH22 + 5 min Sb+K, (c) TWH22 + 10 min Sb+K, and (d) TWH22 + 15 min Sb+K.*

QE, which is too low for QE mapping. After 10 minutes Na-deposition (Figure 4.14a), the QE gradient is measured to be 19°, corresponding to Na deficient samples with the center QE increased to 3.8%. After 20 minutes Na-deposition (Figure 4.14b), the QE in the center increased further to 5.5%, indicating the positive effect of the QE fine-tuning. After 30 minutes and 40 minutes Na-deposition (Figure 4.14c and d), the center QE fall back to 3.9% and 2.2%, respectively. They were transited to Na oversaturated sample with their QE gradients measured to be at around -150°.

This series experiment confirms the Na compensation on Na deficient sample

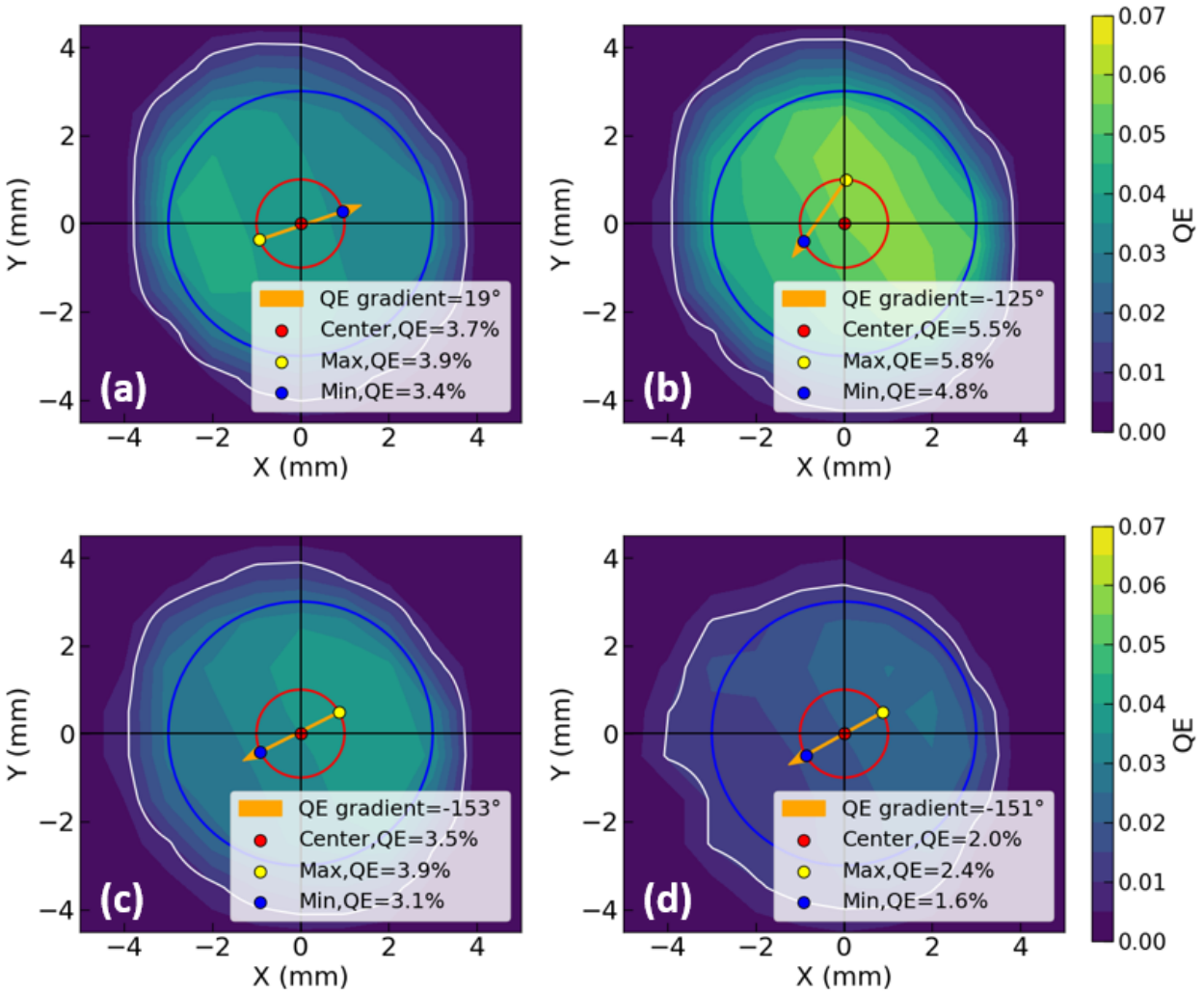


Figure 4.14: *QE maps of TWH19, measured at 520 nm: (a) TWH19 + 10 mins Na, (b) TWH19 + 20 mins Na, (c) TWH19 + 30 mins Na, and (d) TWH19 + 40 mins Na.*

can elevate the QE of Na deficient films above 5%.

4.4.3. Reducing Inhomogeneity by Decreasing the Angular Separation between Na and Sb Sources

The requirements for high-current applications, such as Energy Recovery Linac (ERL) projects, necessitate photocathodes with a large, homogeneous active area exhibiting high QE in the center. A larger laser spot size is often employed to enhance the operational lifetime of photocathode in the gun, making surface QE

uniformity an important requirement of photocathode. In addition, chemical homogeneity also helps reduce the MTE of the emitted electron beam and improve beam brightness in photoinjector.

As established in the previous section, the QE gradient directly aligns with the Na/Sb flux gradient. Our calculations indicated that the magnitude of this flux gradient, and by extension the resulting stoichiometric and QE inhomogeneity, could be significantly reduced by minimizing the angular separation between the Na and Sb sources. To experimentally validate this hypothesis, the source positions is reconfigured, reducing the angle between the Na and Sb sources from 69° to 45°, the calculation predicting a reduced in inhomogeneity to 61%.

The QE maps of samples TWH25 and TWH26, grown using the Tri-2 triple evaporation method with this new geometry, are presented in Figure 4.15. Both maps demonstrate a markedly more homogeneous QE distribution over a large area compared to films produced with the previous setup (e.g., Figure 4.13), thereby conclusively confirming the correctness of our assumption that geometric source arrangement is a key factor in achieving high QE homogeneity.

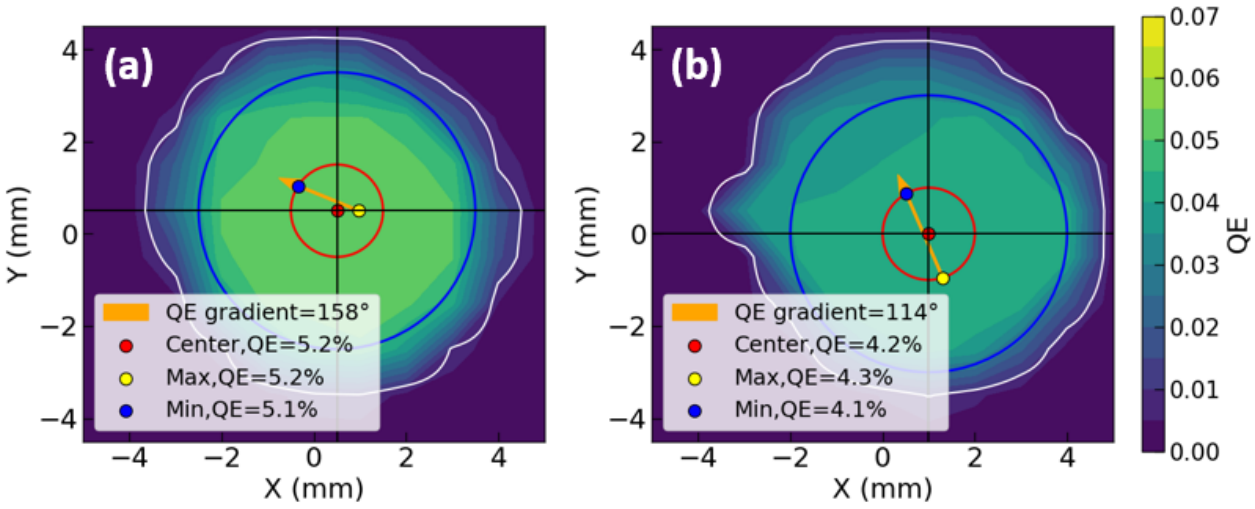


Figure 4.15: *QE maps measured at 520 nm of (a) TWH25 and (b) TWH26, with Tri-2 triple evaporation method and reduced angular separation between the Na and Sb sources.*

4.5. Statistical Results of Stoichiometry and Photoemissive Properties

This section presents the statistical results between XPS calculated stoichiometry and the photoemissive properties of Na-K-Sb series photocathodes, including QE and storage lifetime, and explores the correlation between them.

4.5.1. QE and Stoichiometry

The QE (measured at 515 nm or 520 nm) and stoichiometry calculated from Al Kα of 37 Na-K-Sb films is shown in Figure 4.16. Here, we have proved the assumption from Section 4.1.5, that the qualified Na-K-Sb samples (QE $> 3\ \%$, Storage lifetime $> 150\,\mathrm{h}$) mostly occurs within the optimal stoichiometry zone of the K/Sb ratio between 0.90 and 1.25, with only 2 exceptional samples grown with sequential method (TWH12, TWH19+2Na). When the K/Sb ratio is smaller than 0.90, the photocathode film is either a low QE or exhibiting extremely low storage lifetime. And when the K/Sb ratio is larger than 1.25, the photocathode film have a low QE. Additionally, we can see the benefit of triple evaporation method (square) in fine stoichiometry controlling compared with sequential/alkali-codepostion method (triangle), since it has a relative smaller K/Sb distribution than the latter, resulting in a high reproducibility in high-QE photocathode production.

The next step is to explore the correlation between stoichiometry and QE of the Na-K-Sb photocathode system in the similar experiment condition. Two series of samples grown with different methods are demonstrated in Figure 4.17, the growth protocol within the experiment series is same. For both series, the trend of the curve is similar: there is a optimized K/Sb ratio for the highest QE sample. However, for Tri-1 series samples, the peak QE (6.3%) occurs at a K/Sb ratio of 0.95. While, for TWH19 series samples, which can be seen as sequential method samples with stepwise Na deposition (details in Section 4.4.2), the peak QE (5.9%) occurs at a K/Sb ratio of 0.78, much lower than the triple evaporation samples. Additionally, the K/Sb ratio of TWH19+3Na and TWH19+4Na is apparently much higher than acceptable range for photonsentive Na_2KSb films,[22] but

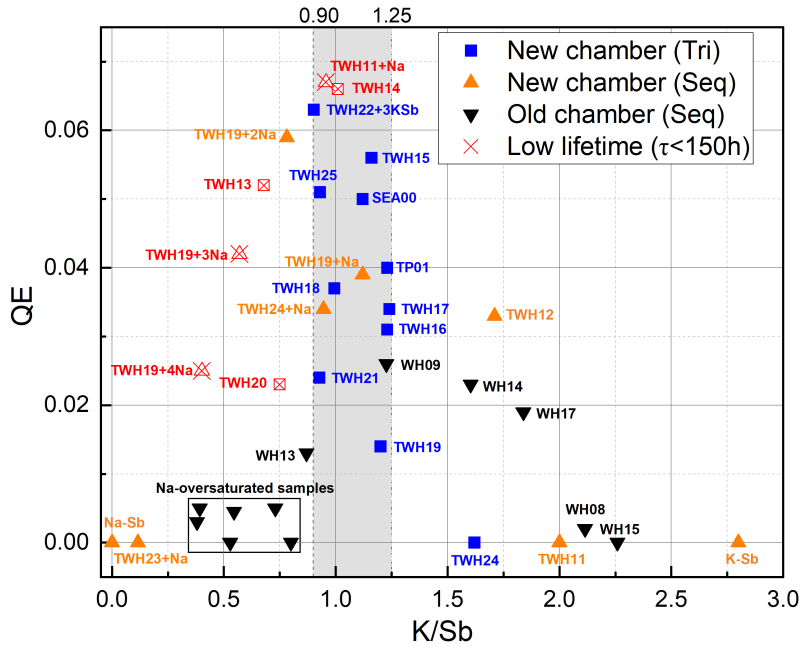


Figure 4.16: *Surface stoichiometry (from Al Kα) and QE of 37 Na-K-Sb films with different growth methods, including triple evaporation in new chamber and sequential/alkali-codepostion in new and old chamber, with shaded area representing the optimal stoichiometric zone for high-QE and long-storage-lifetime Na-K-Sb photocathodes.*

still remains over 2% QE.

This illustrates that the attempt of finding universal correlations across different growth methods is challenging, due to that the growth protocol within the experiments are different. Therefore, as shown in Figure 4.16, the distribution of QE and K/Sb ratio seems to be quite random within the narrow optimal stoichiometry zone.

This random "misalignment" between QE and stoichiometry possibly can be explained by the high surface sensitive of XPS analysis. Its characterization depth is much shorter than the QE resolving depth, which is assumed to be controlled by the electron attenuation length with regard to the electron energy. Although no study found for the direct measurement of the electron attenuation lengths in Na-K-Sb material system. The attenuation length in another alkali-antimonide Cs_3Sb is reported to be of is 26 nm for 2.34 eV photoelectrons excited with 530 nm laser

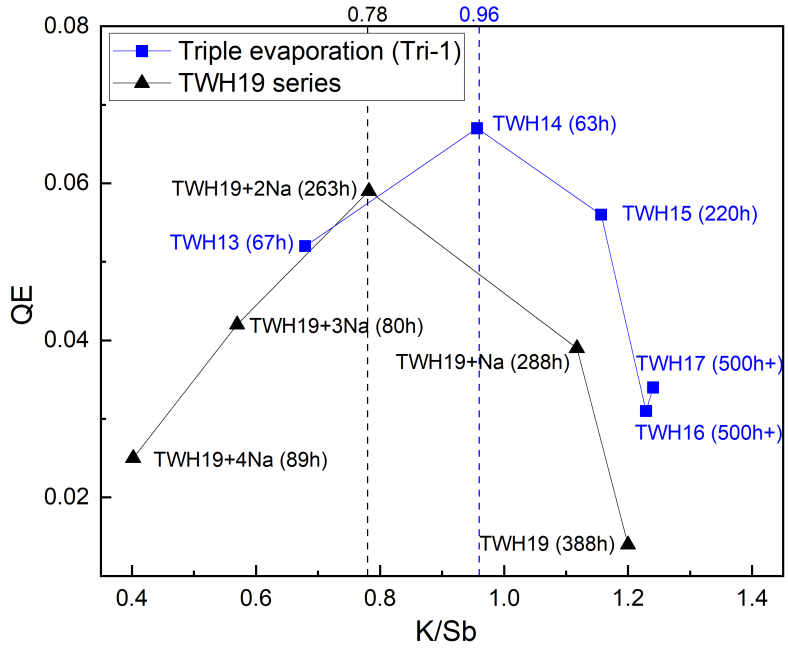


Figure 4.17: *Stoichiometry, QE and storage lifetime of triple evaporated (Tri-1 series) and stepwise Na sequential evaporated (TWH19 series) Na-K-Sb photocathodes.*

based on the study of the Seah and Dench, several related experiments or calculations also obtained similar results.[22,31,70,71] This value is on the same order of magnitude as the minimal thickness of Na_2KSb for QE saturation with 2.4 eV incident light during growth, assumed to be 23 to 34 nm. Meanwhile, the IMFP of photoelectrons excited by Mg Kα and Al Kα X-rays from Na, K and Sb core level range from 0.9 to 3.5 nm, resulting in a characterization depth (3 times IMFP) only count for around 30% of the thickness related to photoelectric properties. Therefore, if the elements are not distributed homogeneous in depth, the stoichiometry calculated form XPS layer can not reflex the average stoichiometry in the whole QE resolving thickness.

To instigate the in-depth stoichiometry distribution, XPS is measured with both Al Kα and Mg Kα X-ray source to conduct the depth-dependent composition analysis. Al Kα has a relative higher energy than Mg Kα, resulting in a 74%, 19% and 24% deeper probing for Na 1s, K 2p and Sb 3d core level, respectively. The stoichiometric gradient of Na, K and Sb is therefore calculated form dividing their

stoichiometry in Mg Kα (more surface sensitive) by that in Al Kα (less surface sensitive), with a higher value representing more surface concentrated. Here, to determine their stoichiometric gradient, the peak areas are collected from the spectra of the Na 1s (1075 - 1068 eV), K 2p (310 - 290 eV) and Sb 3d (550 - 522 eV) region scans with Shirley background subtraction applied. The energy loss peak is not counting in for Na 1s, since it resulting in large uncertainty after Shirley background subtraction, especially for Mg Kα spectra, where the Na 1s has a high background noise.

The gradients of Na/Sb and K/Sb and their stoichiometry measured are summarized in Table 4.3 with their maximal QE and storage lifetime (smoothed with 5 pts FFT smooth method and fitting with function $QE = A \times \exp(-t/\tau)$). In TWH19-series samples, as more Na deposits on the surface, the gradient of Na/Sb increases gradually from 1.07 in TWH19 to 1.35 in TWH19+4Na, suggesting extra Na deposition creating a highly Na concentrated surface. Until this value is similar to the Na/Sb value in Na-Sb system, suggesting the trend of Na sticking to the surface of the film, which could possibly be explained by the property of Na in the vacuum.[72,73] As a comparison, the gradient of Na/Sb is stable at around 1.16 for triple evaporation samples, except for TWH16, since the Na diffusion possibly weakened by the the low substrate temperature during Phase II.

The result demonstrated that the different deposition methods may resulting in in-depth inhomogeneity of the the film. This contributes to the deviation in stoichiometry measurement of the Na-K-Sb film, making it difficult to find the universal correlations between stoichiometry and QE with current data.

4.5.2. Storage Lifetime and Stoichiometry

The similar analysis process is also adopt to this section, to test the assumption in Section 4.2.2.2: Na oversaturated will negative affect the storage lifetime of the sample.

First is to explore the correlation between stoichiometry and lifetime in same

Table 4.3: *Summary of photoemissive properties, stoichiometry and in-depth stoichiometic gradient of Na_2KSb photocathodes prepared with stepwise sequential method (TWH19 series), and triple evaporation method with different Phase II temperature (TWH22 series, TWH25 and TWH14-TWH17). Full data is shown in Section A.4.*

Sample	Peak QE	Lifetime	Stoichiometry	Na/K	Na/Sb and K/Sb Gradient
TWH19	1.4%	388h*	$Na_{2.0}K_{1.2}Sb_{1.0}$	1.6	1.07/1.10
TWH19+Na	3.9%	288h	$Na_{2.2}K_{1.1}Sb_{1.0}$	2.0	1.11/1.23
TWH19+2Na	5.9%	263h*	$Na_{2.5}K_{0.8}Sb_{1.0}$	3.1	1.28/1.22
TWH19+3Na	4.2%	80h	$Na_{2.9}K_{0.6}Sb_{1.0}$	5.0	1.34/-
TWH19+4Na	2.5%	89h	$Na_{3.1}K_{0.4}Sb_{1.0}$	7.8	1.35/-
Na-Sb	0%	-	$Na_{3.2}Sb_{1.0}$	-	1.35/-
TWH22(110°C)	4.7%	500h+	-	-	-
TWH22+KSb(110°C)	6.2%	500h+	-	-	-
TWH22+2KSb(110°C)	6.5%	526h	-	-	-
TWH22+3KSb(110°C)	6.3%	279h	$Na_{2.3}K_{0.9}Sb_{1.0}$	2.5	1.16/1.31
TWH25(110°C)	5.1%	500h+*	$Na_{1.8}K_{0.9}Sb_{1.0}$	2.0	1.17/1.28
TWH17(95°C)	3.4%	500h+	$Na_{1.9}K_{1.2}Sb_{1.0}$	1.5	1.15/1.27
TWH16(73°C)	3.1%	500h+	$Na_{1.9}K_{1.2}Sb_{1.0}$	1.6	1.03/1.25
TWH15(100°C)	5.6%	220h	$Na_{2.2}K_{1.2}Sb_{1.0}$	1.9	-
TWH14(90°C)	6.7%	63h	$Na_{2.4}K_{1.0}Sb_{1.0}$	2.6	-

*The coefficient of determination (COD) of the fitted lifetime curve is smaller than 0.85, due to the short measurement time.

sample series. As plotted in Figure 4.18 and summarized in Table 4.3, storage lifetime dropped as the decrease of the K/Sb within the range of 1.3 to 0.4 for both TWH19 series and triple evaporation (Tri-1) samples. For TWH19 series, as shown in Figure 4.18a, the QE of TWH19 shows only minimal degradation during the 20 hours' measurement period, its storage lifetime is assumed to be around 388 hours. As further Na deposition, the 1/e lifetime decreases to around 200-300 hours for TWH19+Na and TWH19+2Na and around 80-90 hours for sample TWH19+3Na and TWH19+4Na.

For further confirm the correctness of the above result, all samples prepared in triple evaporation chamber is shown in Figure 4.19 with their storage lifetime and

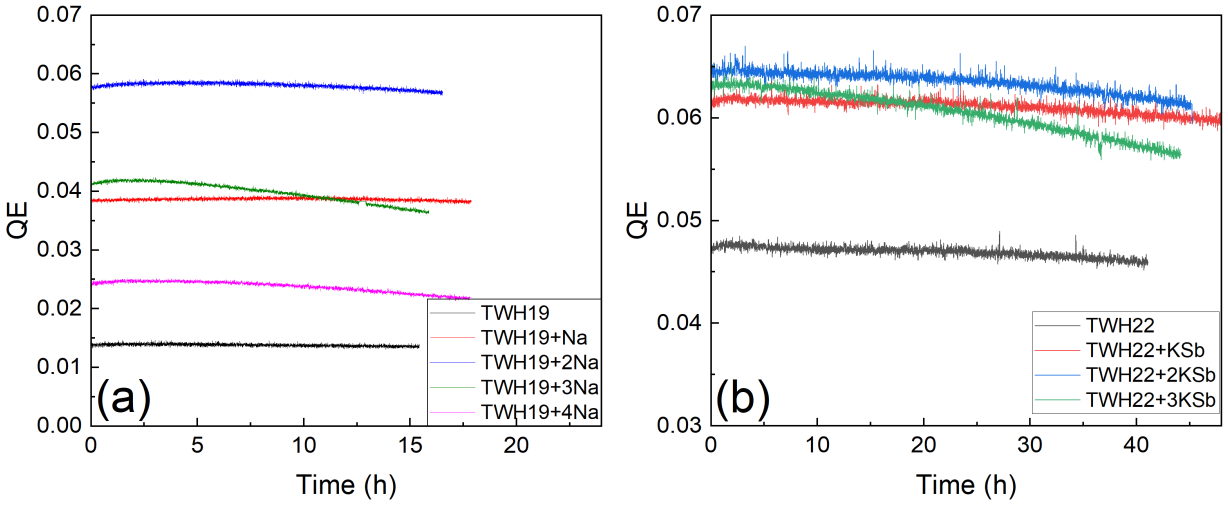


Figure 4.18: *Storage lifetime of TWH19 series and TWH22 series Na-K-Sb photocathodes, (a) TWH19 series, (b) TWH22 series.*

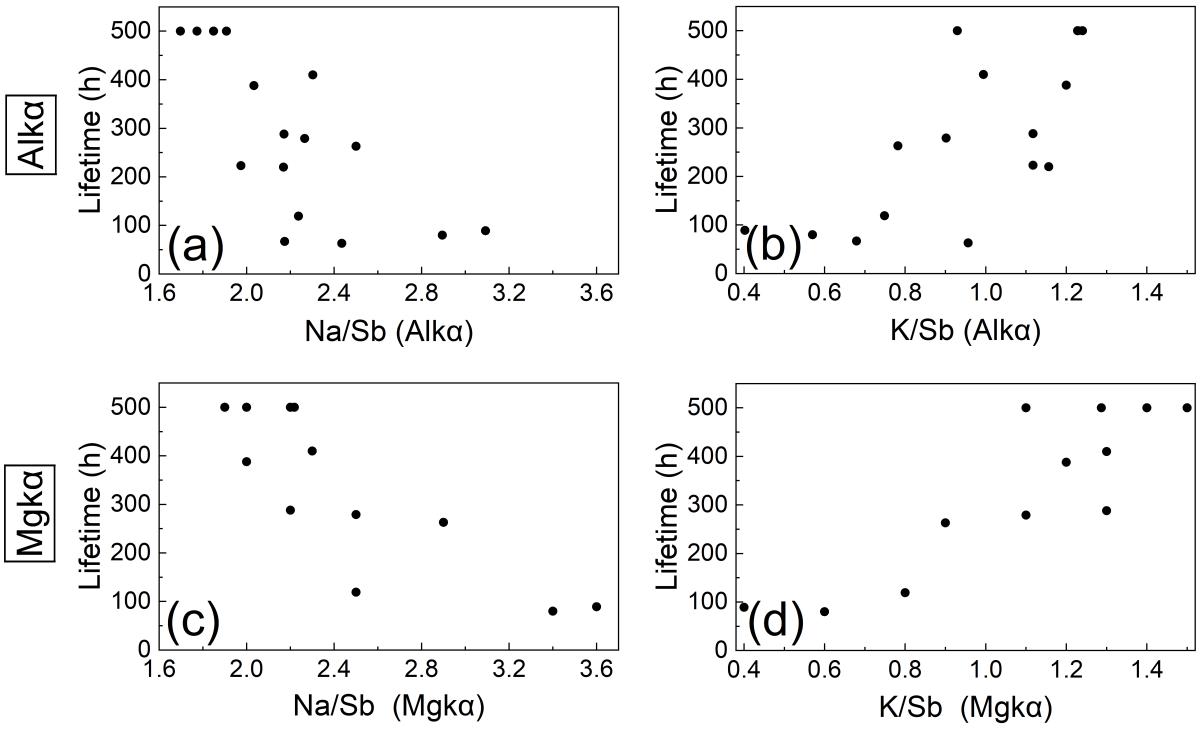


Figure 4.19: *Storage lifetime is shown in the function of the stoichiometry of Na-K-Sb photocathodes films, (a) and (b) measured in Al Kα, (c) and (d) in Mg Kα.*

stoichiometry measured in Al Kα and Mg Kα. And the result show the Pear-

son correlation coefficient between lifetime and Na/Sb and K/Sb measured with Mg Kα are -0.84 and 0.88 and that of Na/Sb and K/Sb measured with Al Kα are -0.73 and 0.72. Therefore, we can consider that the Na oversaturated, is correlated to the short storage lifetime in Na-K-Sb system.

It is crucial to distinguish that the storage lifetime measured in this UHV environment primarily reflects the degradation kinetics of the high-QE Na_2KSb phase, rather than its resistance to oxidation. Under this UHV conditions (Section 3.2.2.1), the partial pressure of residual gases is negligible, as indicated by low O 1s peak intensity in XPS spectra (Figure 6.6f). Therefore, attributing the observed QE decay to oxidation processes under these conditions is not supported by the evidence. A definitive evaluation of the material's oxidation resistance requires dedicated, controlled studies involving exposure to defined partial pressures of oxygen or water vapor.

4.6. Spectral Response Curve

4.6.1. Photoemission Models and Curve Fitting

This section presents the spectral response curve fitting for Na_2KSb photocathodes, following the theoretical models introduced in Section 2.3.3.

The spectral response curve of a representative Na_2KSb photocathode (TWH25, Na:K ≈ 2) is shown in Figure 4.20 and was fitted using three distinct models across different photon energy ranges:

Urbach model ($QE(h\nu) = \exp(A + B \cdot h\nu)$) was applied to the low-energy exponential tail (1.8–1.9 eV, $h\nu < E_{\mathrm{T}}$).

Kane model ($QE(h\nu) = C(h\nu - E_{\mathrm{T}})^n$) was used near the threshold (2.0–2.4 eV, $h\nu > E_{\mathrm{T}}$) to determine the power-law dependence.[74]

Spicer three-step model ($QE(h\nu) = \frac{D(h\nu - E_{\mathrm{T}})^{3/2}}{(h\nu - E_{\mathrm{T}})^{3/2} + \gamma}$) was fitted across the primary response range (2.0–3.0 eV, $h\nu > E_{\mathrm{T}}$).[22]

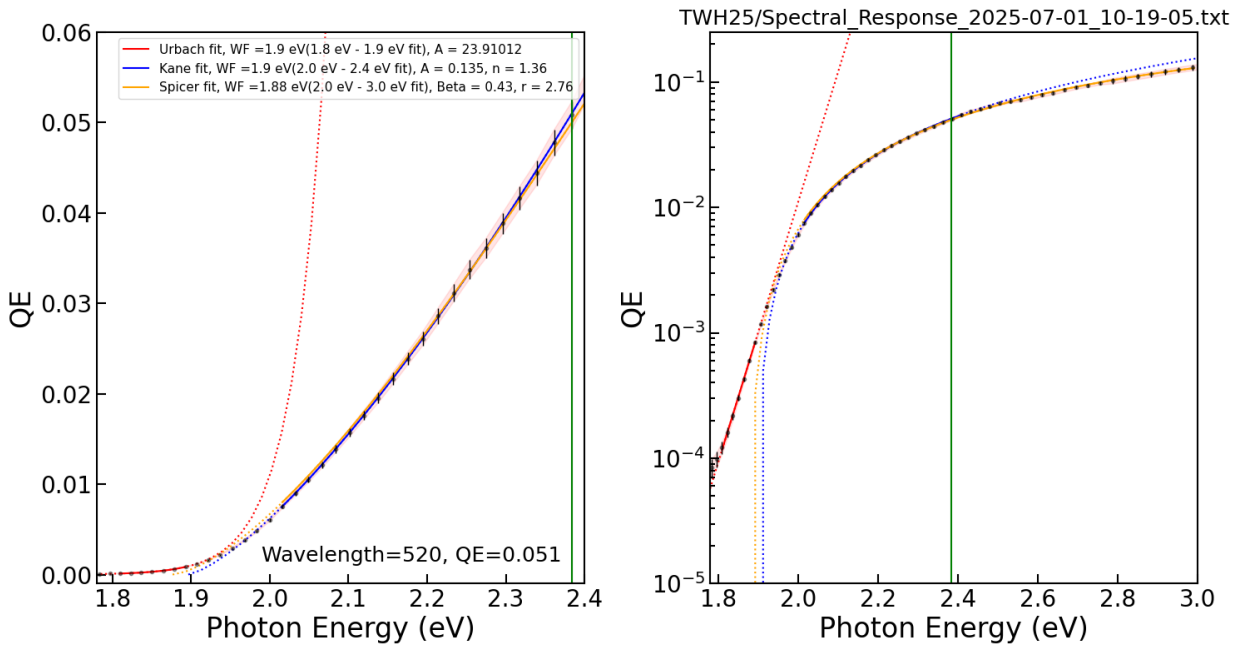


Figure 4.20: *Spectral response curve of TWH25, fitted by Urbach, Kane and Spicer model. Left: QE shown in linear y-axis. Right: QE shown in logarithmic y-axis.*

The fitting parameters for four Tri-2-grown Na_2KSb photocathodes are summarized in Table 4.4, revealing several key findings:

Threshold Energy Consistency: The threshold energy E_T determined from both Urbach and Kane models consistently falls between 1.90 and 1.95 eV, with a difference of less than 0.02 eV between the two methods. This aligns with values reported in prior publications.[9,22] An exception was observed in Na-surface-enriched samples, where E_T dropped below 1.8 eV, consistent with Fisher's report.[75] This situation will be discussed separately in Section 4.6.2.

Variable Shape Factor: The Kane model shape factor n is not constant across samples, indicating variations in photon absorption, carrier scattering, or electron escape mechanisms. This variability contradicts the fixed $n = 1.5$ assumption in the Spicer model, leading to larger errors in E_T determination when that model is used. The value of n is influenced by the growth procedure, as to be discussed in Section 4.6.2.

Urbach Energy and Temperature Dependence: The valence band energy broadening $\Delta E(T)$, derived from the Urbach parameter B ($B = 1/\Delta E(T)$), is approximately 0.04 eV at room temperature. This value is consistent with reports for polycrystalline Cs_3Sb films[23] and is typical for the exponential tail width in disordered semiconductors.[76] As theoretically predicted, $\Delta E(T)$ increases with temperature due to enhanced disorder, rising from 0.043 eV at room temperature to 0.053 eV at 110 °C for sample TWH18 (see Section A.3.1). While verifying the quantitative relationship requires additional experiments at cryogenic temperatures.

Table 4.4: *Urbach, Kane and Spicer fitting of the four Na_2KSb photocathodes grown by triple evaporation (Tri-2) method.*

Sample	Urbach		Kane			Spicer			QE_{520nm}
	B	E_T	C	n	E_T	D	γ	E_T	
TWH25	23.9	1.90	0.13	1.36	1.90	0.43	2.76	1.88	5.1%
SEA03	25.9	1.89	0.13	1.18	1.90	0.60	3.96	1.85	5.4%
TWH26	25.0	1.93	0.09	1.32	1.91	0.60	4.91	1.93	3.4%
TP01	25.5	1.93	0.10	1.08	1.95	0.59	5.65	1.84	4.0%
Average	25.1	1.91	0.11	1.24	1.92	0.56	4.32	1.88	-
STD	0.87	0.02	0.02	0.13	0.02	0.08	1.25	0.04	-

4.6.2. Spectral Response Dependence on Growth Method

This section compares the spectral response of the TWH19 and TWH22 series (growth parameters detailed in Section 4.4) to explain the impact of different synthesis methods.

The spectral response curves (Figure 4.21, summarized in Table 4.5) reveal distinct trends: For TWH22 (Tri-2 method), the threshold energy E_T remained nearly constant as extra K-Sb layers were deposited. While for TWH19 (sequential Na deposition), E_T decreased from over 1.9 eV to below 1.8 eV after the third and fourth Na deposition. The latter value is close to the 1.75 eV threshold re-

ported by Fisher.[75] The lower E_T may result from the formation of stoichiometric Na_2KSb or from an n-type Na_3Sb surface layer inducing downward band bending on a p-type Na_2KSb bulk.

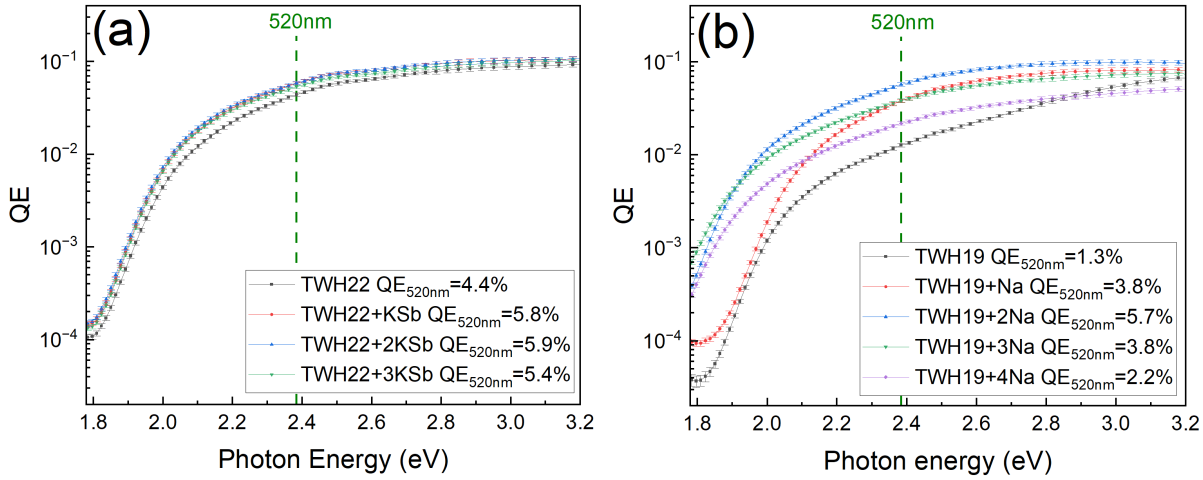


Figure 4.21: *Spectral response curve of TWH19 and TWH22 series Na_2KSb photocathodes. (a) TWH22 series, (b) TWH19 series.*

Table 4.5: *Urbach and Kane fitting of TWH19 and TWH22 series Na_2KSb photocathodes.*

TWH22	Urbach		Kane		QE	TWH19	Urbach		Kane		QE
	B	E_T	n	E_T			B	E_T	n	E_T	
Original	21.1	1.92	1.37	1.92	4.4%	Original	22.3	1.98	1.37	1.92	1.3%
+KSb	22.0	1.89	1.12	1.93	5.8%	+Na	21.6	1.97	1.47	1.95	3.8%
+2KSb	22.1	1.89	1.09	1.94	5.9%	+2Na	21.7	1.82	1.40	1.82	5.7%
+3KSb	22.0	1.90	1.07	1.94	5.3%	+3Na	-	-	1.47	1.76	3.8%
						+4Na	-	-	1.45	1.78	2.2%

The growth method also influences the Kane shape factor n. The initial n for both TWH22 and TWH19 was 1.37. Subsequent K-Sb deposition (TWH22 series) decreased n, while additional Na deposition (TWH19 series) increased it.

Furthermore, as shown in Section A.3.2, within a single sample, areas with higher Na concentration exhibit a larger n. However, more experimental data are needed to determine the correlation between stoichiometry/grown method and factor n.

5. Beam Commissioning at SEALab with Na_2KSb Photocathodes

This chapter introduces the performance of Na_2KSb photocathodes as a subsystem during the beam commissioning at SEALab, conducted from winter 2024 to summer 2025.

The experiment setup of the SRF gun system (detailed in Section 2.1) was completed in summer 2024. Subsequently, three Na_2KSb photocathodes (SEA01-SEA03) were sequentially transferred into the gun for commissioning. The initial attempt with SEA01 in winter 2024 was interrupted due to a technical incident involving the RF-power supply, which resulted in damage to the warm section of the high-power RF input window. Consequently, no operational photocathode data were obtained during this first attempt.

5.1. First Successful Beam Commissioning with SEA02

After the repair, the second commissioning attempt using photocathode SEA02 in spring 2025 successfully achieved first beam in March 2025. The gun subsequently operated for 13 weeks from March to May.[14] During this period, the Na_2KSb photocathode shows good compatibility with the SRF electron gun and supported the commissioning of other subsystems—including the laser, cavity, and solenoid—by providing a stable electron beam at low average currents (1–$10\,\mu\mathrm{A}$), maintaining a QE between 10^{-3} to 10^{-4} despite several vacuum events producing pressure bursts up to $1 \times 10^{-8}\,\mathrm{mbar}$.

While this demonstrated basic functionality, the achieved QE was insufficient for high-current applications. Analysis following the run identified two critical problems requiring urgent optimization before the next commissioning phase in July 2025:

1) Growth Recipe Optimization

As discussed in Section 4.1.2, the initial triple evaporation recipe presented a fundamental trade-off: extended storage lifetime (>500 hours) was achieved at the cost of reduced QE (∼3%), a value less than half that reported in literature[9]. Therefore, optimizing a growth recipe capable of simultaneously delivering high QE and long storage lifetime remained a primary challenge.

2) Transfer Process

Photocathode SEA02 exhibited a QE of 2.5% at 521 nm post-growth in the preparation chamber. However, the QE degraded by one order of magnitude during the transfer procedure and lost another order of magnitude after moving from the warm to the cold section of the SRF gun. The main problem was probably the surface oxidation due to a high partial pressure of water vapor in the transfer system, as shown by residual gas analysis (RGA) data in Figure 5.1.

It is urgent to solve these two problems—recipe refinement and transfer induced degradation— for the success of the subsequent beam commissioning.

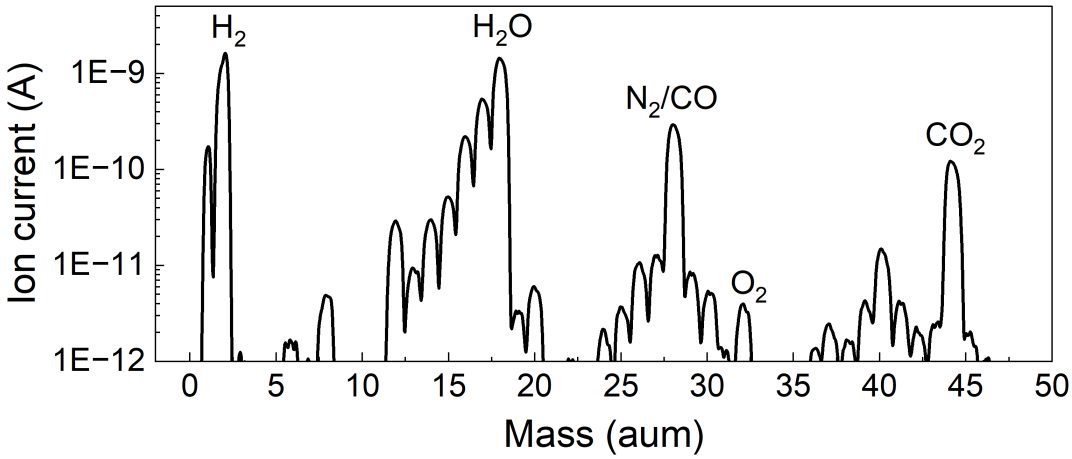


Figure 5.1: *Residual gas analysis (RGA) spectrum of transfer system 2, measured on 13 March 2025, one week prior to the transfer of SEA02. The high ion current of water vapor is observed.*

5.2. Second Beam Commissioning with SEA03

This section presents the experimental progress and performance of the latest Na_2KSb photocathode (SEA03) during the second beam commissioning at the

SEALab photoinjector, including its growth, transfer, and operational results.

5.2.1. Growth of SEA03

Photocathode SEA03 was prepared using the optimized triple-evaporation method (Tri-2), demonstrating reproducibility, and high QE ($\sim$5%) with long storage lifetime ($>$500h). A substrate (real-Mo plug) designed for SEALab was employed.[45] Due to the different geometry and thermal mass of this real-Mo plug compared to the standard full-Mo plug (Figure 3.1), the sample stage temperature was set to 100 °C during growth. This adjustment compensated for the increased thermal effect due to reduced mass, ensuring the substrate surface temperature was equivalent to that of previous photocathodes. To improve surface homogeneity, the positions of the Na and K effusion cells were swapped, reducing the angular separation between the Na and Sb sources and thereby minimizing the QE gradient across the film, as discussed in Section 4.4.3.

As shown in Figure 5.2a, the Tri-2 recipe was designed to enhance the compatibility between high QE and storage lifetime. In phase I, simultaneous co-deposition of Sb (0.01 Å/s), Na (0.04 Å/s), and K (0.12 Å/s) proceeded for approximately 200 minutes, with a Sb thickness of 12 nm. During phase II, the Na shutter was closed while additional Sb and K were deposited for 7 minutes (0.4 nm Sb). Crucially, the substrate temperature was maintained at the phase I to enhance the formation of more homogeneous Na_2KSb layer. In phase III, the Sb shutter was closed and the sample was cooled while a lower flux of K was maintained. One day post-growth, the central QE was measured at 5.4%. The color of the film was similar to sample TWH14 in Figure 4.9.

The QE maps of the SEA-series samples are compared in Figure 5.3. SEA03, produced with the Tri-2 method, exhibits a significantly higher QE than SEA00-SEA02 (Tri-1 method). The inhomogeneity, quantified as $(QE_{\text{max}} - QE_{\text{min}})/QE_{\text{max}}$ within a 1 mm radius, was 0.14 for SEA03, significantly lower than the values of 0.44, 0.30, and 0.46 for SEA00, SEA01, and SEA02, respectively. This improve-

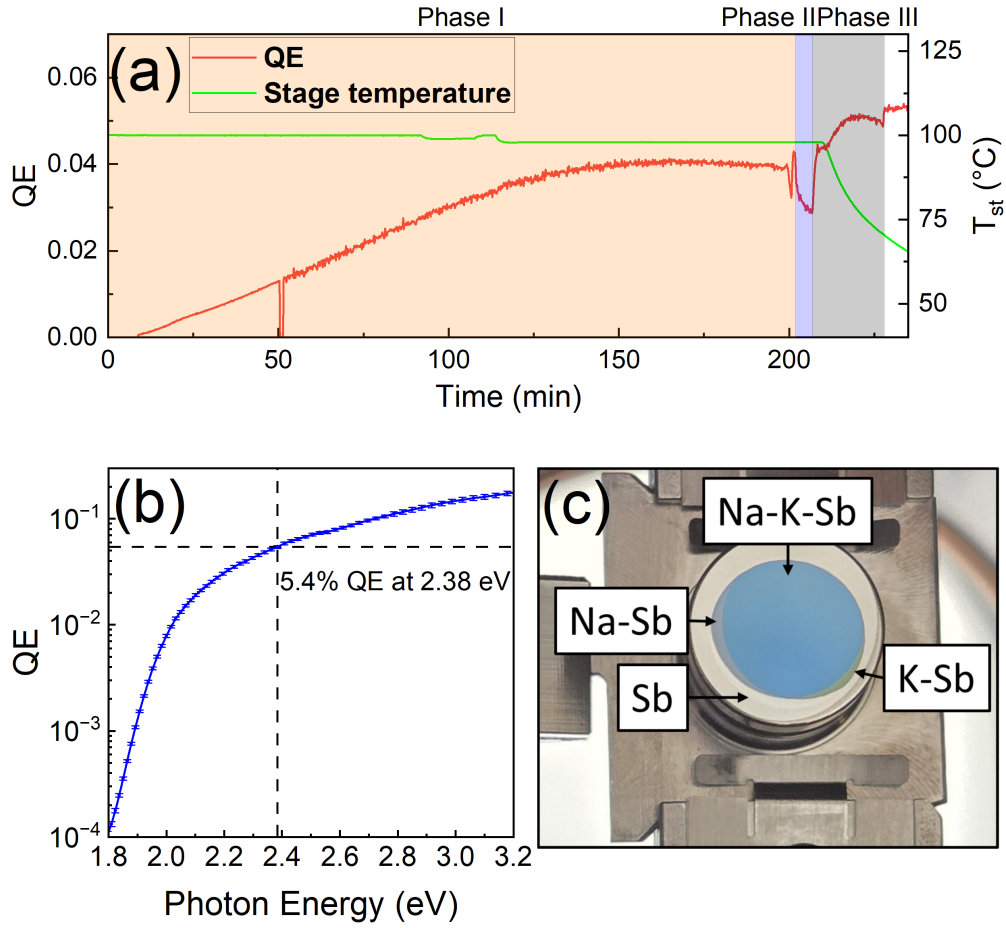


Figure 5.2: *The photocathode SEA03 prepared for the commissioning of SEALab: (a) QE (at 520 nm) and stage temperature in triple evaporation growth; (b) Spectral response of SEA03 one day after growth; and (c) Image of the SEA03 in photocathode lab in transfer system 1 before transferred into suitcase.*

ment in homogeneity is due to the geometry optimization as described in Section 4.4.3.

Due to the urgent schedule for transfer to the photoinjector, the storage lifetime was monitored for only one night, and XPS characterization was cancelled to avoid QE degradation. The QE was stable over night, with a 1/e storage lifetime exceeding 500 hours.

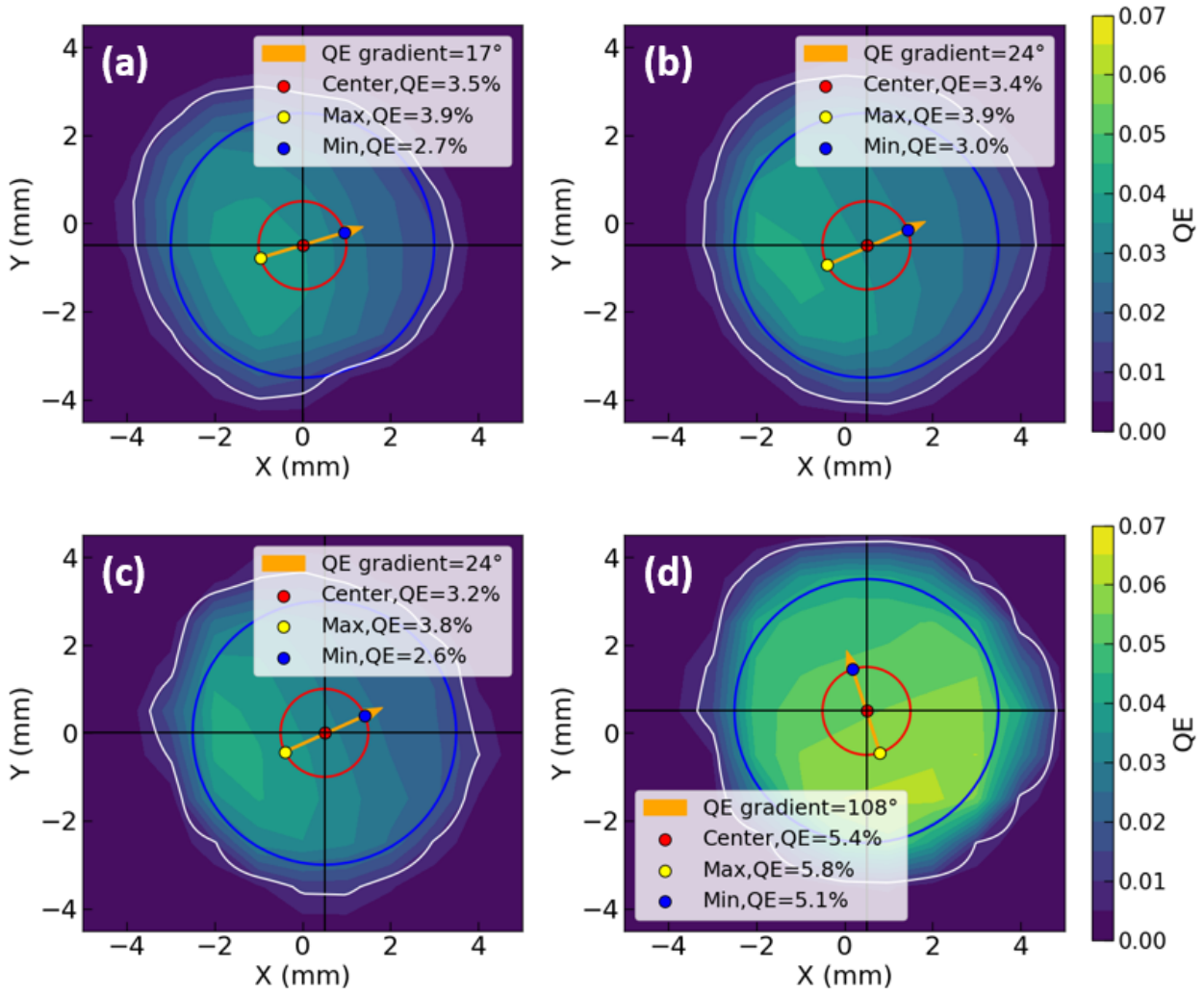


Figure 5.3: *QE maps of Na_2KSb photocathodes prepared on real-Mo plug for SEALab, measured at 520 nm in preparation chamber: (a) SEA00, (b) SEA01, (c) SEA02 and (d) SEA03.*

5.2.2. Transfer to SEALab

The transfer of the photocathode from the photocathode lab to the SEALab photoinjector involved several steps. The photocathode is first transferred via transfer system 1 to a compact UHV vacuum suitcase. During the transfer, which lasted approximately 30 minutes, the base pressure increase to low $10^{-9}\,\mathrm{mbar}$ due to residual degassing from the moving transfer arm of duration of about half an hour. Experimental verification of SEA00 confirmed that this transient pressure rise does not cause instant measurable degradation of the QE of Na_2KSb photocathodes.

The UHV suitcase itself is pumped by a combination of a non evaporable getter (NEG) and an ion pump (IGP), achieving a base pressure of 2×10^{-11} mbar. This suitcase is designed for safe transport between transfer system 1 at the photocathode lab and transfer system 2 at the SEALab facility.[77]

Under ideal conditions, the entire transfer process can be completed within four days. However, an incident occurred during the transfer from the UHV suitcase to transfer system 2: a limit screw in the pincer loosened when picking up the sample, requiring the system to be vented, repaired, pumped down, and baked out. Consequently, the photocathode (SEA03) was inserted into the cold section of the photoinjector 14 days post-growth. The pressure profile throughout the transfer is shown in Figure 5.4. The base pressure in transfer system 2 before transfer was approximately 4×10^{-10} mbar, a great improvement over previous transfers of SEA02. The transfer from the suitcase into transfer system 2 is particularly challenging, requiring approximately 7 hours due to issues with the pincer mechanism. The subsequent transfer from system 2 into the main gun chamber was completed in about 1 hour, causing a pressure increase to several 10^{-9} mbar in the main chamber. Following the transfer, the photocathode was cooled from room temperature to 80 K, during which the gun pressure stabilized in the low 10^{-10} mbar range.

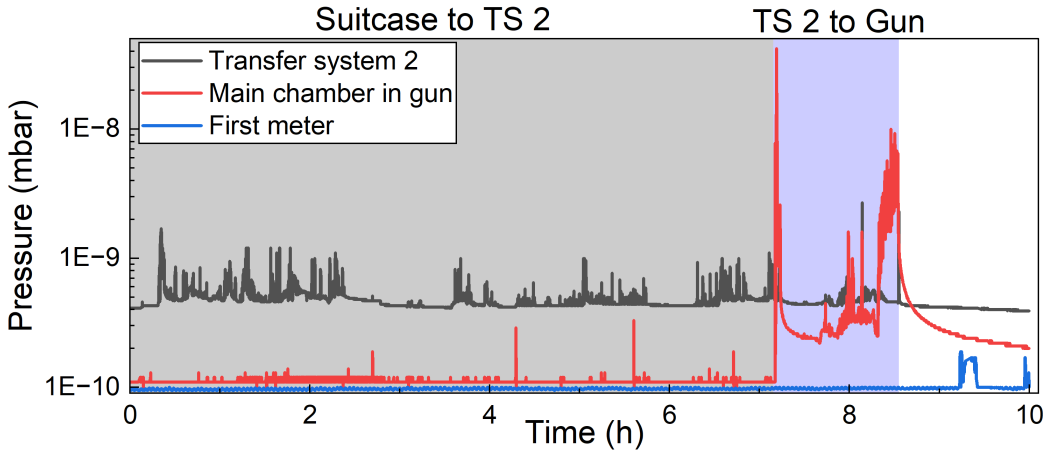


Figure 5.4: *Pressure change during the transfer of photocathode SEA03 from the UHV suitcase into the SRF gun via transfer system 2 at SEALab.*

5.2.3. Performance in SEALab

After transfer to the back wall of the cavity in the main chamber in gun, the QE is measured by the drain current with a constant applied voltage of $5000\,\mathrm{V}$, without applying RF-field to the cavity. This measurement was conducted by Jonas and Guido in the HBB team. The drive laser (521 nm, 1 MHz repetition rate, 4 ps bunch length, 1 mW power, 1 mm spot diameter) was used for QE mapping via motorized mirrors. Figure 5.5a shows the laser positioned at the edge of the plug for alignment purposes.

As shown in Figure 5.5b, the QE map is directly measured on 17 July 2025, revealed a center QE of 0.42%, approximately one order of magnitude lower than that after growth. This degradation is attributed mainly to surface oxidation during transfer. In beam commissioning on 21 July 2025, as shown in Figure 5.5c, a focused electron beam was successfully observed on the viewscreen in the diagnostic beamline with a cavity gradient of 4 MV/m.

Despite the premature termination of the experiment, the operational data confirmed a significant performance improvement of the SEA03 photocathode over previous attempts. It maintained a functional QE of $\sim$0.4% post-transfer and demonstrated robustness against operational incidents such as field emission and electron back-bombardment. This enhanced performance is attributed to two critical advancements: (1) The optimized triple evaporation (Tri-2) recipe produced a film with a more homogeneous and stoichiometric Na_2KSb phase by suppressing Na surface enrichment and the formation of low-QE secondary phases (e.g., NaK_2Sb), thereby improving the compromise between initial QE and operational stability. (2) Optimizations to the cathode transfer chain, including more thorough baking of transfer system 2, achieved a superior vacuum, which significantly reduced oxidation during transfer.

While shortcomings remain, these results provide a foundation for continued optimization of growth recipes and transfer process to achieve photocathodes with higher QE and robustness for future commissioning and operations.

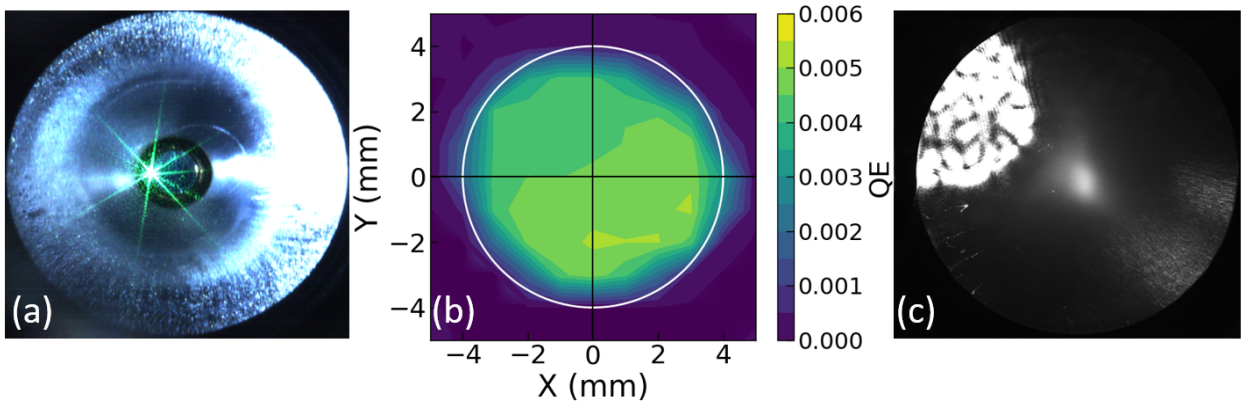


Figure 5.5: *(a) The photocathode aligned in the center of the back wall of the gun cavity with the photocathode laser at the edge of the cathode plug. (b) The QE map of the SEA03 photocathode measured in SEALab directly after cathode transfer with $QE_{center} = 0.42\%$, via the drain current at 5 kV DC bias and with photocathode laser (521 nm, 1 mm spot diameter); (c) Focused electron beam on viewscreen (FOM) in diagnostic beam line with a cavity gradient of 4 MV/m.*

6. XPS

This chapter presents a systematic XPS analysis of Sb layers, Na-Sb and K-Sb binary systems, and the Na-K-Sb ternary system. The main focus of this research is on the Na-K-Sb ternary system, establishing a comprehensive database of core level peak shifts, energy separations, and Auger parameters. Data for relevant alkali metal oxides are also included.

All measurements were conducted following the procedures detailed in Section 3.4. Spectra were processed using CasaXPS software. For both Al Kα and Mg Kα spectra, the Sb, K, and Na peaks were fitted with a line shape of 80% Lorentzian and 20% Gaussian protocol. The Sb 3d and K 2p peaks exhibit spin-orbit splitting, and the doublets were separated by 9.4 eV and 2.8 eV, respectively.[58,67] The intensity of the Sb $3d_{3/2}$ peak was constrained to two-thirds that of the Sb $3d_{5/2}$ peak, and the K $2p_{1/2}$ peak was constrained to half the intensity of the K $2p_{3/2}$ peak. Shirley background was subtracted from all spectra.[78]

6.1. Pure Metallic Antimony

A reference layer of pure metallic antimony was deposited via thermal cracker cell at a rate of 0.15 Å/s for 30 minutes with the substrate held at 70 °C. The corresponding XPS spectra are shown in Figure 6.1.

Figure 6.1a displays the survey scan. The spectrum confirms the presence of Sb core levels (3s, 3p, 3d, 4d) and the Sb MNN Auger peak series. The Sb 3d doublet exhibits the highest intensity and was therefore selected for detailed region scans in subsequent studies. Minor satellite peaks are attributed to plasmon loss features from photoelectron scattering. The absence of carbon (C 1s) and oxygen (O 1s) contaminants confirms the cleanliness of the UHV environment and the Sb evaporation source, a prerequisite for synthesizing high quality Na-K-Sb films.

Peak fitting is applied to the Sb 3d region scan in Figure 6.1b, the Sb $3d_{5/2}$ and

Sb $3d_{3/2}$ peaks are located at 528.2 eV and 537.6 eV, respectively, with a spin-orbit splitting of 9.4 eV and an intensity ratio consistent with the theoretical 3:2 value. The Sb $3d_{5/2}$ binding energy aligns well with literature values for metallic Sb, which range from 528.1 eV[60,79], 528.2 eV[80] to 528.3 eV[67], while the amorphous Sb layers typically exhibit a slightly higher value near 529.3 eV[81].

The full width half maximum (FWHM) of the Sb 3d peaks is approximately 1.3 eV, broader than the 0.8 eV reported using monochromatic X-ray sources,[82] a consequence of the non-monochromatic source. The peak fitting is satisfied overall, though a slight asymmetry on the high-binding-energy side of the Sb $3d_{5/2}$ peak is observed, a feature also reported in earlier studies.[83]

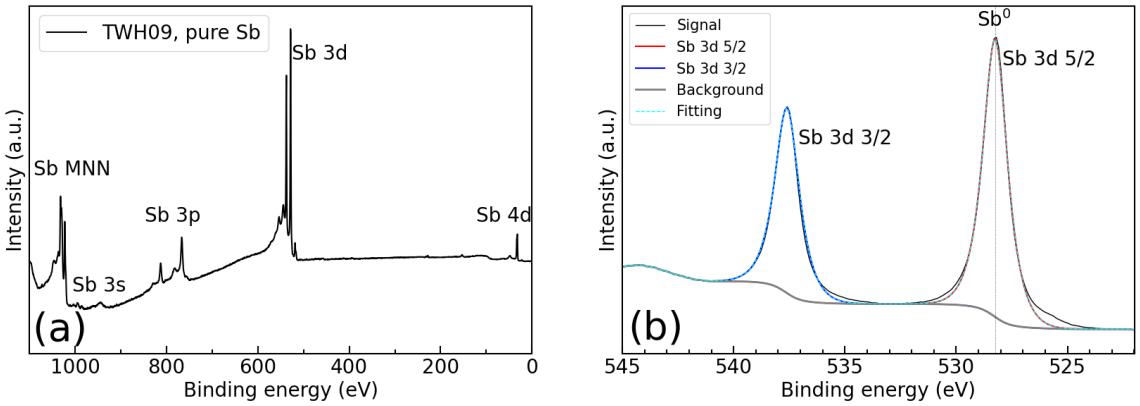


Figure 6.1: *XPS spectra of a pure Sb layer acquired with Al Kα: (a) survey scan and (b) high-resolution Sb 3d region scan with peak fitting.*

6.2. K-Sb System

K-Sb phases are studied as intermediates in the sequential growth of both Na-K-Sb and Cs-K-Sb photocathodes, as discussed in Section 2.4.1.1. Films with mixed K-Sb phases, such as samples P07 and WH15, typically exhibit a QE of 0.1–0.3% at 520 nm.

This section presents the XPS characterization of four K-Sb films with increased K/Sb ratio, including two samples (P06, P07) from Martin's dissertation[46] and two newly prepared samples (WH04, TWH23). Stoichiometries were cal-

culated from survey scans (P06, P07) and high-resolution region scans (WH04, TWH23) of the K 2p (288–309 eV) and Sb 3d (521–548 eV) regions, acquired with a 10 eV pass energy.

Figure 6.3a shows a survey scan of the P07 ($K_{2.7}Sb$) film, confirming the presence of Sb and K core level peaks. The region scan of Sb d region is shown in Figure 6.3b, and the spin orbit splitting between $3d_{5/2}$ and Sb $3d_{3/2}$ peak is 9.4 eV with the intensity ratio close to 3:2.

High-resolution Sb 3d spectra for all four films are shown in Figure 6.2a. The binding energies of Sb^0, Sb^-, Sb^{3-} states are annotated at 528.2 eV, 527.5 eV, and 526.3 eV, respectively.[60,84] As the K/Sb ratio increases, the spectra systematically shift to lower binding energies with the successive appearance of Sb^0, Sb^-, Sb^{3-} peaks. The increased FWHM in WH04 (1.7 eV), P06 (2.5 eV), and P07 (1.7 eV) compared to pure Sb (1.3 eV) indicates the coexistence of multiple phases. WH04 likely contains metallic Sb and KSb, while P06 is a mixture of metallic Sb, KSb and K_3Sb. In P07, the metallic Sb component vanishes, and the phase ratio is approximately 35% KSb to 65% K_3Sb. For the K-saturated sample TWH23 (7nm Sb+70nm K at 90°C substrate temperature), the FWHM narrows to 1.3 eV, indicating a single phase of K_3Sb. A 0.3 eV positive binding energy shift suggests a transition to a n-type hexagonal K_3Sb structure, while no QE ($< 0.1\%$) was detected in this sample. These observations are consistent with XRD results[26,27]- cubic K_3Sb (p-type, high QE phase) transfer to a more stable hexagonal structure (n-type, low QE) with excess K deposition. In addition, an O 1s peak is detectable in K-rich samples (P07, TWH23), indicating slight surface oxidation.

The K 2p region scans (Figure 6.2b) show a K $2p_{3/2}$ peak at 293.7 eV (FWHM of 1.3 eV) in K-deficient samples (WH04, P06). In P07, the peak broadens to 1.7 eV and shifts to 293.4 eV, consistent with reported values for $K_{2.4}Sb$.[60] This broadening suggests a mixed-phase region of cubic and hexagonal K_3Sb. While, the FWHM narrows again to 1.3 eV in TWH23, indicating single-phase hexagonal K_3Sb.

To mitigate surface band bending effects, the binding energy separation between the K $2p_{3/2}$ and Sb $3d_{5/2}$ peaks was calculated.[85] As shown in Figure 6.2c, this separation increases from –234.2 eV for KSb to –232.9 eV for hexagonal K_3Sb, reflecting enhanced charge transfer from K to Sb with increasing K content. The value for the high-QE cubic K_3Sb phase likely lies slightly above that for hexagonal K_3Sb, though its precise position remains unknown due to challenges in synthesizing the pure cubic phase K_3Sb films, and please refer to Section A.1.4 for more study on this topic.

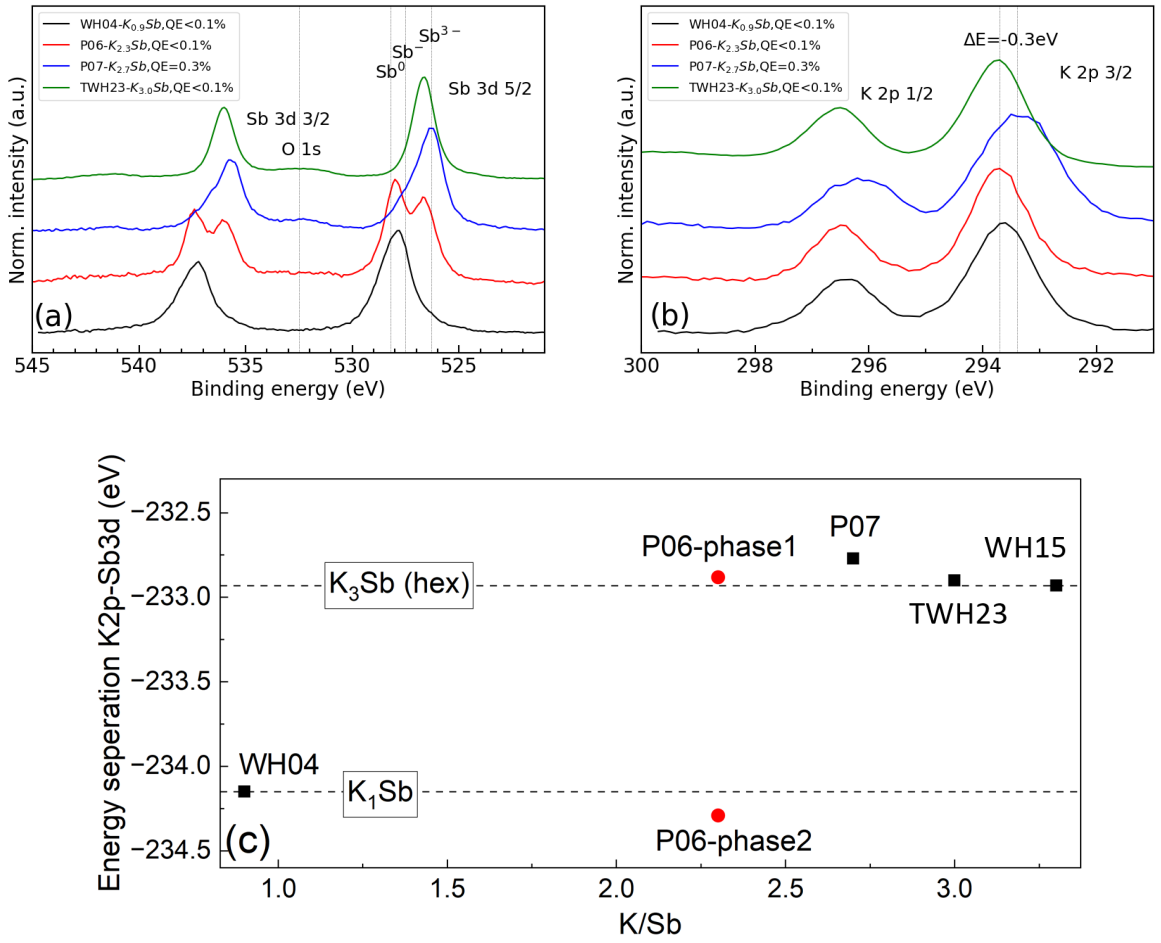


Figure 6.2: *Al Kα XPS region scan of four K-Sb films with increased K to Sb ratio: (a) Sb 3d region scan, (b) K 2p region scan and (c) binding energy separation between Sb $3d_{5/2}$ and K $2p_{3/2}$.*

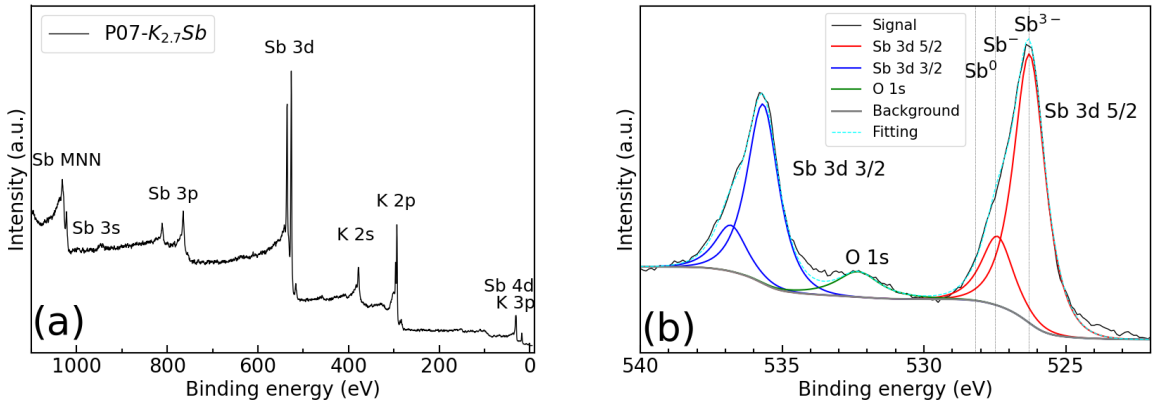


Figure 6.3: *XPS spectra of a $K_{2.7}Sb$ film (P07) with Al Kα: (a) survey scan and (b) high-resolution Sb 3d region scan with peak fitting.*

6.3. Na-Sb System

As discussed in Section 4.1.4, Na-Sb phases may exists as by-products in Na-saturated Na-K-Sb films due to the low equilibrium vapor pressure of Na, often degrading photocathode performance. This section establishes a reference XPS database by characterizing a Na_3Sb film.

The film was synthesized by co-depositing Na and Sb at a substrate temperature of 110 °C for two hours (Sb rate: 0.01 Å/s, Sb thickness: 5.4 nm). The resulting Na_3Sb thickness was estimated to be 21 nm, based on a 3.9 times volume expansion from metallic Sb. The sample was subsequently held at 70 °C for 12 hours to evaporate the excess Na, which may exist on the surface.

The XPS spectra, acquired with Mg Kα to avoid overlap between the Na KL_1L_{23} Auger peak and the O 1s signal, are shown in Figure 6.4. The calculated stoichiometry was $Na_{3.3}Sb$, with the slight Na excess potentially due to the surface adsorbed Na or calculation uncertainty, since the characterization depth is 9.15 Å for Na 1s and 24.1 Å for Sb 3d in Mg Kα. As shown in Figure 6.4a, the Na 1s peak is located at 1071.7 eV with FWHM of 1.3 eV.

As shown in Figure 6.4b, peak fitting of the Sb 3d region reveals contributions

from Na_3Sb and a Na-deficient phase (e.g., NaSb), with Sb $3d_{5/2}$ peaks fitted at 526.8 eV and 527.9 eV, respectively.

The positive binding energy shift of Na_3Sb relative to K_3Sb can be attributed to its n-type character, which induces upwards surface band bending that shifts core levels to higher binding energies. Free from this effect, the binding energy separation between the Na 1s and Sb $3d_{5/2}$ peaks was calculated. This separation increases from 543.9 eV for NaSb to 544.9 eV for Na_3Sb, confirming a greater charge transfer from Na to Sb in the more Na-rich compound.[85]

The Sb 3d doublet maintains the expected 9.4 eV spin-orbit splitting. However, the intensity ratio of the $3d_{5/2}$ to $3d_{3/2}$ peaks is consistently 5–10% higher than the theoretical 3:2 value. This deviation is observed only in Na-containing films (Na-Sb and Na-K-Sb). The effect is unrelated to Na Auger peaks or the presence of oxides, as it persists when using different X-ray sources and the O 1s peak for Na oxides does not appear in such high binding energy (∼536 eV). The physical origin of this deviation remains unclear.

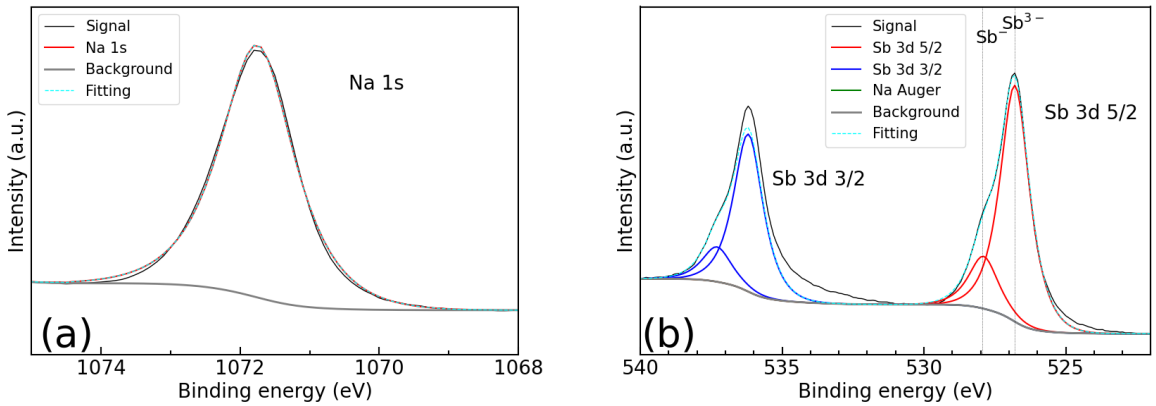


Figure 6.4: *Mg kα XPS spectra of a Na-Sb film, the stoichiometry is calculated to be $Na_{3.3}Sb$: (a) Na 1s region scan, (b) Sb 3d region scan.*

6.4. Na-K-Sb System

This section presents a detailed XPS study of the $Na_xK_{3-x}Sb$ ternary system. As outlined in Section 2.4.1, the $Na_xK_{3-x}Sb$ system can be divided into six phase zones as a function of K_3Sb content. Our focus here is on the single-phase $(Na,K)_2KSb$ zone and the two adjacent dual-phase zones.

6.4.1. Phase Transformation from Na_2KSb to NaK_2Sb

As discussed in Section 4.5.1, the QE peaks for K/Sb ratios between 0.90 and 1.25, suggesting that Na_2KSb is the primary photoemissive phase, while NaK_2Sb is not.

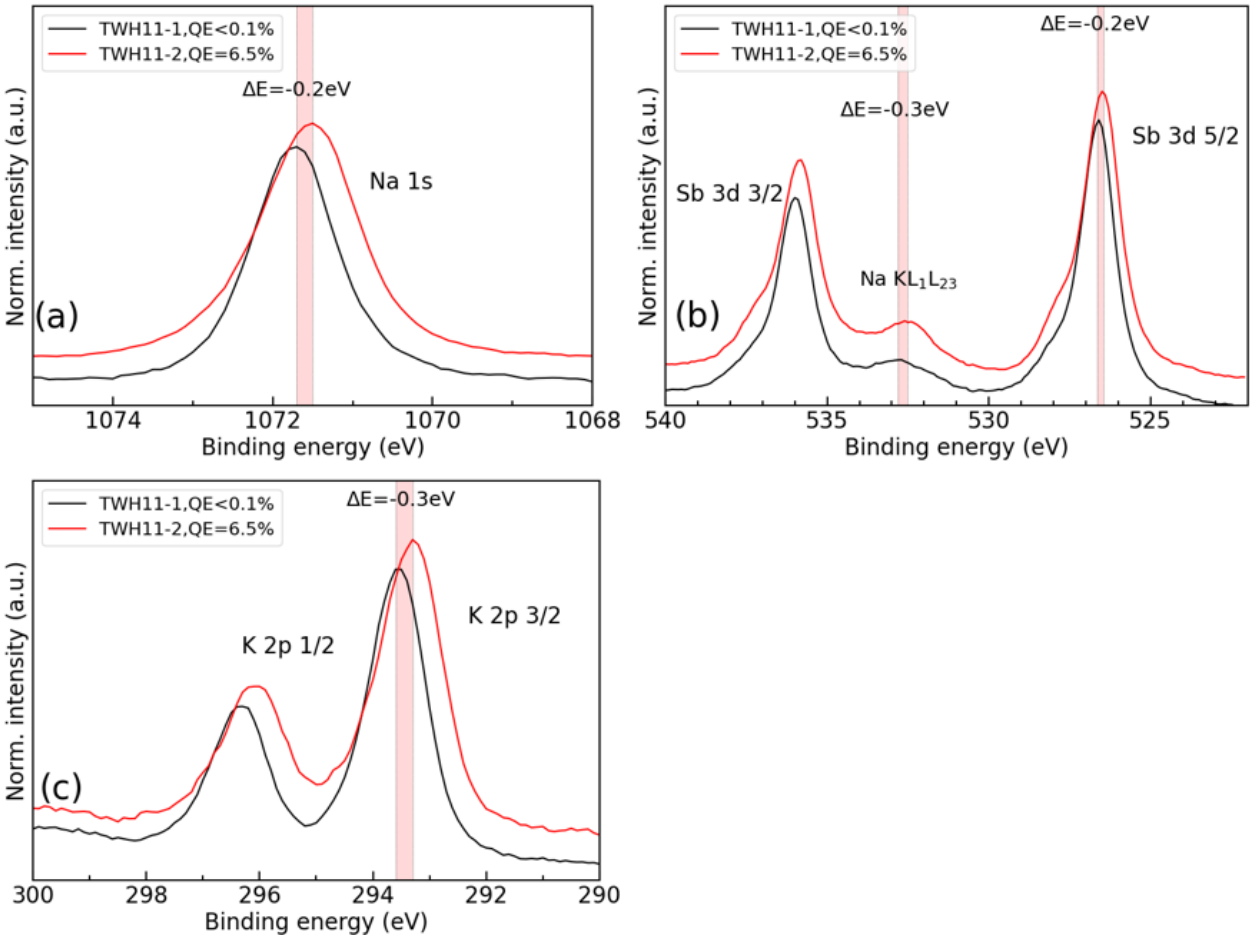


Figure 6.5: *Al Kα XPS spectra of TWH11-1 ($Na_{1.2}K_{2.0}Sb$) and TWH11-2 ($Na_{2.0}K_{1.0}Sb$) photocathodes. (a) Na 1s region scan, (b) Sb 3d region scan and (c) K 2p region scan.*

To investigate this, we synthesized a $Na_{1.2}K_{2.0}Sb$ film (TWH11-1) via sequential deposition, which exhibited no photocurrent (QE<0.1% at 520 nm) at room temperature. Subsequent deposition of additional Na at an elevated substrate temperature of 170 °C converted the film to $Na_{2.0}K_{1.0}Sb$ (TWH11-2), yielding a QE of 6.5% after cooling down.

A comparison of the background-subtracted and normalized XPS spectra for both samples is shown in Figure 6.5. A consistent shift of 0.2–0.3 eV to lower binding energy is observed for all core levels—Na 1s, Sb 3d, K 2p, as well as Auger peak Na KL_1L_{23}—upon conversion to the high-QE Na_2KSb phase. This systematic shift indicates a transition from an n-type (hexagonal NaK_2Sb) to a p-type (cubic Na_2KSb) semiconductor. The similar trend is also observed in sample TWH24 as shown in Section A.1.2.

6.4.2. Phase Transformation from Na_2KSb to Na_3Sb

To study the surface phase transformation to Na-rich compositions, stepwise Na deposition was performed on sample TWH19, transitioning it from $Na_{2.0}K_{1.2}Sb$ to $Na_{3.1}K_{0.4}Sb$. The normalized, background-subtracted XPS spectra (Al Kα and Mg Kα) for the TWH19 series are shown in Figure 6.6.

A concurrent positive shift of 0.2–0.3 eV is observed for the Na 1s, Na KL_1L_{23} and Sb 3d peaks in Figure 6.6, with the Sb $3d_{5/2}$ peak moving from 526.5 eV (TWH19+Na) to 526.7 eV (TWH19+4Na). These shifts are consistent with a partial surface transformation from p-type Na_2KSb to n-type Na_3Sb. While, the initial TWH19 spectrum is also slightly positive shifted relative to TWH19+Na, likely due to the presence of n-type NaK_2Sb.

The O 1s peak area shows a slight increase for the last two samples (TWH19+3Na, TWH19+4Na) at 532.8 eV, as indicated in the subplot of Figure 6.6e. However, it is difficult to determine the type of the oxides due to the low peak intensity and numerous possible candidates.

In contrast to other elements, the K $2p_{3/2}$ peak shifts to a lower binding energy,

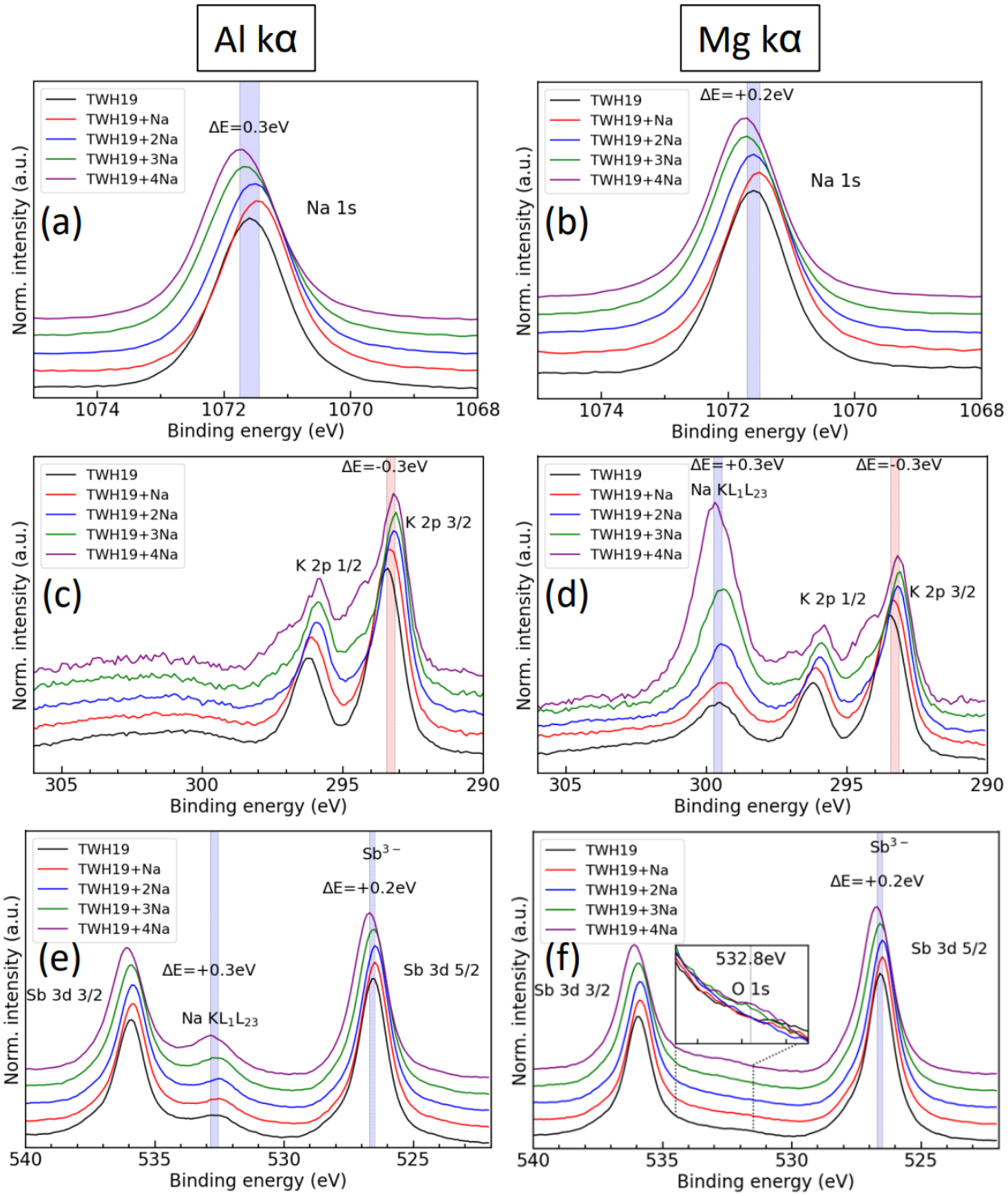


Figure 6.6: *XPS spectra of TWH19 series Na_2KSb photocathodes. (a), (c) and (e) are the region scans of Na 1s, Sb 3d and K 2p by Alkα. (b), (d) and (f) are the region scans of Na 1s, Sb 3d and K 2p by Mgkα.*

from 293.5 eV (TWH19) to 293.2 eV (TWH19+4Na), as shown in Figure 6.6c and f. This trend is opposite to that expected from a simple n-type to p-type transition, which will be further investigated in Section 6.4.3.

K deficiency in the surface layer helps the detection of K oxides by reducing the signal from the bulk Na-K-Sb phase. And the peak fitting of the K 2p region for TWH19+3Na and TWH19+4Na reveals a secondary component at 294.4 eV, which is attributed to K–O species.[86,87] As summarized in Table 6.1, the K oxidation level—defined as the ratio of the K–O peak area to the total K $2p_{3/2}$ area—increases with successive deposition, likely due to prolonged exposure to residual gases during deposition or the XPS measurement. The K-O contribution is more pronounced in the more surface-sensitive Mg Kα spectra than in the Al Kα spectra, confirming that oxidation is a surface phenomenon rather than bulk. In contrast, a parallel analysis for Na oxides is not feasible, as the high mobility of Na prevents the formation of a Na-deficient surface necessary for quantifying Na–O species in slightly oxidized films. In Section 6.5.2 more oxidized Na-K-Sb samples will be analyzed in detail.

Table 6.1: *Summary of peak fitting results and oxidation level in K 2p region scan for TWH19+3Na and TWH19+4Na.*

Sample	X-ray source	K $2p_{3/2}$ peak area (cps*eV)		K oxidation level
		K-O	Na-K-Sb	
TWH19+3Na	Al Kα	80	415	16%
TWH19+3Na	Mg Kα	117	410	22%
TWH19+4Na	Al Kα	100	259	28%
TWH19+4Na	Mg Kα	129	276	32%

6.4.3. Core Level Peak Shifts

To establish a comprehensive overview of core-level binding energy shifts in the Na-K-Sb system, we analyzed the Na 1s, K $2p_{3/2}$, and Sb $3d_{5/2}$ peak positions from 21 photocathode samples across the stoichiometric range from Na_3Sb

to NaK_2Sb, as shown in Figure 6.7. Peak shifts are calculated relative to the metallic phases of Na (1071.8 eV), K (294.4 eV), and Sb (528.2 eV),[58,88] with an estimated uncertainty of ±0.05 eV. Alkali-deficient samples (TWH10, TWH20) were excluded to ensure statistical accuracy.

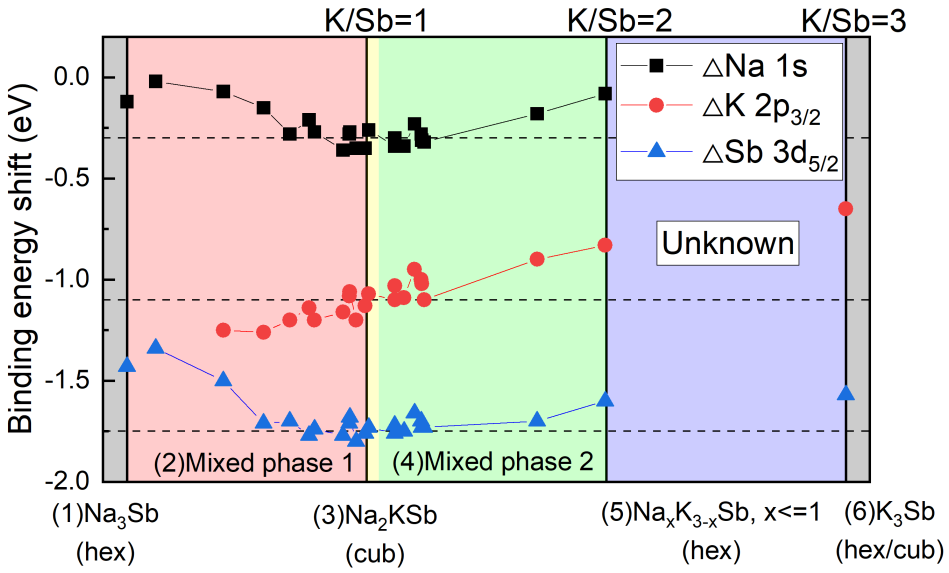


Figure 6.7: *Na 1s, K $2p_{3/2}$ and Sb $3d_{5/2}$ core level peak shifts of $Na_{3-x}K_xSb$ photocathode films, present as a function of K/Sb ratio. From left to right listed: Na_3Sb, TWH19+4Na, TWH19+3Na, TWH13, TWH19+2Na, TWH22, TWH21, TWH25, TWH14, TWH18, TWH11-2, SEA00, TWH19+Na, TWH15, TWH19, TP01, TWH16, TWH17, TWH12, TWH11-1, TWH23(Hex-K_3Sb).*

The Na 1s and Sb $3d_{5/2}$ peaks exhibit similar behavior, shifting by +0.2 eV upon transitioning from the Na_2KSb phase to NaK_2Sb, and by +0.3 eV upon transitioning to Na_3Sb. These positive shifts are likely caused by surface band bending with a change from a p-type (Na_2KSb) to a n-type (NaK_2Sb, Na_3Sb) semiconductor.

In contrast, the K $2p_{3/2}$ peak shows a significant and gradual negative shift of approximately -0.3 eV across the compositional range from the NaK_2Sb to Na_2KSb. For the Na_2KSb phase, the K $2p_{3/2}$ binding energy is around 293.3 eV, similar to the value reported for p-type Cs-K-Sb phases (293.2 eV).[60] A slight

further decrease of 0.1 eV is observed in zone 2, despite the only K contained phase in both zones 2 and 3 is the Na_2KSb phase. This minor difference may arise from systematic errors in stoichiometry calculation or inhomogeneity within the film.

To mitigate effects from energy referencing and surface band bending, I examined the Auger parameter and core-level energy separations, which are shown in Figure 6.8 as a function of K/Sb ratio.

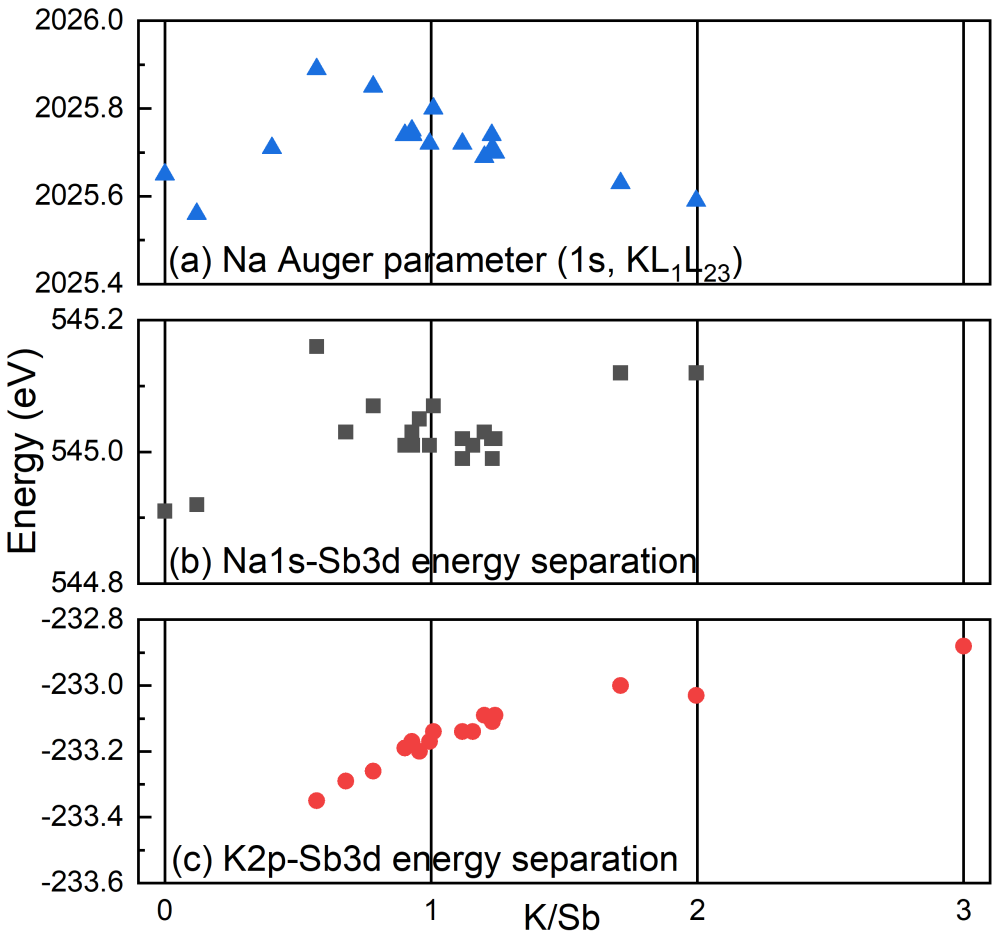


Figure 6.8: *Na Auger parameter (1s, KL_1L_{23}), and core level binding energy separation between K $2p_{3/2}$ and Sb $3d_{5/2}$, Na 1s and Sb $3d_{5/2}$ in $Na_{3-x}K_xSb$ photocathodes.*

The energy separation between Na 1s and Sb $3d_{5/2}$ increases with the K/Sb ratio from Na_3Sb to NaK_2Sb, with one exception. Similarly, the K $2p_{3/2}$-Sb $3d_{5/2}$

separation increases from NaK_2Sb to K_3Sb. These trends can be qualitatively explained by a larger effective charge transfer from K to Sb compared to Na, consistent with the larger electronegativity difference between K and Sb than Na and Sb.

However, this simplified charge-transfer model fails to explain the behavior of the Na Auger parameter, which peaks at 2025.9 eV at K/Sb=0.6—approximately 0.3 eV higher than the values for Na_3Sb or NaK_2Sb, a trend also noted in the NIST database.[88] A complete interpretation of this non-monotonic behavior likely requires more refined models, which can account for localized electron configurations and final-state effects.

6.5. Thermal Dissociation and Oxidation of Na2KSb Photocathodes

This section presents a systematic investigation into two primary mechanisms responsible for QE degradation in Na_2KSb photocathodes: thermal dissociation and surface oxidation. Understanding these failure modes is critical for improving photocathode transfer process and operational stability.

6.5.1. Thermal Dissociation

This section presents an XPS analysis of the effect of thermal load on the surface composition of Na_2KSb photocathodes. As introduced in Section 2.4, a principal advantage of Na-K-Sb photocathodes over Cs-K-Sb is their superior thermal stability, a property critical for applications involving significant thermal load, such as normal-conducting radio frequency (NCRF) guns. While the primary application within this thesis is the SEALab superconducting RF (SRF) photoinjector, which provides sufficient cooling as discussed in Section 2.1. Understanding thermal degradation remains essential for characterizing the material's fundamental properties.

Following the XPS analysis in Sec. Section 4.2.2.1, the thermal stability of photocathodes TWH14-TWH17 was investigated. The QE of these samples had degraded to between 1.5% and 2.0% after the initial XPS measurement. The sam-

ples were subsequently following a step-wise heating protocol, with temperatures held at 70 °C, 90 °C, 110 °C, and finally 130 °C for two hours at each step.

The QE evolution during heating, shown in Figure 6.9, reveals distinct behaviors. Samples TWH14 and TWH15, which have stoichiometries closest to the ideal Na_2KSb composition, remained relatively stable until a rapid QE decay occurred at 130 °C. In contrast, TWH16 and TWH17 exhibited more complex degradation profiles, potentially due to the dissociation of less thermally stable phases such as NaK_2Sb within the film.

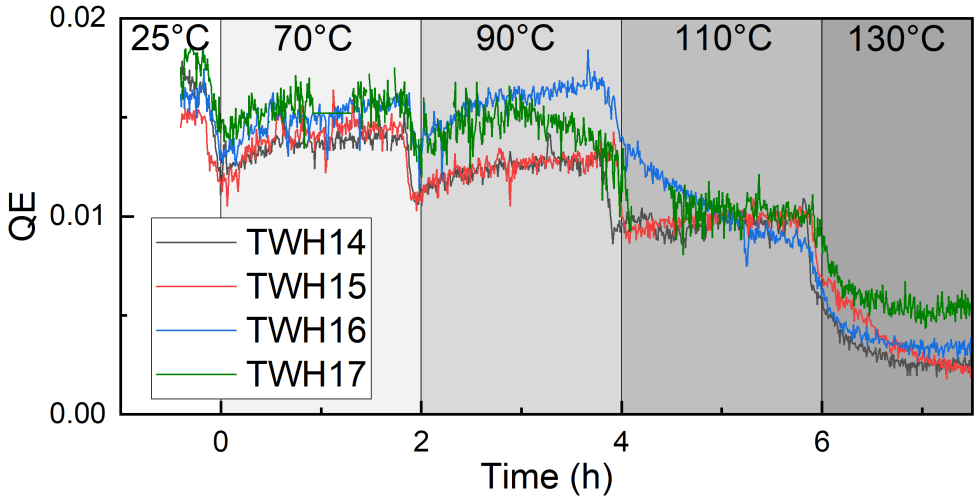


Figure 6.9: *Thermal stability experiment of the four Na_2KSb photocathodes. The samples were step-wise heating to a sample temperature of 70°C, 90°C, 110°C, and 130°C, with 2 hours step.*

Here the XPS spectra before and after the thermal test of TWH15 is analyzed in detail, due to its stoichiometric close to ideal Na_2KSb. The full dataset and supplementary experiments are provided in Appendix Section A.2.1.

The background-subtracted spectra of Na 1s, Sb 3d, and K 2p are shown in Figure 6.10. All three spectra exhibit significant changes after thermal testing. The calculated stoichiometry changed from $Na_{2.2}K_{1.2}Sb_{1.0}$ to $Na_{2.6}K_{0.8}Sb_{1.0}$. This trend is visually apparent in the Na 1s and K 2p spectra, where the Na 1s peak intensity increased by 33% and the K $2p_{3/2}$ intensity decreased by 27%, as sum-

Table 6.2: *Summary of peak fitting results of Na_2KSb photocathode before (TWH15) and after (TWH15T) thermal dissociation test, including binding energy (BE) in eV, peak width (FWHM) in eV and peak intensity (I) in cps*eV.*

Sample	Sb $3d_{5/2}$		K $2p_{3/2}$	Na 1s	
	Primary peak BE/FWHM/I	Secondary peak BE/FWHM/I	Primary peak BE/FWHM/I	Primary peak BE/FWHM/I	Secondary peak BE/FWHM/I
TWH15	526.4/1.3/4207	528.0/1.3/239	293.3/1.3/908	1071.5/1.3/4918	-/-/-
TWH15T	526.4/1.3/3685	527.8/1.3/1062	293.3/1.3/666	1071.6/1.3/5067	1072.2/1.3/1450

marized in the peak fitting results in Table 6.2.

The total intensity of the Sb $3d_{5/2}$ peak increased slightly by 6%. Furthermore, a secondary peak attributed to Sb^- appeared at 527.8 eV, accounting for 22% of the total Sb $3d_{5/2}$ intensity. A corresponding secondary peak is also observed in the Na 1s spectrum. The energy separation between Na 1s and Sb $3d_{5/2}$ in this "secondary phase" is 544.4 eV, which lies between the values for Na_3Sb (544.9 eV) and NaSb (534.9 eV), as discussed in Section 6.3. This indicates a mixture of the two phases. This result aligns with previous research on the thermal dissociation of Na_2KSb,[38] which concludes that dissociation begins with K loss and a phase transformation to Na_3Sb and NaSb, as these phases have higher dissociation energies than Na_2KSb.

6.5.2. Oxidation

As detailed in Section 5.2, the QE of the SEA03 Na_2KSb photocathode degraded from 5% to 0.4% after transfer from the preparation lab to the SEALab photoinjector. This significant QE loss is attributed to surface oxidation resulting from several vacuum incidents during the transfer procedure. To understand the chemical processes underlying this degradation, we conducted an XPS study on the effect of residual gases—H_2O and O_2—on the surface composition of Na_2KSb. The analysis compares samples exhibiting progressively higher oxidation levels, quantified by the O 1s/Sb 3d peak area ratio. It should be noted that this study

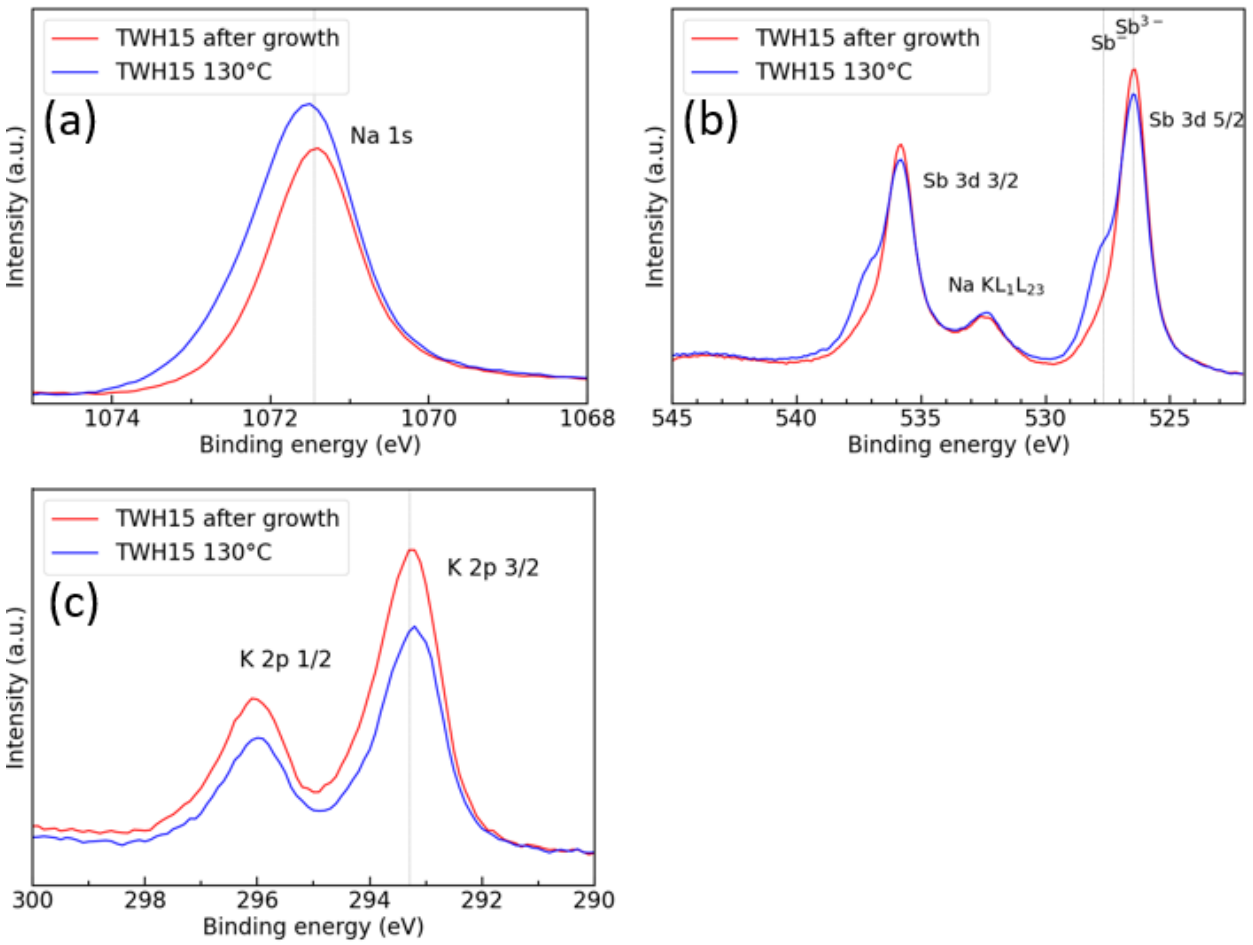


Figure 6.10: *Al Kα XPS region scans of TWH15 before and after the thermal dissociation test.*

examines naturally occurring oxidation under complex vacuum conditions, while a controlled study involving single component of residual gases with controllable partial pressures is not included in this study.

The Mg Kα XPS spectra of the Na 1s, Sb 3d, and K 2p region scans of four photocathodes are presented in Figure 6.11. Spectra were fitted with constraints: the FWHM for Na 1s, Sb 3d, and K 2p peaks was set to 1.25 eV (based on sample TWH16), except for the oxidized Na 1s component, which was set to 1.50 eV (based on spectrum c1). The Sb^{3-} peak position served as an internal energy reference for minor to moderately oxidized samples. For the heavily oxidized sample (d2), the Sb^{3-} peak was undetectable, and influences from surface charging

or band bending could not be ruled out.

A general positive chemical shift to higher oxidation states is observed across all core levels (Na 1s, Sb 3d, and K 2p) with increasing oxidation. The Na 1s peak shows a clear example, shifting from 1071.5 eV (a1) to 1072.5 eV (a3). The final value corresponds to the reported binding energies for Na_2O (1072.5 eV[89]) or NaOH (1072.6 eV[90]).

The K $2p_{3/2}$ region is more complex, developing components at 293.4 eV, 294.4 eV, and 295.0 eV upon oxidation. The latter two match the range for oxidized K (294.7–294.8 eV) formed upon exposure to 40–45 Langmuirs of oxygen.[86,87] A reduction in plasmon loss features is also noted.

The O 1s peak appears at approximately 532.0 eV in a2, b2, c2 and 532.5 eV in d2, a value consistent with several alkali oxides and hydroxides, including suboxide K_3O (532.1 eV in Cs-K-Sb[91], suboxide Na_2O (529.2 eV[87], 529.6 eV[89]), hydroxide NaOH (532.2 eV[90], 532.7 eV[89]) and peroxide K_2O_2 (532.1 eV[87], 531.3 eV[91]).

In the Sb 3d region, the appearance of Sb^- (527.7 eV) and Sb^0 (528.2 eV) components indicates the decomposition of Na_2KSb caused by the formation of alkali oxides. In the heavily oxidized sample (d2), the appearance of an Sb^{3+} peak suggests catalytic oxidation of Sb in the presence of alkali oxides.[91]

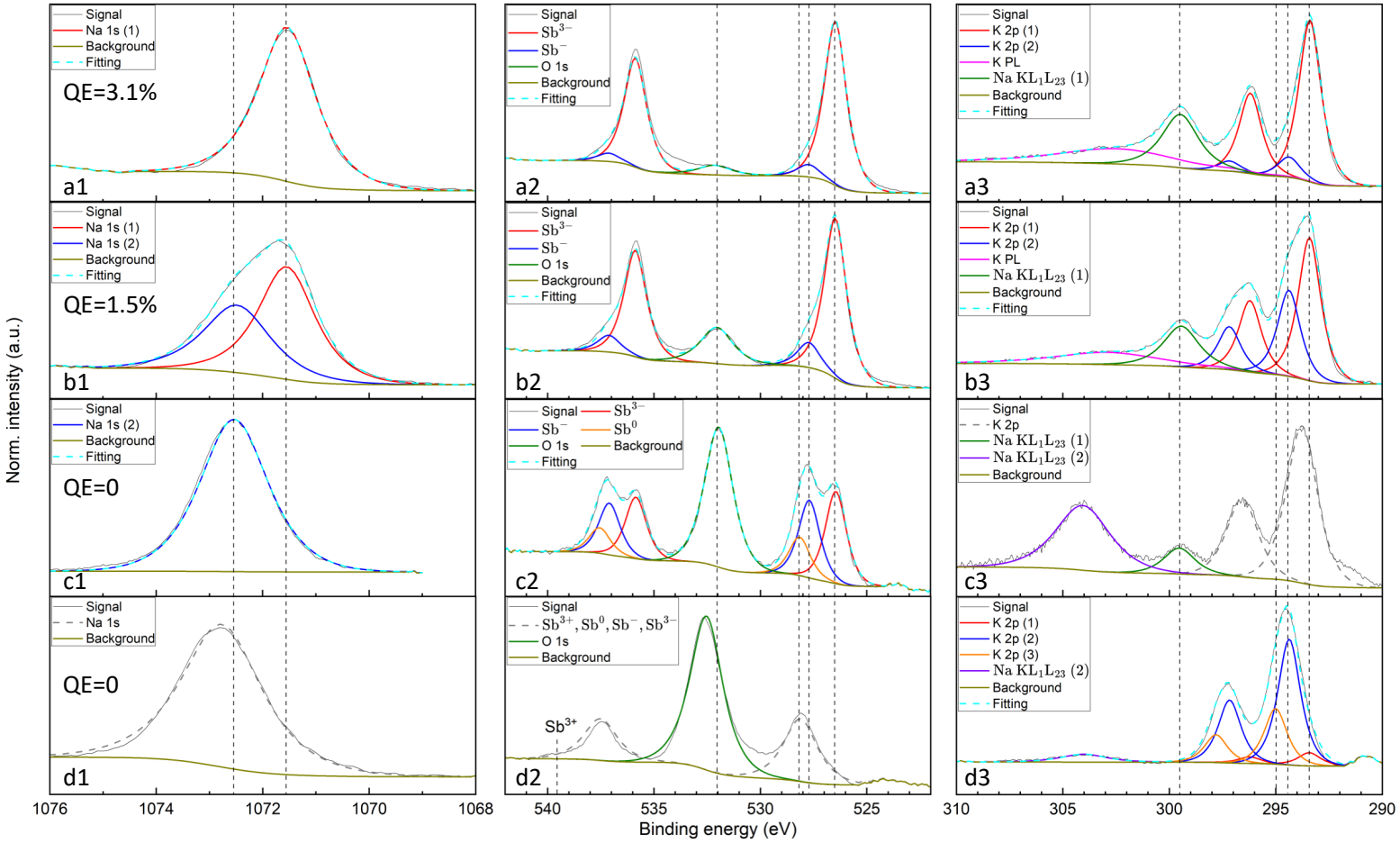


Figure 6.11: *XPS spectra of oxidized Na_2KSb photocathodes, Na 1s (a1, b1, c1, d1), Sb 3d (a2, b2, c2, d2) and K 2p (a3, b3, c3, d3) region scans are taken with Mgkα. a1-a3 are XPS spectra of minor oxidized Na_2KSb (TWH16), with QE=3.1% at 520nm. b1-b3 are XPS spectra of low-level oxidized Na_2KSb (TWH16-2), with QE=1.5%. c1-c3 are XPS spectra of moderate oxidized Na_2KSb (TWH11-2, oxidized), with QE=0. d1-d3 are XPS spectra of heavy oxidized Na_2KSb (SEA01, oxidized), with QE=0.*

6.6. Summary of XPS peak fitting results

This section summarizes the peak fitting results for Na-K-Sb material system in Table 6.3. It is important to note that absolute binding energies are influenced by surface band bending, leading to systematically overestimated values for n-type semiconductors (hexagonal K_3Sb, NaK_2Sb, Na_3Sb) and underestimated values for p-type semiconductors (Na_2KSb). In contrast, the energy separations and Auger parameters provide more reliable values, as they are largely unaffected by energy reference problems from surface charging or band bending.

Table 6.3: *Summary of peak fitting results of Sb, K-Sb, Na-K-Sb and Na-Sb films acquired from lab based XPS region scans in Alkα.*

Sample	Core level binding energy (eV)						Energy separation (eV)		Auger parameter (eV)
	Sb $3d_{5/2}$		K $2p_{3/2}$		Na 1s		$K2p_{3/2}$-$Sb3d_{5/2}$	Na1s-$Sb3d_{5/2}$	Na (1s, KL_1L_{23})
	BE	FWHM	BE	FWHM	BE	FWHM	Energy	Energy	Energy
Sb	528.2	1.3							
KSb	527.8	1.3	293.7	1.3			-234.2		
K_3Sb Mixed	526.3	1.3	293.5*	>1.3					
K_3Sb Hex	526.6	1.3	293.7	1.3			-232.9		
NaK_2Sb	526.6	1.3	293.6	1.3	1071.7	1.3	-233.0	545.1	2025.6
Na_2KSb	526.4(5)	1.3	293.3	1.3	1071.5	1.3	-233.2	545.0	2025.8
NaSb	527.9	1.3			1071.8	1.3		543.9	
Na_3Sb	526.8	1.3			1071.8	1.3		544.9	2025.6

*This value may fluctuate due to changes in the concentration of the cubic and hexagonal K_3Sb phases.

7. Conclusion and Outlook

7.1. Conclusion

This work reported the novel synthesis method and application of high-QE Na_2KSb photocathodes as electron sources for the SEALab superconducting radio-frequency (SRF) photoinjector. Though Na_2KSb demonstrated better robustness than Cs-K-Sb photocathodes and demonstrated capability for high-current operation in photoinjectors,[9,38] its adoption has historically been hindered by poor reproducibility and consequent large variations in its photoemissive properties including QE and dark lifetime.

Initial development conducted in dispenser chamber confirmed the limitations of traditional sequential deposition. The subsequent development of an alkali co-deposition method extended the time window for achieving optimal QE (QE $>1\%$ at 515 nm) and improved the success rate to over 50%. Despite this progress, preparation system limitations—including suboptimal geometry and unstable alkali flux—making the reproducible synthesis of high-performance photocathode films extremely difficult. The maximum QE achieved in this chamber was 2.6% at 515 nm, significantly lower than literature values[9] and with suboptimal stoichiometry from the ideal Na_2KSb composition.

To solve these limitations, a dedicated evaporation chamber was designed, commissioned, and a novel triple evaporation growth procedure has been developed. This development achieved a significant improvement, increasing the success rate to nearly 100% (after initial calibration) and consistently producing Na_2KSb photocathodes with QE values between 3% and 7% at 520 nm. For the first time, this enabled precise stoichiometric control within the narrow composition window required for optimal performance, simultaneously enhancing both QE and dark lifetime.

To push performance beyond the resolution of conventional XPS analysis, a

analytical model was developed to correlate stoichiometry with spatial QE homogeneity. This model guided a post-growth optimization method, whereby the QE gradient was used to guide fine-tuning, successfully elevating the central QE of both Na-oversaturated and Na-deficient samples to approximately 6%.

Statistical analysis established clear correlations between final stoichiometry and photoelectric properties. High-QE films with extended dark lifetime were consistently achieved within the optimal stoichiometry zone of the K/Sb ratio between 0.90 and 1.25 without Na enrichment. While in some conditions, Na-surface-enriched samples exhibited a lower photoemission threshold energy ($\sim$1.8 eV), however, resulting in lower dark lifetime.

The highlight of this work was the validation of a Na_2KSb photocathode (SEA03) within the SEALab photoinjector. Grown with the optimized triple evaporation recipe, the photocathode exhibited a QE of 5.4% at 520 nm and a dark lifetime exceeding 500 hours. Its successful integration demonstrated, for the first time, the operation of an SRF photoinjector with a Na_2KSb photocathode. Despite a QE reduction to 0.4% post-transfer, the photocathode demonstrated good robustness, maintaining functionality through operational incidents including field emission and electron back-bombardment.

This thesis also establishes a comprehensive XPS database for the Na-K-Sb system, including core-level peak shifts, energy separations and Auger parameters with the accompanying analysis of oxidation and thermal dissociation, providing a foundational resource for future research and development on this material.

7.2. Outlook

While this work has established a reproducible growth procedure for high-performance Na_2KSb photocathodes on molybdenum substrates and demonstrated their successful operation in SEALab SRF photoinjector, several works for fundamental understanding and performance enhancement remain. The following research directions are proposed to further advance the development of this promis-

ing material.

7.2.1. Synchrotron Radiation Based X-ray Characterization

Synchrotron radiation facilities offer X-ray beams with high brightness, superior collimation, and tunable wavelength, enabling a detailed characterization of electronic structure beyond the capabilities of laboratory-based XPS. An initial transfer and characterization of a Na_2KSb sample at the EMIL beamline at BESSY II (HZB) was conducted in October 2024. Unfortunately, vacuum degradation at the interface between the transport suitcase and the beamline load-lock led to severe sample oxidation, as evidenced by the HAXPES spectrum of the Sb $3d_{3/2}$ core level shown in Figure 7.1. The high-resolution data revealed the presence of multiple antimony oxidation states (Sb^{3-}, Sb^{-}, Sb^{0}, Sb^{3+}, Sb^{5+}, with FWHM of 0.8 eV), highlighting the potential of the technique, though the complex oxidized surface precluded a meaningful analysis of the original Na_2KSb material.

To enable successful future studies, the UHV suitcase has been redesigned and recommissioned in 2025 for a scheduled beamtime in December 2025 with upgraded interface. The planned experiment includes:

Depth-Dependent Compositional Analysis: As discussed in Section 4.5.1, the surface stoichiometry can differ from the bulk due to alkali metal segregation. Tunable synchrotron X-rays will be used for non-destructive depth profiling to quantify the homogeneity of Na_2KSb films and correlate it with growth parameters.

X-ray Absorption Near Edge Structure (XANES) Studies: XANES will be employed to investigate the electronic structure, oxidation states, and local coordination symmetry of the elements. These experimental results will be integrated into a feedback loop with ab initio calculations performed by collaborators to refine theoretical models of Na-K-Sb compounds.

High-Resolution photoelectron spectroscopy: This will involve precise measurement of the valence band structure, band gap, electron affinity, and doping type

for Na_2KSb, NaK_2Sb and K_3Sb films with soft X-ray. In addition, high-resolution photoelectron spectroscopy will also be used to verify the peak shifts and Auger parameters established in Chapter 6.

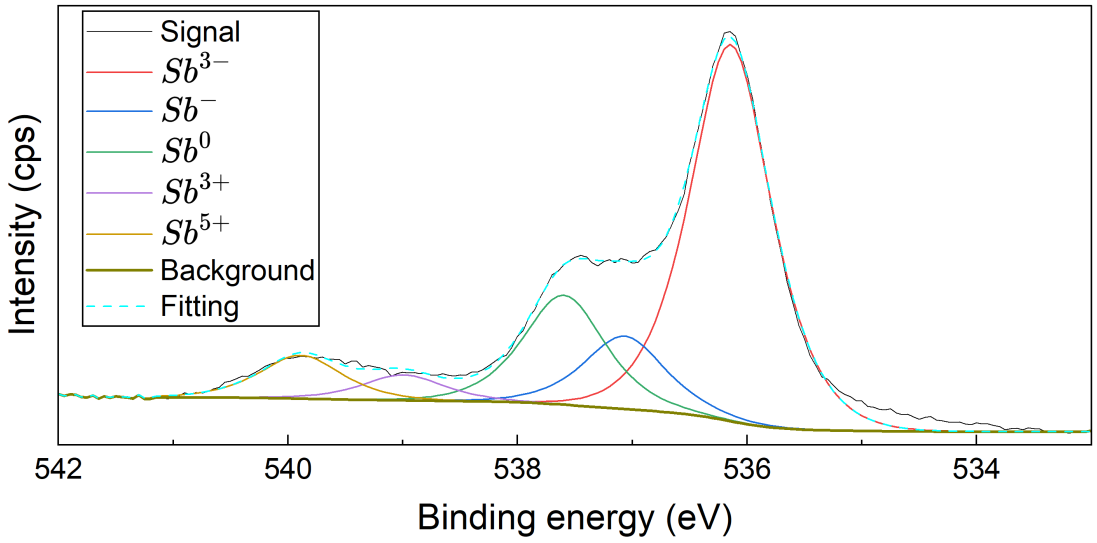


Figure 7.1: *HAXPES spectrum of the Sb $3d_{3/2}$ core level from an oxidized Na_2KSb sample (TWH11), measured at a photon energy of 3550 eV in EMIL beamline.*

7.2.2. Epitaxial Growth

Epitaxial growth of alkali-antimonides is an emerging frontier aimed at minimizing beam emittance by improving surface uniformity. The surface non-uniformities, such as physical roughness and work function variations increase the mean transverse energy (MTE) of the emitted electron beam, thereby degrading the beam brightness. While the new source geometry has reduced work function variations to below 0.03 eV over a 4 mm diameter area (as shown in Table A.1 for sample TWH25), physical roughness remains a key parameter for optimization.

The current polycrystalline Na_2KSb films are deposited onto polycrystalline Mo substrates with a surface roughness (R_q) of approximately 10 nm (Section 3.1). The polycrystalline nature of the film itself may further increase this roughness. Consequently, developing single-crystal or large-grained epitaxial films with low surface roughness could be the new direction for minimizing emittance. Studies on related alkali-antimonides, such Cs_3Sb and K_2CsSb, have demonstrated

that epitaxial films exhibit significantly lower surface roughness and consequently lower roughness-induced MTE compared to the polycrystalline samples in control group across the commonly used field gradient range in photoinjectors.[92,93,94]

The existing triple evaporation chamber at photocathode lab, with its highly stable evaporation sources operating at low deposition rates, provides a suitable platform for initial epitaxial growth experiments. The primary challenge lies in selecting an appropriate single-crystal substrate that lattice-matches with the cubic Na_2KSb phase. Single-crystal Si(100) is a promising candidate due to its low lattice mismatching with $Na_2KSb(100)$. In addition, it has excellent availability, well-established surface cleaning procedures, and relative high electrical and thermal conductivity (with doping) for the integration into a photoinjector.

A. Appendix

A.1. Additional XPS Studies

A.1.1. Sequential and Triple Evaporation

This section compares the XPS spectra of quasi-Na_2KSb photocathode films synthesised via traditional sequential evaporation (TWH11.2, Na:K ratio=2.0, QE =6.6%) and triple evaporation (TWH15, Na:K ratio=1.9, QE=5.6%). As shown in Figure A.1, the core-level peak positions for Na 1s, Sb 3d, and K 2p are highly consistent between the two samples, indicating that both growth methods produced the same Na_2KSb phase.

As shown in Figure A.1b, the primary Sb $3d_{5/2}$ peak is located at 526.4(5) eV for both samples. For the sequentially evaporated TWH11.2, peak fitting reveals a minor component at 527.7 eV, accounting for 14% of the total signal, which indicates the presence of an alkali-deficient phase. In contrast, the triple-evaporated TWH15 exhibits a much smaller secondary peak at 528.1 eV (5% of total signal), potentially attributable to the shutter shadowing effect during deposition, as previously discussed for Figure 4.9a.

The K 2p spectra, displayed in Figure A.1c, show the K $2p_{3/2}$ binding energy at 293.3 eV for both films. Similarly, the Na 1s spectra in Figure A.1d share a main peak at 1071.5 eV. While a difference is observed in the Na 1s line shape: TWH15 (triple evaporation) exhibits a single, sharp peak with a FWHM of 1.3 eV, whereas TWH11.2 (sequential evaporation) peak fitting reveals a second component at 1072.1 eV (16% of total intensity). The energy separation of this second component between Na 1s peak and Sb $3d_{5/2}$ peak is 544.4 eV. This value is similar to that of the secondary phase identified in the thermally dissociated study (Section 6.5.1), suggesting a similar alkali-deficient composition.

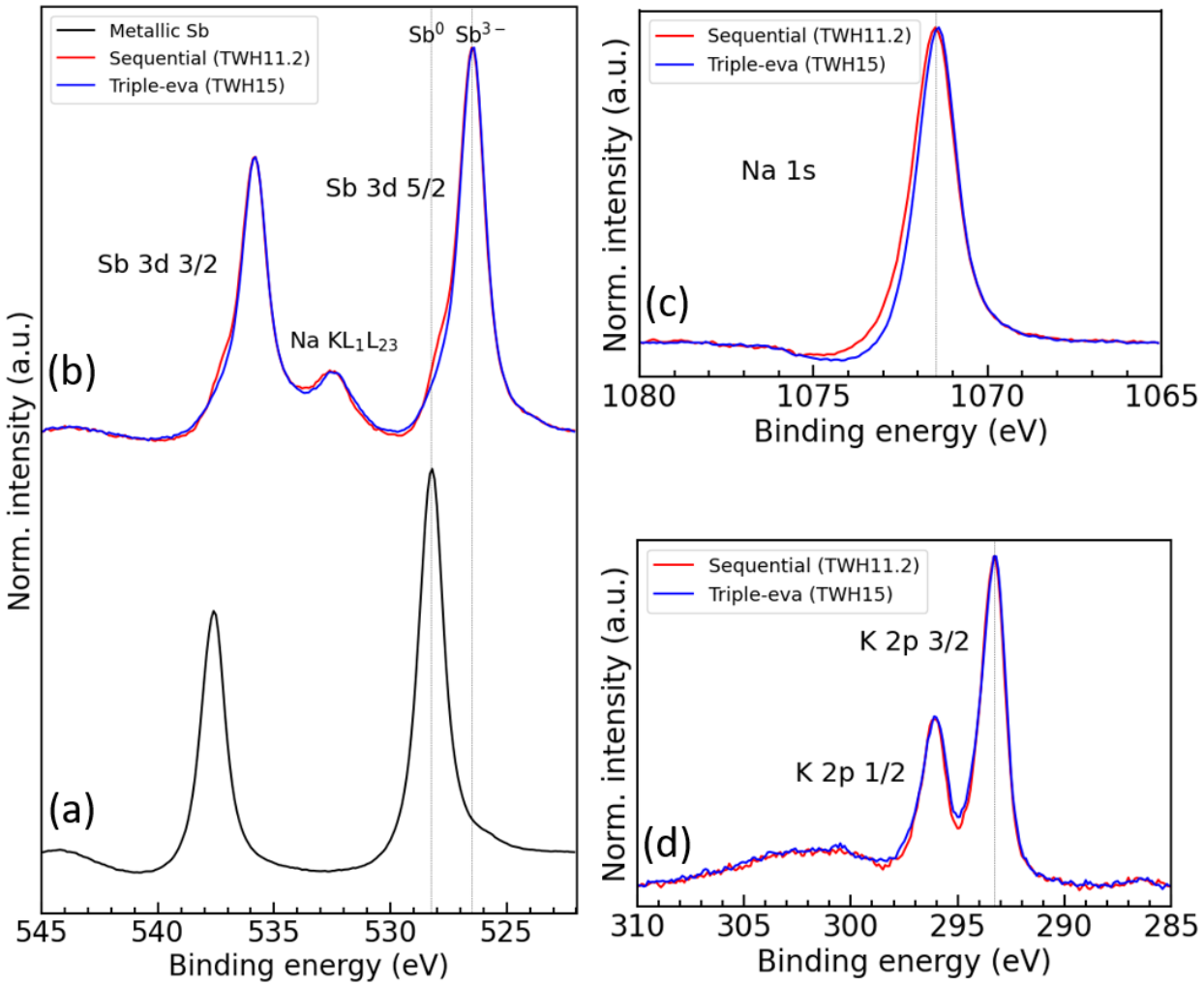


Figure A.1: *Al Kα XPS spectra of Na_2KSb photocathodes synthesis by two different growth methods. TWH11.2 ($Na_{2.0}K_{1.0}Sb_{1.0}$) for typical sequential growth method and TWH15 ($Na_{2.2}K_{1.2}Sb_{1.0}$) for triple evaporation method: (a) Sb 3d regions of metallic Sb; (b), (c) and (d) for Sb 3d, K 2p, and Na 1s regions of the two Na_2KSb films.*

A.1.2. Transformation from Na_2KSb to NaK_2Sb

This section present TWH24 (Figure A.2) as another comparison between NaK_2Sb and Na_2KSb film. The TWH24-1 ($Na_{0.8}K_{1.6}Sb$) is synthesised via sequential deposition, which exhibited no photocurrent at room temperature. Subsequent deposition of additional Na at an elevated substrate temperature of 170 °C converted the film to $Na_{2.2}K_{1.0}Sb$ (TWH24-2), yielding a QE of 3.4% after cooling to room

temperature.

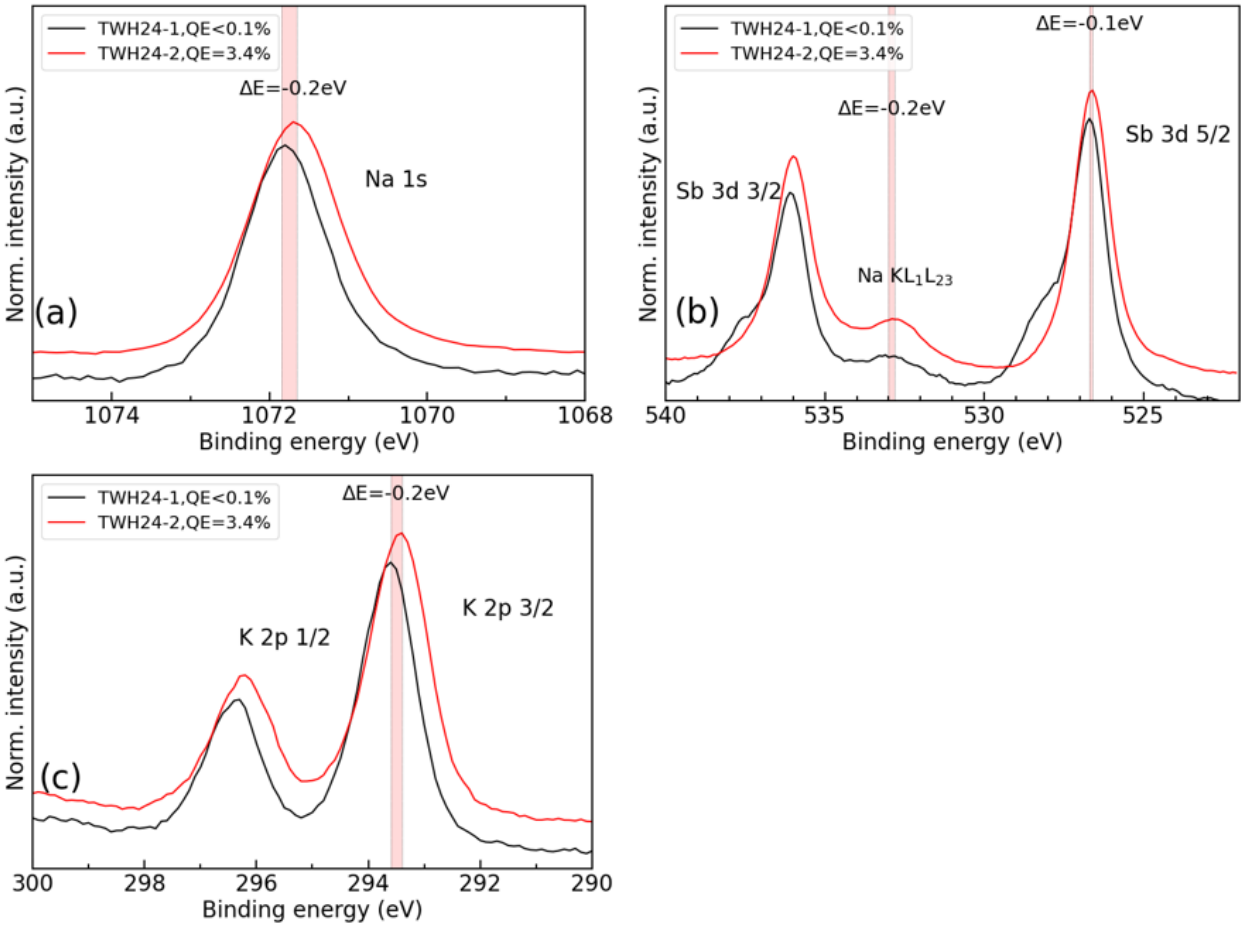


Figure A.2: *Al Kα XPS spectra of TWH24-1 ($Na_{0.8}K_{1.6}Sb$) and TWH24-2 ($Na_{2.2}K_{1.0}Sb$) photocathodes. (a), (b) and (c) are the region scans of Na 1s, K 2p and Sb 3d, respectively.*

A.1.3. High-QE K-Sb Film

This section details an accidentally formation of a high-QE K-Sb film, which exhibited a QE exceeding 1% at 520 nm. This result occurred due to an incomplete degassing procedure of the effusion cell. As discussed in Section 2.4.1.1, the high QE is attributed to the formation of a cubic K_3Sb phase, induced by the presence of oxygen during growth. This hypothesis is supported by a high O 1s peak intensity in the XPS region scan (Figure A.3a) and is consistent with the known oxygen-enhanced formation of high-QE K-Sb photocathode films.[34]

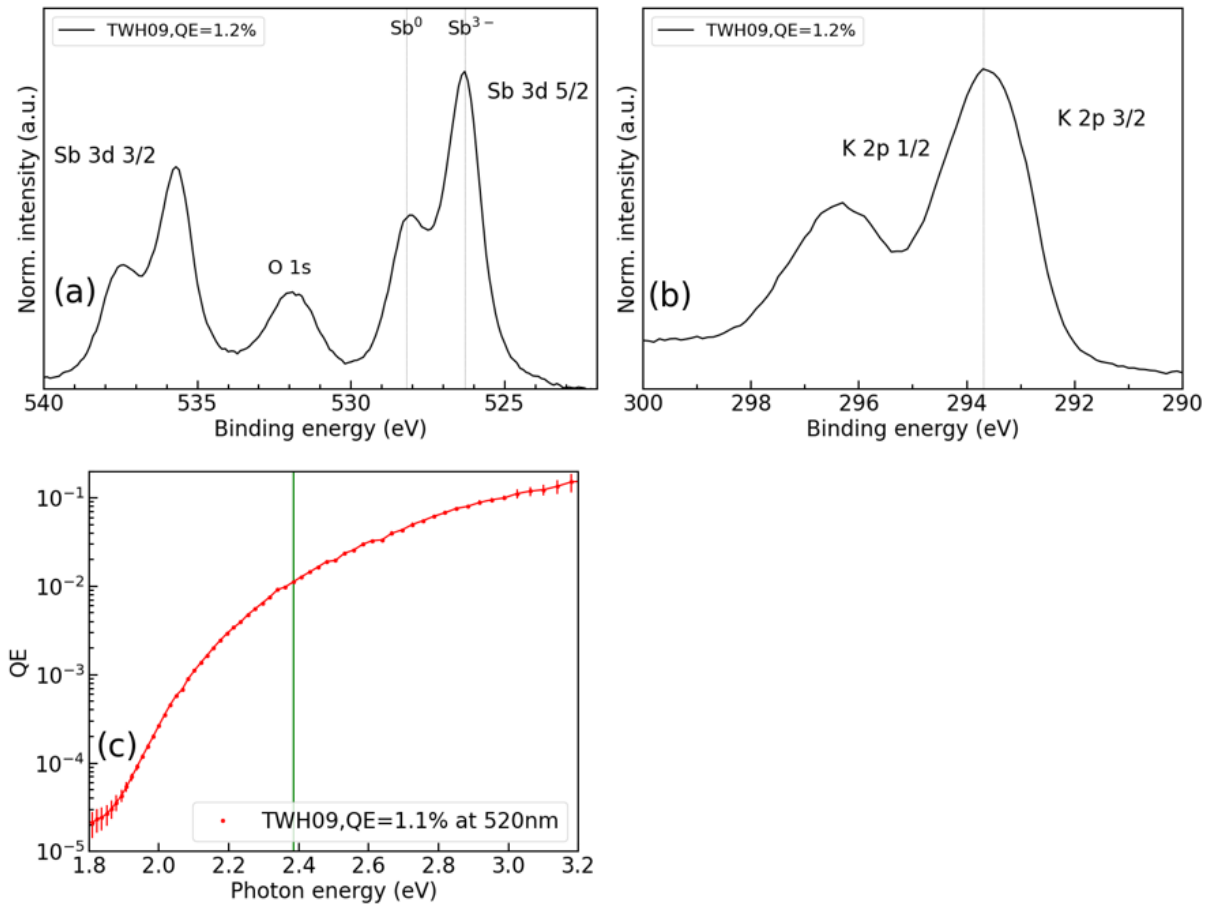


Figure A.3: *Al Kα XPS spectra and spectral response curve of TWH09 ($Na_{0.3}K_{3.5}Sb_{1.0}$) with high oxygen concentration. (a), (b) are the region scans of K 2p and Sb 3d, and (c) is the spectral response curve showing a QE of 1.1% at 520 nm.*

A.1.4. Valence Band Structure

Valence band XPS spectra were acquired using Al Kα for three samples: a metallic Sb film (TWH23-0), a hexagonal K_3Sb film (TWH23, QE<0.1%), and a Na_2KSb film (TWH25, QE=5.1%). The probe depth, calculated from three times the IMFP, is approximately 12 nm.

Although the signal-to-noise ratio was insufficient for a precise quantitative determination of the valence band maximum (VBM) position relative to the Fermi level, a qualitative comparison is possible. The spectra indicate that the VBM of hexagonal K_3Sb is closer to the Fermi level than that of Na_2KSb. This observation

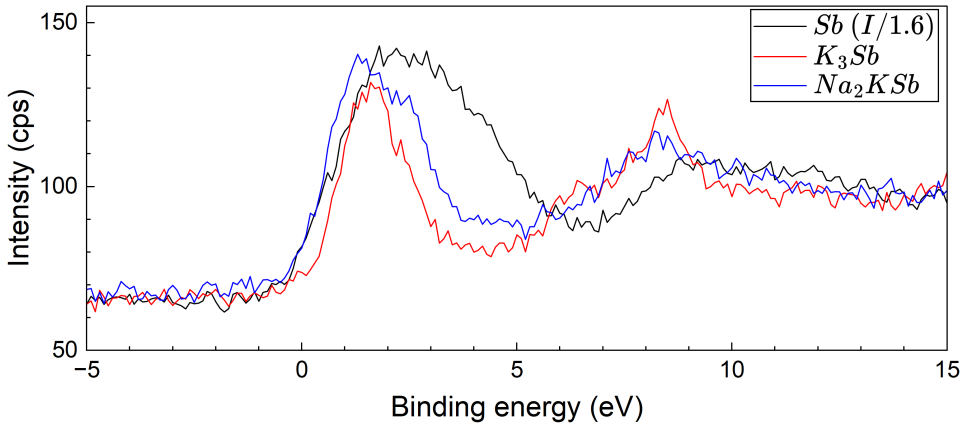


Figure A.4: *Al Kα XPS spectra of valence band structures of metallic Sb film (TWH23-Sb), hexagonal K_3Sb film (TWH23, QE<0.1%), and Na_2KSb film (TWH25, QE=5.1%).*

is consistent with the established electronic character of these materials, confirming the n-type nature of hexagonal K_3Sb and the p-type nature of Na_2KSb.

A.2. Thermal Stability of Na2KSb Photocathodes

More experimental results conducted on this topic are presented here as a supplement to Section 6.5.1.

A.2.1. Thermal Stability of TWH15-17

XPS analysis was performed before and after the thermal test using both Mg Kα (Figure A.5) and Al Kα (Figure A.6)sources. The primary effects of thermal loading on the Na_2KSb films were: (1) A decrease in surface K content. (2) An increase in surface Na content, except TWH17. (3) A secondary peak appeared in the Sb 3d spectra at higher binding energy, indicating the appearance of an alkali-deficient phase. (4) More pronounced stochiometric changes in the Mg Kα spectra (higher surface sensitivity) compared to the Al Kα, confirming the changes are surface-preferred. The extent of these changes varied between samples and was accompanied by minor peak shifts. A definitive correlation between the initial stoichiometry and the thermal stability requires further investigation.

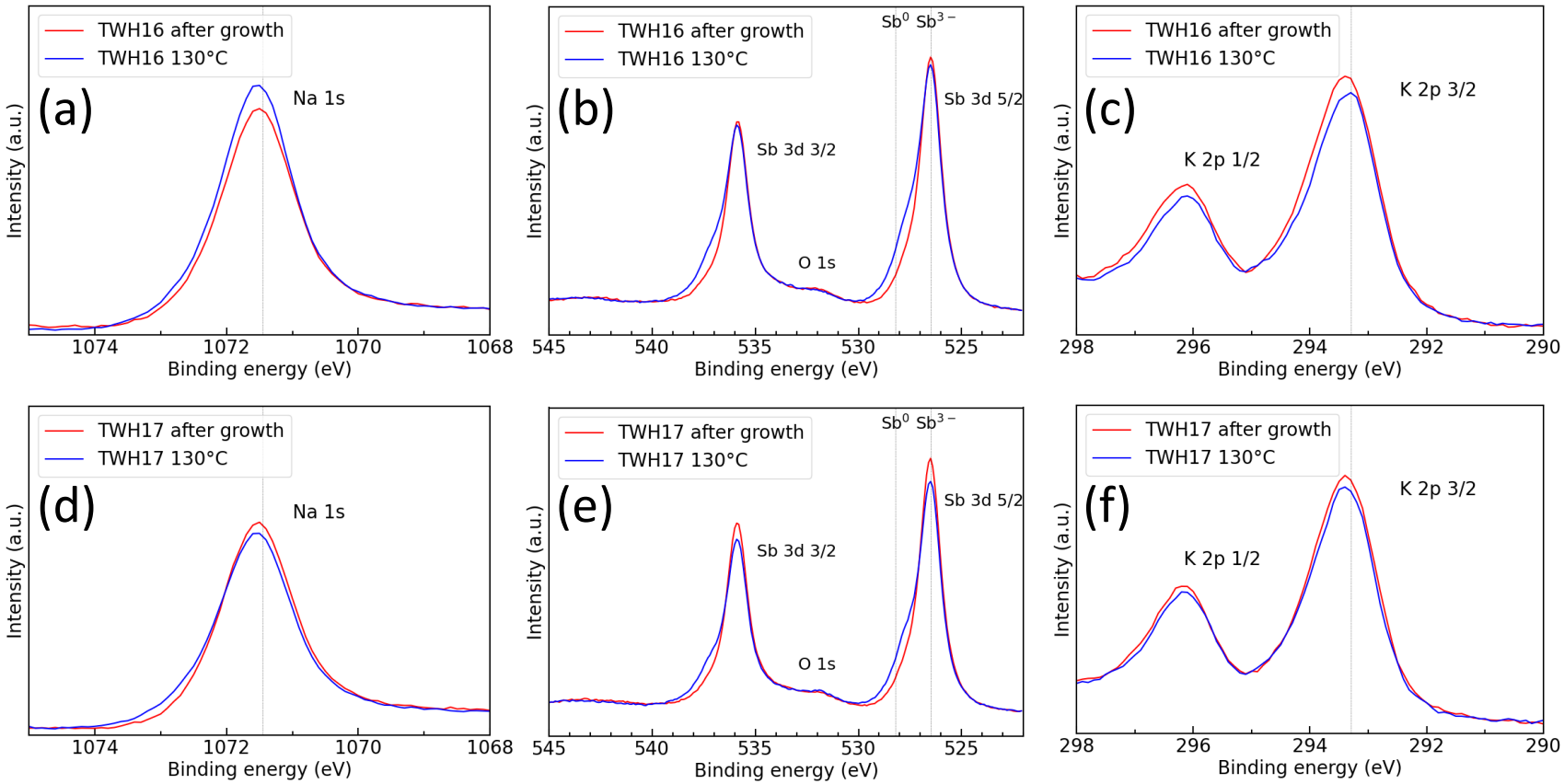


Figure A.5: *Mg Kα XPS region scans of TWH16 and TWH17 before and after the thermal dissociation test. (a), (d) for Na 1s region scans; (b), (e) for Sb 3d region scans; (c), (f) for K 2p region scans.*

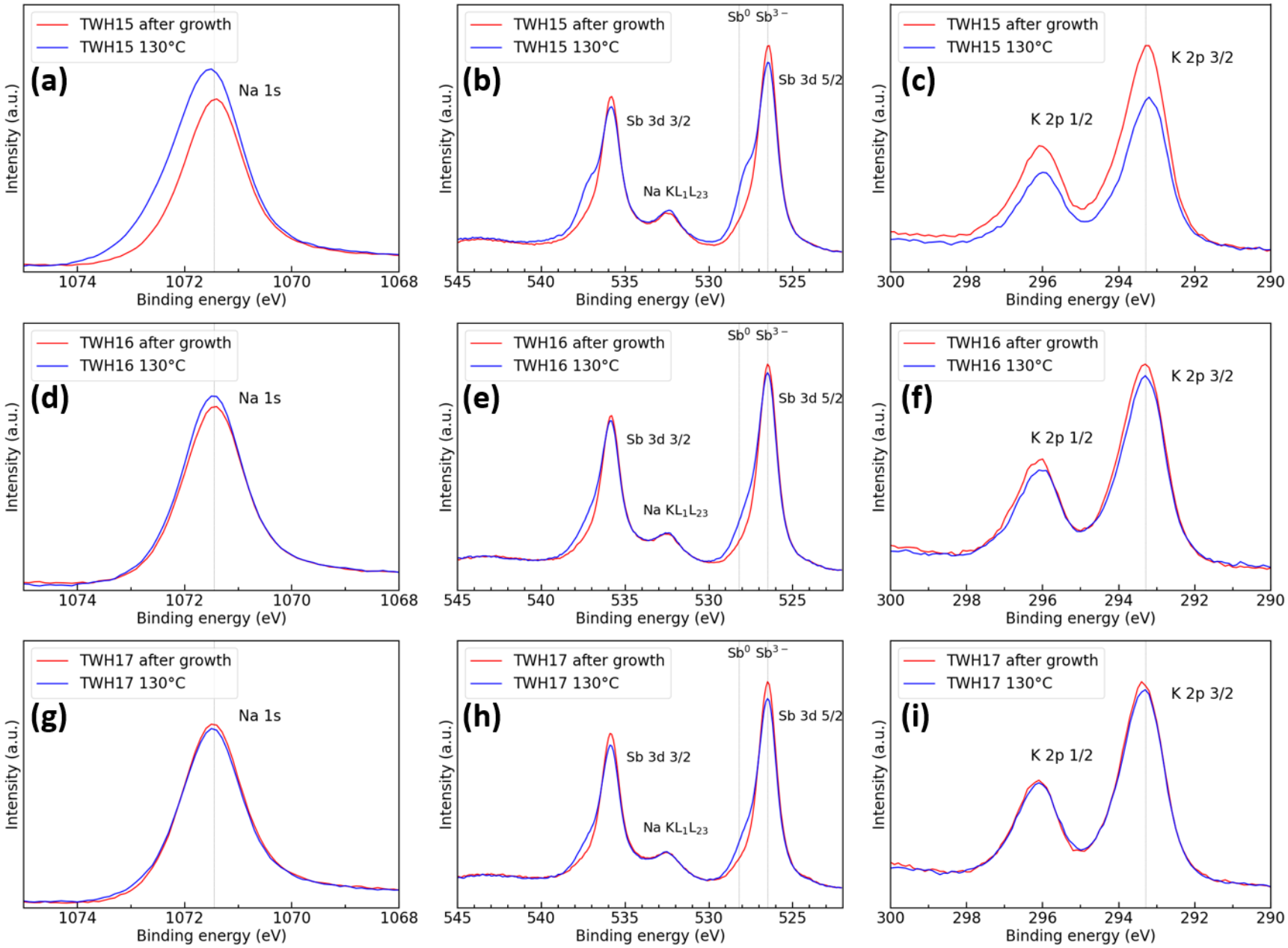


Figure A.6: *Al Kα XPS region scans of TWH15, TWH16 and TWH17 before and after the thermal dissociation test. (a), (d), (g) for Na 1s region scans; (b), (e), (h) for Sb 3d region scans; (c), (f), (i) for K 2p region scans.*

A.2.2. Thermal Stability of WH17 in Dispenser Based Chamber

Another thermal stability investigation was conducted on sample WH17, which was synthesized via alkali co-deposition in the dispenser chamber in 2023. This sample exhibited a surface stoichiometry of $Na_{1.5}K_{1.8}Sb$, deviating from the ideal NaK_2Sb composition, resulting in the low QE and short dark lifetime as reported in Section 4.1.6.

The thermal stability test was conducted on WH17 after an 18-day dark lifetime measurement. The sample followed a stepwise heating protocol: 70 °C, 90 °C, 110 °C, and 130 °C, with each temperature maintained for 24 hours. Following each step, the sample was cooled to room temperature for XPS analysis. The QE evolution and corresponding XPS spectra are presented in Figure A.7.

At temperatures below 90 °C, the QE demonstrated full recovery to 1.1% upon cooling, with XPS revealing no detectable changes in stoichiometry or core-level peak positions.

An irreversible QE drop to 0.9% occurred after the second XPS measurement, conducted before heating up to 110 °C. This degradation is attributed to potential beam damage or a minor pressure increase during XPS analysis, although no evidence of oxidation (e.g., oxide peaks in K 2p or Na 1s spectra) was observed.

Subsequent heating to 110 °C and 130 °C led to further QE decline, while the effects of repeated XPS measurements could not be ruled out. The evidence of stoichiometric changes related to thermal dissociation happened after the 130 °C step, showing similar result as discussed in last section: A decrease in peak intensity for K 2p, an increase of Na and an appearance of a secondary peak in Sb 3d region.

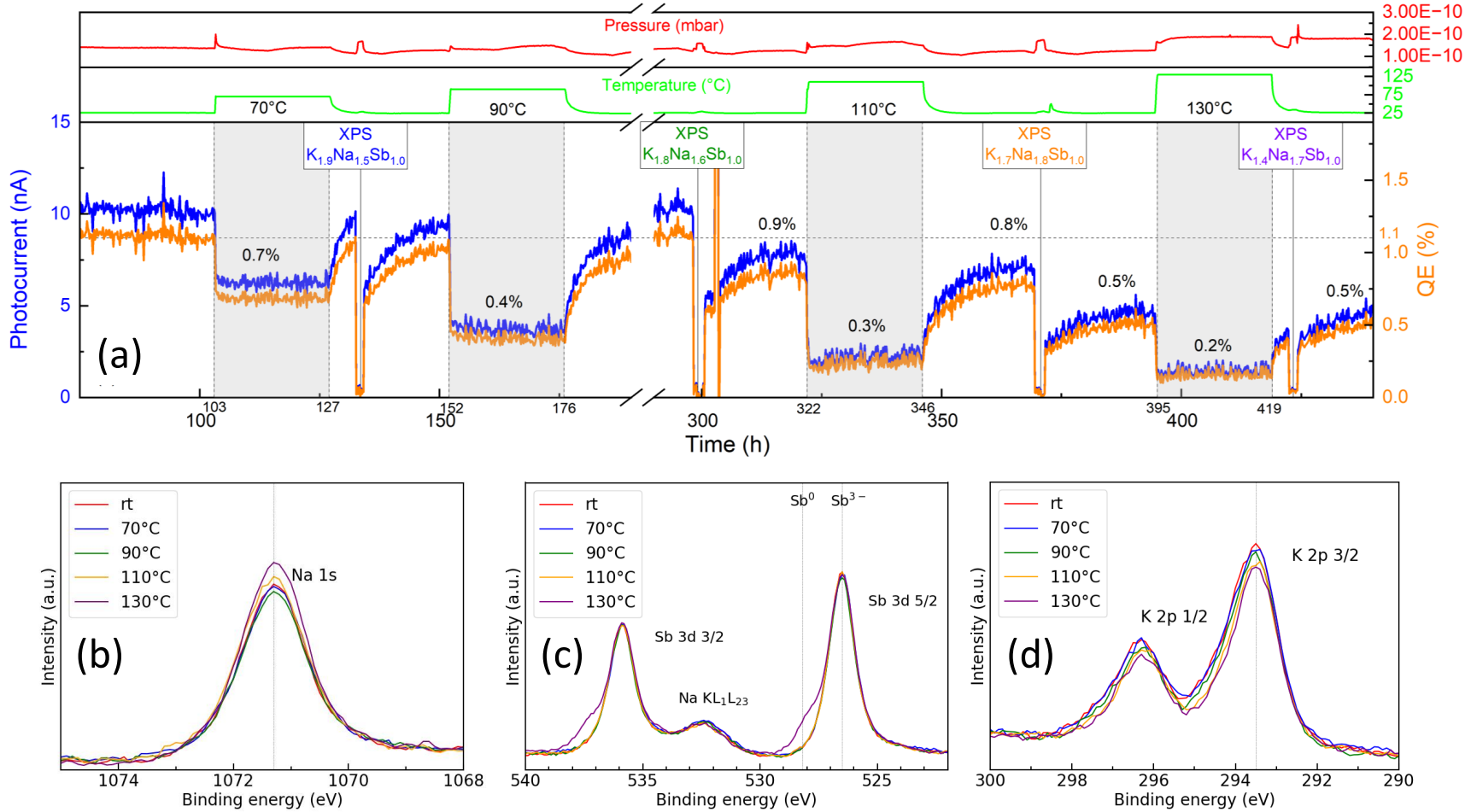


Figure A.7: *WH17 thermal stability test protocol and stoichiometry change: (a) the thermal stability test protocol; (b), (c) and (d) XPS spectra (Al Kα) of Na 1s, Sb 3d, and K 2p after heating to 70 °C, 90 °C, 110 °C and 130 °C for 24 h.*

A.2.3. Temperature-Dependent QE Behavior of Na-oversaturated Samples

This subsection presents the temperature-dependent QE of the slightly Na-oversaturated sample TWH13 ($Na_{2.2}K_{0.9}Sb_{1.0}$). As shown in the post-growth cooling curve of Figure 4.1, the QE of this sample decrease during cooling down. Meanwhile, a heating up could recover the QE as shown in Figure A.8a.

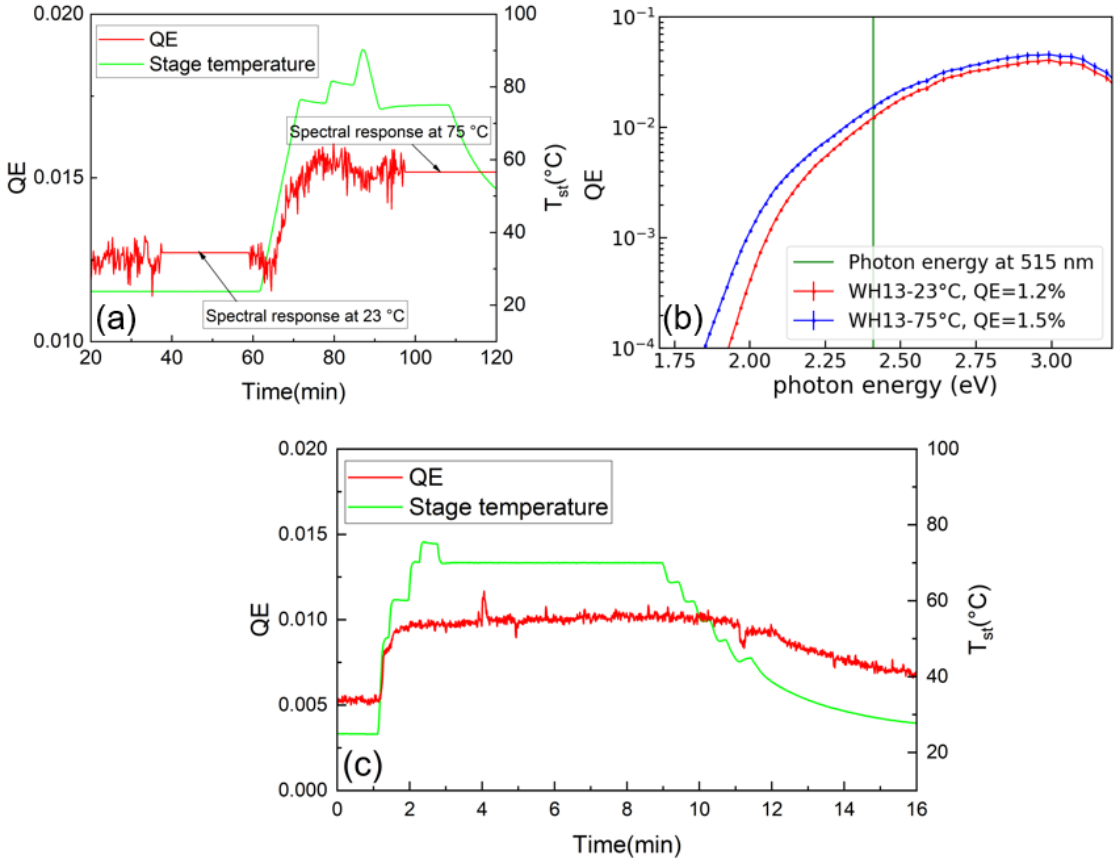


Figure A.8: *Temperature-dependent QE behavior of Na-oversaturated samples: (a) QE versus substrate temperature for TWH13 ($Na_{2.2}K_{0.9}Sb$); (b) Spectral response of TWH13 measured at 23 °C and 75 °C; (c) QE versus substrate temperature for WH11 ($Na_{2.4}K_{0.7}Sb$).*

To investigate this phenomenon further, spectral response curves were measured. The QE at 75 °C is found to exceed that at 23 °C across the entire spectral range, as shown in Figure A.8b. This positive correlation between QE and temperature is not unique to TWH13, a similar trend was observed in other Na-

oversaturated samples, such as WH11 ($Na_{2.4}K_{0.7}Sb$), as demonstrated in Figure A.8c.

A.3. Additional Spectral Response Studies

A.3.1. Spectral Response at increased Temperature

To quantify the relationship between the energy broadening $\Delta E(T)$ and substrate temperature, the spectral response of sample TWH18 was measured at room temperature, 70 °C, 90 °C, and 110 °C. The corresponding values of $\Delta E(T)$ were determined to be 0.043 eV, 0.050 eV, 0.052 eV, and 0.053 eV by Urbach fitting, respectively. These results demonstrate a positive correlation, where $\Delta E(T)$ increases with rising temperature.

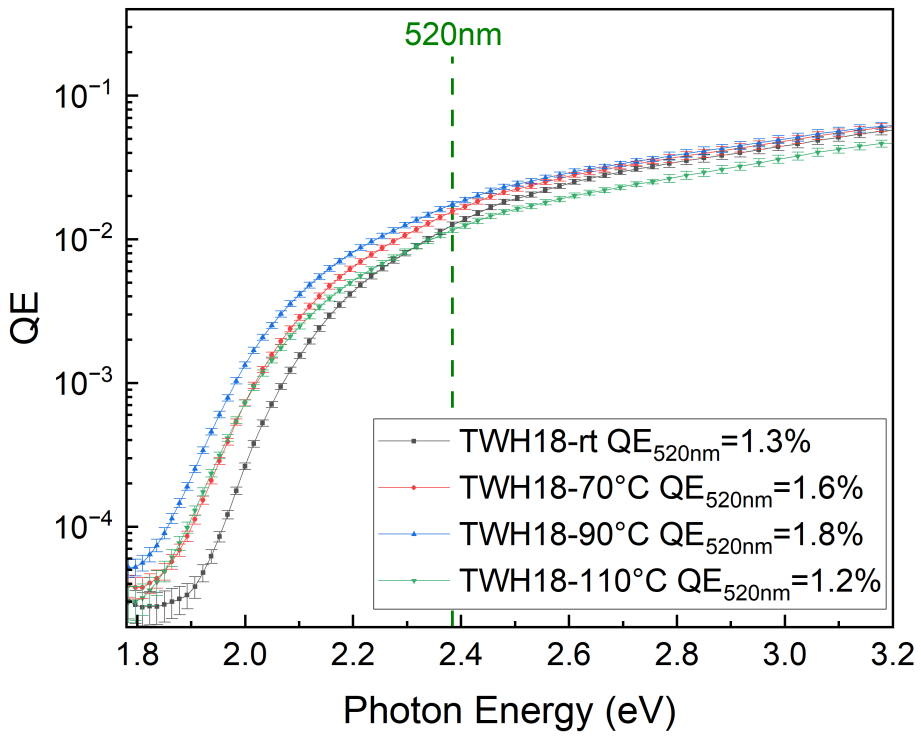


Figure A.9: *Spectral response curve of TWH18 measured at sample temperature of room temperature, 70°C, 90°C and 110°C.*

A.3.2. Spectral Response at different positions

Table A.1: *Urbach and Kane fitting of TWH22 (old geometry) and TWH25 (new geometry) spectral response curves in four sample positions. These four points lie on a straight line passing through the center of the film, and the distance between two adjacent points is 1.4 mm, with stoichiometric ratio of Na:K in position 1< position 2< position 3< position 4.*

Old geometry						New geometry					
TWH22	Urbach		Kane		QE	TWH25	Urbach		Kane		QE
	B	E_T	n	E_T			B	E_T	n	E_T	
Position1	22.1	1.91	1.36	1.92	4.4%	Position1	23.8	1.90	1.30	1.92	5.0%
Position2	21.9	1.91	1.33	1.91	4.4%	Position2	23.9	1.90	1.34	1.90	5.1%
Position3	22.2	1.93	1.41	1.93	3.7%	Position3	23.9	1.90	1.36	1.90	5.1%
Position4	22.3	1.95	1.41	1.93	2.8%	Position4	24.3	1.90	1.39	1.89	5.0%

A.4. Full Dataset

The full dataset of Na-K-Sb photocathodes deposited from September. 2024 to August. 2025 is listed in Table A.2 and Table A.3.

Table A.2: *QE (at 520 nm), dark lifetime and stoichiometry of Na-K-Sb photocathodes deposited from September.2024 to April.2025*

Sample	Method	max QE	Lifetime	Stoichiometry(AlKα)	Stoichiometry(MgKα)	Na/Sb and K/Sb gradient	Sb gradient
TWH10	seq (test)	0%	-	$Na_{1.4}K_{1.2}Sb_{1.0}$	-	-	-
TWH11	seq (test)	0%	-	$Na_{1.2}K_{2.0}Sb_{1.0}$	-	-	-
TWH11+Na	extra Na	6.6%	low	$Na_{2.0}K_{1.0}Sb_{1.0}$	$Na_{3.3}K_{1.2}Sb_{1.0}$	1.70/1.25	0.78
TWH12	seq	>3.3%	+	$Na_{0.8}K_{1.7}Sb_{1.0}$	$Na_{1.7}K_{1.5}Sb_{1.0}$	1.11/1.22	0.79
TWH13	tri-1	5.2%	67h	$Na_{2.2}K_{0.7}Sb_{1.0}$	-	-	0.83
TWH14	tri-1	6.7%	63h	$Na_{2.4}K_{1.0}Sb_{1.0}$	-	-	-
TWH15	tri-1	5.6%	220h	$Na_{2.2}K_{1.2}Sb_{1.0}$	-	-	0.81
TWH15-1	thermal	-	-	$Na_{2.6}K_{0.8}Sb_{1.0}$	-	-	0.85
SEA00	tri-1	5.0%	223h	$Na_{2.0}K_{1.1}Sb_{1.0}$	-	-	-
SEA01	tri-1	>4.0%	+	-	-	-	-
TWH16	tri-1	3.1%	500h+	$Na_{1.9}K_{1.2}Sb_{1.0}$	$Na_{1.9}K_{1.4}Sb_{1.0}$	1.03/1.25	0.84
TWH16-1	thermal	-	-	$Na_{1.8}K_{1.1}Sb_{1.0}$	$Na_{2.0}K_{1.3}Sb_{1.0}$	1.07/1.28	0.85
TWH16-2	extra K	-	-	$Na_{1.6}K_{1.9}Sb_{1.0}$	$Na_{2.4}K_{2.3}Sb_{1.0}$	1.31/1.32	0.79
TWH17	tri-1	3.4%	500h+	$Na_{1.9}K_{1.2}Sb_{1.0}$	$Na_{2.2}K_{1.5}Sb_{1.0}$	1.15/1.27	0.82
TWH17-1	thermal	-	-	$Na_{1.6}K_{1.2}Sb_{1.0}$	$Na_{2.1}K_{1.4}Sb_{1.0}$	1.16/1.28	0.83
SEA02	tri-1*	3.6%	108h	-	-	-	-
TWH18	tri-1*	3.7%	410h	$Na_{2.3}K_{1.0}Sb_{1.0}$	$Na_{2.3}K_{1.3}Sb_{1.0}$	1.07/1.37	0.83
TWH19	tri-1*	1.4%	388h	$Na_{2.0}K_{1.2}Sb_{1.0}$	$Na_{2.0}K_{1.2}Sb_{1.0}$	1.07/1.10	0.86
TWH19+Na	extra Na	3.9%	288h	$Na_{2.2}K_{1.1}Sb_{1.0}$	$Na_{2.2}K_{1.3}Sb_{1.0}$	1.11/1.23	0.89
TWH19+2Na	extra Na	5.9%	263h	$Na_{2.5}K_{0.8}Sb_{1.0}$	$Na_{2.9}K_{0.9}Sb_{1.0}$	1.28/1.22	0.85
TWH19+3Na	extra Na	4.2%	80h	$Na_{2.9}K_{0.6}Sb_{1.0}$	$Na_{3.4}K_{0.6}Sb_{1.0}$	1.34/1.21	0.84
TWH19+4Na	extra Na	2.5%	89h	$Na_{3.1}K_{0.4}Sb_{1.0}$	$Na_{3.6}K_{0.4}Sb_{1.0}$	1.35/1.06	0.84

Table A.3: *QE (at 520 nm), dark lifetime and stoichiometry of Na-K-Sb photocathodes deposited from May.2025 to August.2025*

Sample	Method	max QE	Lifetime	Stoichiometry(AlKα)	Stoichiometry(MgKα)	Na/Sb and K/Sb gradient	Sb gradient
TWH20	tri-1*	2.3%	119h	$Na_{2.2}K_{0.8}Sb_{1.0}$	$Na_{2.5}K_{0.8}Sb_{1.0}$	1.21/1.22	0.85
TWH21	tri-1*	>2.4%	+	$Na_{2.2}K_{0.9}Sb_{1.0}$	$Na_{2.4}K_{1.1}Sb_{1.0}$	1.18/1.24	0.82
TWH22	tri-2 (test)	4.7%	500h+	-	-	-	-
TWH22-1	extra K+Sb	6.2%	500h+	-	-	-	-
TWH22-2	extra K+Sb	6.5%	526h	-	-	-	-
TWH22-3	extra K+Sb	6.3%	279h	$Na_{2.3}K_{0.9}Sb_{1.0}$	$Na_{2.5}K_{1.1}Sb_{1.0}$	1.16/1.31	0.83
TWH23	seq (test)	0%	-	$Na_{3.0}K_{0.1}Sb_{1.0}$	$Na_{8.9}K_{0.0}Sb_{1.0}$	1.54/-	0.75
TWH24	tri-2 (test)	0%	-	$Na_{0.8}K_{1.6}Sb_{1.0}$	$Na_{1.4}K_{1.6}Sb_{1.0}$	1.51/1.09	0.82
TWH24+Na	extra Na	3.4%	500h+	$Na_{2.2}K_{1.0}Sb_{1.0}$	$Na_{3.2}K_{1.0}Sb_{1.0}$	1.55/1.19	0.79
TWH25	tri-2	5.1%	500h+	$Na_{1.8}K_{0.9}Sb_{1.0}$	$Na_{2.0}K_{1.1}Sb_{1.0}$	1.17/1.28	0.83
SEA03	tri-2	5.5%	500h+	-	-	-	-
TP01	tri-2	4.0%	500h+	$Na_{1.7}K_{1.2}Sb_{1.0}$	$Na_{2.2}K_{1.3}Sb_{1.0}$	1.49/1.13	0.82
Na-Sb	-	0%	-	$Na_{3.2}Sb_{1.0}$	$Na_{4.0}Sb_{1.0}$	1.35/-	0.84
K-Sb	-	0%	-	$K_{3.0}Sb_{1.0}$	-	-	

*partially depleted Na source

Bibliography

[1] Z. T. Zhao, Z. Wang, C. Feng, S. Chen, and L. Cao. "Energy recovery linac based fully coherent light source". In: *Scientific Reports* 11.1 (2021), 23875. ISSN: 2045-2322.

[2] A Neumann, B Alberdi, T Birke, P Echevarria, D Eichel, F Falkenstern, R Fleischhauer, A Frahm, F Goebel, A Heugel, et al. "bERLinPro becomes SEALab: Status and perspective of the energy recovery linac at HZB". In: *Proc. IPAC'22*. JACoW Publishing, 2022, 1110–1113.

[3] Paul Emma, R Akre, J Arthur, R Bionta, C Bostedt, J Bozek, A Brachmann, P Bucksbaum, Ryan Coffee, F-J Decker, et al. "First lasing and operation of an ångstrom-wavelength free-electron laser". In: *nature photonics* 4.9 (2010), 641–647.

[4] Jana Schaber, Rong Xiang, and Nikolai Gaponik. "Review of photocathodes for electron beam sources in particle accelerators". In: *Journal of Materials Chemistry C* 11.9 (2023), 3162–3179. ISSN: 2050-7534.

[5] D. Filippetto, P. Musumeci, R. K. Li, B. J. Siwick, M. R. Otto, M. Centurion, and J. P. F. Nunes. "Ultrafast electron diffraction: Visualizing dynamic states of matter". In: *Reviews of Modern Physics* 94.4 (Dec. 2022), 045004.

[6] D. H. Dowell, I. Bazarov, B. Dunham, K. Harkay, C. Hernandez-Garcia, R. Legg, H. Padmore, T. Rao, J. Smedley, and W. Wan. "Cathode R&D for future light sources". In: *Nuclear Instruments and Methods in Physics Research Section A: Accelerators, Spectrometers, Detectors and Associated Equipment* 622.3 (2010), 685–697.

[7] AH Sommer. "New photoemissive cathodes of high sensitivity". In: *Review of Scientific Instruments* 26.7 (1955), 725–726.

[8] William Edward Spicer. “Photoemissive, photoconductive, and optical absorption studies of alkali-antimony compounds”. In: *Physical Review* 112.1 (1958), 114–114.

[9] L Cultrera, S Karkare, B Lillard, A Bartnik, I Bazarov, B Dunham, W Schaff, and K Smolenski. “Growth and characterization of rugged sodium potassium antimonide photocathodes for high brilliance photoinjector”. In: *Applied Physics Letters* 103.10 (2013).

[10] ZT Zhao, Zhen Wang, Chao Feng, Si Chen, and Lu Cao. “Energy recovery linac based fully coherent light source”. In: *Scientific Reports* 11.1 (2021), 23875.

[11] Daniele Filippetto, Pietro Musumeci, RK Li, Bradley John Siwick, MR Otto, Martin Centurion, and JPF Nunes. “Ultrafast electron diffraction: Visualizing dynamic states of matter”. In: *Reviews of Modern Physics* 94.4 (2022), 045004.

[12] Winfried Decking, S Abeghyan, P Abramian, A Abramsky, A Aguirre, C Albrecht, P Alou, M Altarelli, P Altmann, K Amyan, et al. “A MHz-repetition-rate hard X-ray free-electron laser driven by a superconducting linear accelerator”. In: *Nature photonics* 14.6 (2020), 391–397.

[13] Jana Schaber, Rong Xiang, and Nikolai Gaponik. “Review of photocathodes for electron beam sources in particle accelerators”. In: *Journal of Materials Chemistry C* 11.9 (2023), 3162–3179.

[14] T Kamps, B Alberdi, T Birke, EJ Brookes, J Dube, P Echevarria, D Eichel, E Ergenlik, R Fleischhauer, A Frahm, et al. “First Beam Commissioning of The HZB SRF Photoelectron Gun”. In: *Proc. IPAC’25*. JACoW Publishing, 2025.

[15] H Jia, T Li, T Wang, Y Zhao, X Zhang, H Xu, Z Liu, J Liu, L Lin, H Xie, et al. “High-brightness megahertz-rate beam from a direct-current and

superconducting radio-frequency combined photocathode gun". In: *Physical Review Research* 6.4 (2024), 043165.

[16] Bruce Dunham, John Barley, Adam Bartnik, Ivan Bazarov, Luca Cultrera, John Dobbins, Georg Hoffstaetter, Brent Johnson, Roger Kaplan, Siddharth Karkare, et al. "Record high-average current from a high-brightness photoinjector". In: *Applied Physics Letters* 102.3 (2013).

[17] F Sannibale, D Filippetto, H Qian, C Mitchell, F Zhou, T Vecchione, RK Li, S Gierman, and J Schmerge. "High-brightness beam tests of the very high frequency gun at the Advanced Photo-injector EXperiment test facility at the Lawrence Berkeley National Laboratory". In: *Review of Scientific Instruments* 90.3 (2019).

[18] Xing-Heng Wang, Guan Shu, Hou-Jun Qian, Xu-Dong Li, Zi-Peng Liu, Zeng-Gong Jiang, Hao Meng, Cao-Cao Xing, Qin Zhou, and Hai-Xiao Deng. "Experimental demonstration of dark current mitigation by an over-inserted plug in a normal conducting very-high-frequency gun". In: *Physical Review Accelerators and Beams* 28.4 (2025), 043401.

[19] I Petrushina, VN Litvinenko, Y Jing, J Ma, I Pinayev, K Shih, G Wang, YH Wu, Z Altinbas, JC Brutus, et al. "High-brightness continuous-wave electron beams from superconducting radio-frequency photoemission gun". In: *Physical Review Letters* 124.24 (2020), 244801.

[20] Dongming Ouyang, Yonglong Zhao, Huamu Xie, Xinkai Zhang, Sheng Zhao, Liwen Feng, Kexin Liu, and Senlin Huang. "Performance of bialkali photocathode in DC-SRF photoinjector". In: *Nuclear Instruments and Methods in Physics Research Section A: Accelerators, Spectrometers, Detectors and Associated Equipment* 1026 (2022), 166204.

[21] Julius Kühn, Nawar Al-Saokal, Markus Bürger, Marc Dirsat, Andre Frahm, Andreas Jankowiak, Thorsten Kamps, Guido Klemz, SMA Neumann, and H Ploetz. "Thermal load studies on the photocathode insert with exchange-

able plug for the BERLinPro SRF-photoinjector". In: *Proc. IPAC'19*. JACoW Publishing, 2019.

[22] William E Spicer. "Photoemission and related properties of the alkali-antimonides". In: *Journal of Applied Physics* 31.12 (1960), 2077–2084.

[23] Pallavi Saha, Oksana Chubenko, J Kevin Nangoi, Tomas Arias, Eric Montgomery, Shashi Poddar, Howard A Padmore, and Siddharth Karkare. "Theory of photoemission from cathodes with disordered surfaces". In: *Journal of Applied Physics* 133.5 (2023).

[24] William Edward Spicer. "Photoemissive, photoconductive, and optical absorption studies of alkali-antimony compounds". In: *Physical review* 112.1 (1958), 114.

[25] John D Dow and David Redfield. "Toward a unified theory of Urbach's rule and exponential absorption edges". In: *Physical Review B* 5.2 (1972), 594.

[26] T Kamps, MAH Schmeißer, Berlin HZB, Germany E Muller, and M Ruiz-Oses. "Influence of growth method on K3Sb photocathode structure and performance". In: *Proc. IPAC'14*. JACoW Publishing, 2014.

[27] Susanne Schubert, Jared Wong, Jun Feng, Siddharth Karkare, Howard Padmore, Miguel Ruiz-Osés, John Smedley, Erik Muller, Zihao Ding, Mengjia Gaowei, et al. "Bi-alkali antimonide photocathode growth: An X-ray diffraction study". In: *Journal of Applied Physics* 120.3 (2016).

[28] WH McCarroll. "Phases in the photoelectric sodium-potassium-antimony system". In: *Journal of Physics and Chemistry of Solids* 16.1-2 (1960), 30–36.

[29] WH McCarroll. "Chemical and structural characteristics of the potassium-cesium-antimony photocathode". In: *Journal of Physics and Chemistry of Solids* 26.1 (1965), 191–195.

[30] Luca Cultrera, Ivan Bazarov, Adam Bartnik, Bruce Dunham, Siddharth Karkare, Richard Merluzzi, and Matthew Nichols. “Thermal emittance and response time of a cesium antimonide photocathode”. In: *Applied Physics Letters* 99.15 (2011).

[31] Alice Galdi, William JI DeBenedetti, Jan Balajka, Luca Cultrera, Ivan V Bazarov, Jared M Maxson, and Melissa A Hines. “The effects of oxygen-induced phase segregation on the interfacial electronic structure and quantum efficiency of Cs3Sb photocathodes”. In: *The Journal of Chemical Physics* 153.14 (2020).

[32] Chuni Ghosh and BP Varma. “Preparation and study of properties of a few alkali antimonide photocathodes”. In: *Journal of Applied Physics* 49.8 (1978), 4549–4553.

[33] P Dolizy. “Growth of Alkali Antimonide Films for Photocathodes”. In: *Philips Tech. Rev.* 40.1 (1982), 19–28.

[34] Alfred Hermann Sommer and Ladislaus Marton. “Photoemissive materials: preparation, properties, and uses”. In: *Physics Today* 23.3 (1970), 89–91.

[35] Koichi Momma and Fujio Izumi. “VESTA 3 for three-dimensional visualization of crystal, volumetric and morphology data”. In: *Applied Crystallography* 44.6 (2011), 1272–1276.

[36] Raymond Amador, Holger-Dietrich Saßnick, and Caterina Cocchi. “Electronic structure and optical properties of Na2KSb and NaK2Sb from first-principles many-body theory”. In: *Journal of Physics: Condensed Matter* 33.36 (2021), 365502.

[37] Chung Xu, Richard Schier, and Caterina Cocchi. “Electronic and optical properties of computationally predicted Na–K–Sb crystals”. In: *Electronic Structure* 7.1 (2025), 015001.

[38] P Dolizy and F Groliere. “Dissociation energies of alkali antimonides as thin layers”. In: *Journal of Physics D: Applied Physics* 19.4 (1986), 687.

[39] Martin AH Schmeißer, Sonal Mistry, Hans Kirschner, Susanne Schubert, Andreas Jankowiak, Thorsten Kamps, and Julius Kühn. "Towards the operation of Cs-K-Sb photocathodes in superconducting rf photoinjectors". In: *Physical Review Accelerators and Beams* 21.11 (2018), 113401.

[40] Bojan Erjavec. "Alkali vapour pressure variations during Na2KSb (Cs) photocathode synthesis". In: *Vacuum* 45.5 (1994), 617–622.

[41] B Erjavec. "Alkali metal vapour dynamics during Na2KSb (Cs) photocathode growth". In: *Vacuum* 43.12 (1992), 1171–1175.

[42] Jun Feng, Siddharth Karkare, James Nasiatka, Susanne Schubert, John Smedley, and Howard Padmore. "Near atomically smooth alkali antimonide photocathode thin films". In: *Journal of Applied Physics* 121.4 (2017).

[43] Mengjia Gaowei. *Bi-alkali antimonide photocathodes for LEReC DC gun*. Tech. rep. Brookhaven National Lab.(BNL), Upton, NY (United States), 2019.

[44] David Garcia, B Schaap, A Ody, P Musumeci, C Pennington, J Maxson, GJ Silvi, A Mostacci, E Chiadroni, A Giribono, et al. "NaKSb photocathode tests in a high gradient S-band photoinjector". In: *Proc. IPAC'24*. JACoW Publishing, 2024.

[45] Julius Kühn, Nawar Al-Saokal, Markus Bürger, Marc Dirsat, Andre Frahm, Andreas Jankowiak, Thorsten Kamps, Guido Klemz, Sonal Mistry, Axel Neumann, and Henry Plötz. "Thermal Load Studies on the Photocathode Insert with Exchangeable Plug for the bERLinPro SRF-Photoinjector". In: *Proc. SRF'19*. JACoW Publishing, 2019.

[46] Martin Anton Helmut Schmeißer. *Photocathodes for high brightness, high average current photoelectron injectors*. Humboldt Universitaet zu Berlin (Germany), 2019.

[47] J Dube, J Kühn, C Wang, S Mistry, G Klemz, A Galdi, and T Kamps. "Triple evaporation growth and photoemission characterization of bialkali antimonide photocathodes". In: *Journal of Applied Physics* 138.4 (2025).

[48] X. Liang et al. "Deposition and In-Situ Characterization of Alkali Antimonide Photocathodes". In: *Proc. IPAC'12*. JACoW Publishing, 2012, 670–672.

[49] Anubhav Jain, Shyue Ping Ong, Geoffroy Hautier, Wei Chen, William Davidson Richards, Stephen Dacek, Shreyas Cholia, Dan Gunter, David Skinner, Gerbrand Ceder, and Kristin A. Persson. "Commentary: The Materials Project: A materials genome approach to accelerating materials innovation". In: *APL.Mater.* 1.1 (2013), 011002.

[50] Hans Kirschner. "Spectral quantum efficency measurements on Cs-K-Sb photocathodes for the energy-recovery linac test facility bERLinPro". MA thesis. Humboldt-Universität zu Berlin, Mathematisch-Naturwissenschaftliche Fakultät, 2017.

[51] Noel H Turner and John A Schreifels. "Surface analysis: X-ray photoelectron spectroscopy and auger electron spectroscopy". In: *Analytical chemistry* 72.12 (2000), 31–56, 57–61, 421–425.

[52] Stephan Hüfner. *Photoelectron spectroscopy: principles and applications*. Springer Science & Business Media, 2013.

[53] JL Campbell and Tibor Papp. "Widths of the atomic K–N7 levels". In: *Atomic Data and Nuclear Data Tables* 77.1 (2001), 1–56.

[54] John F. Watts and James E. Castle. "The development of laboratory-based high energy sources for XPS". In: *Surface and Interface Analysis* 56.7 (2024), 408–424.

[55] J H Scofield. *Theoretical photoionization cross sections from 1 to 1500 keV.* Tech. rep. California Univ., Livermore. Lawrence Livermore Lab., 1972.

[56] Wolfgang SM Werner, Werner Smekal, and Cedric J Powell. *NIST Database for the Simulation of Electron Spectra for Surface Analysis (SESSA)*. 2011.

[57] Shigeo Tanuma, Cedric J Powell, and David R Penn. "Calculations of electron inelastic mean free paths. V. Data for 14 organic compounds over the 50–2000 eV range". In: *Surface and interface analysis* 21.3 (1994), 165–176.

[58] Jill Chastain and Roger C King Jr. "Handbook of X-ray photoelectron spectroscopy". In: *Perkin-Elmer Corporation* 40.221 (1992), 25.

[59] Irene Martini, Eric Chevallay, Valentin Fedosseev, Christoph Hessler, Holger Neupert, Valentin Nistor, and Mauro Taborelli. "X-ray photoemission spectroscopy studies of cesium antimonide photocathodes for photoinjector applications". In: *Physics Procedia* 77 (2015), 34–41.

[60] S Schubert, M Ruiz-Osés, I Ben-Zvi, T Kamps, X Liang, E Muller, K Müller, H Padmore, T Rao, X Tong, et al. "Bi-alkali antimonide photocathodes for high brightness accelerators". In: *Apl Materials* 1.3 (2013).

[61] F Wooten and WE Spicer. "Surface effects, band bending, and photoemission in semiconducting films of Cs3Sb". In: *Surface Science* 1.4 (1964), 367–377.

[62] E Yablonovitch, BJ Skromme, R Bhat, JP Harbison, and TJ Gmitter. "Band bending, Fermi level pinning, and surface fixed charge on chemically prepared GaAs surfaces". In: *Applied physics letters* 54.6 (1989), 555–557.

[63] Pranav Gupta, Luca Cultrera, and Ivan Bazarov. "Monte Carlo simulations of electron photoemission from cesium antimonide". In: *Journal of Applied Physics* 121.21 (2017).

[64] Huamu Xie. "Overview of the semiconductor photocathode research in China". In: *Micromachines* 12.11 (2021), 1376.

[65] Xu-Dong Li, Zeng-Gong Jiang, Qiang Gu, Ming-Hua Zhao, and Li Guo. "Preliminary systematic study of the temperature effect on the K–Cs–Sb photocathode performance based on the K and Cs Co-evaporation". In: *Chinese Physics Letters* 37.1 (2020), 012901.

[66] L Galan and CW Bates Jr. "Structure of multialkali antimonide photocathodes studied by x-ray photoelectron spectroscopy". In: *Journal of Physics D: Applied Physics* 14.2 (1981), 293.

[67] B Vincent Crist. "BE lookup table for signals from elements and common chemical species". In: *Handbook of Monochromatic XPS Spectra: The Elements of Native Oxides* 1 (1999), 77–358.

[68] Martin Knudsen. "The law of molecular flow and viscosity of gases moving through tubes". In: *Ann. Phys.* 28 (1909), 75.

[69] Hai-Tian Zhang, Lei Zhang, Debangshu Mukherjee, Yuan-Xia Zheng, Ryan C Haislmaier, Nasim Alem, and Roman Engel-Herbert. "Wafer-scale growth of VO2 thin films using a combinatorial approach". In: *Nature communications* 6.1 (2015), 8475.

[70] M Pl Seah and WA Dench. "Quantitative electron spectroscopy of surfaces: A standard data base for electron inelastic mean free paths in solids". In: *Surface and interface analysis* 1.1 (1979), 2–11.

[71] Liu Yuanzhen. "Analysis and Study on the Photoelectron Emission Characteristics of Antimony Alkali Effective Photocathode". In: *The 3rd National Science and Technology Exchange Conference of Quantum Electronics Society of Chinese Institute of Electronics on Optoelectronic Devices*. 2023.

[72] D Briggs, RA Marbrow, and RM Lambert. "An XPS and UPS study of the interaction of oxygen with sodium-dosed Ag (110)". In: *Surface Science* 65.1 (1977), 314–324.

[73] Fang Cheng-Wei, Zhang Yi-Jun, Rong Min-Min, Qian Yunsheng, Daia Qingxin, Shi Feng, Cheng Hongchang, and Bai Xiaofeng. "Micro-area Analysis of Surface Contaminations of GaAs Photocathode in Preparation Process". In: *Acta Photonica Sinica* (2019).

[74] Evan O Kane. "Theory of photoelectric emission from semiconductors". In: *Physical review* 127.1 (1962), 131.

[75] DG Fisher, AF McDonie, and AH Sommer. "Band-bending effects in Na2KSb and K2CsSb photocathodes". In: *Journal of Applied Physics* 45.1 (1974), 487–488.

[76] V Sa-Yakanit and HR Glyde. "Urbach tails and disorder". In: *Comments Matter Phys* 13.1 (1987), 35–48.

[77] Julius Kühn, J Borninkhof, M Bürger, André Frahm, Andreas Jankowiak, Thorsten Kamps, Martin Schmeißer, M Schuster, P Murcek, J Teichert, and Rong Xiang. "UHV Photocathode Plug Transfer Chain for the bERLinPro SRF-Photoinjector". In: *Proc. IPAC'17*. JACoW Publishing, 2017.

[78] Dave A Shirley. "High-resolution X-ray photoemission spectrum of the valence bands of gold". In: *Physical Review B* 5.12 (1972), 4709.

[79] R Nyholm and N Mårtensson. "Experimental core-hole ground state energies for the elements 41Nb to 52Te". In: *Solid State Communications* 40.3 (1981), 311–314.

[80] Lothar Ley. "Photoemission in solids II". In: *Topics in Applied Physics* 27 (1979).

[81] Wayne E Morgan, Wojciech J Stec, and John R Van Wazer. "Inner-orbital binding-energy shifts of antimony and bismuth compounds". In: *Inorganic Chemistry* 12.4 (1973), 953–955.

[82] David J Morgan. "Metallic antimony (Sb) by XPS". In: *Surface Science Spectra* 24.2 (2017).

[83] Valentina P Zakaznova-Herzog, SL Harmer, HW Nesbitt, GM Bancroft, R Flemming, and AR Pratt. "High resolution XPS study of the large-band-gap semiconductor stibnite (Sb2S3): structural contributions and surface reconstruction". In: *Surface Science* 600.2 (2006), 348–356.

[84] CT Parzyck, A Galdi, JK Nangoi, WJI DeBenedetti, J Balajka, BD Faeth, H Paik, C Hu, TA Arias, MA Hines, et al. "Single-crystal alkali antimonide photocathodes: High efficiency in the ultrathin limit". In: *Physical review letters* 128.11 (2022), 114801.

[85] L Soriano, L Galan, and F Rueda. "An XPS study of Cs2Te photocathode materials". In: *Surface and Interface Analysis* 16.1-12 (1990), 193–198.

[86] LG Petersson and SE Karlsson. "Clean and oxygen exposed potassium studied by photoelectron spectroscopy". In: *Physica Scripta* 16.5-6 (1977), 425.

[87] David Krix and Hermann Nienhaus. "Low-temperature oxidation of alkali overlayers: Ionic species and reaction kinetics". In: *Applied surface science* 270 (2013), 231–237.

[88] JR Rumble Jr, DM Bickham, and CJ Powell. "The NIST x-ray photoelectron spectroscopy database". In: *Surface and interface analysis* 19.1-12 (1992), 241–246.

[89] A Barrie and FJ Street. "An Auger and X-ray photoelectron spectroscopic study of sodium metal and sodium oxide". In: *Journal of Electron Spectroscopy and Related Phenomena* 7.1 (1975), 1–31.

[90] PH Citrin. "High-resolution X-ray photoemission from sodium metal and its hydroxide". In: *Physical Review B* 8.12 (1973), 5545.

[91] Leonardo Soriano Leonardo Soriano and Luis Galán Luis Galán. "Interaction of cesium-potassium antimonide photocathode materials with oxygen: An x-ray photoelectron spectroscopy study". In: *Japanese journal of applied physics* 32.10R (1993), 4737.

[92] A Galdi, CT Parzyck, WJI DeBenedetti, J Balajka, L Cultrera, IV Bazarov, H Paik, L Moreschini, C Hu, KM Shen, et al. “Understanding the growth dynamics Cs-Sb thin films via in-situ characterization techniques: Towards epitaxial alkali antimonide photocathodes”. In: *Quantum* 10 (2021), 4.

[93] Pallavi Saha, Oksana Chubenko, Gevork S Gevorkyan, Alimohammed Kachwala, Christopher J Knill, Carlos Sarabia-Cardenas, Eric Montgomery, Shashi Poddar, Joshua T Paul, Richard G Hennig, et al. “Physically and chemically smooth cesium-antimonide photocathodes on single crystal strontium titanate substrates”. In: *Applied Physics Letters* 120.19 (2022).

[94] Erdong Wang. “High average current HVDC electron gun RD for EIC hadron cooling”. In: *Proc. ERL’24*. JACoW Publishing, 2024.